

Charles University in Prague
Faculty of Mathematics and Physics

DOCTORAL THESIS



Vlastimil Kuš

Study of diffractive processes at the ATLAS Experiment

Institute of Particle and Nuclear Physics

Supervisor of the doctoral thesis: Mgr. Marek Taševský, Ph.D.

Study programme: Physics

Specialization: Subnuclear Physics

Prague 2015

Dedicated to all those who strive and endure.

"Hope is definitely not the same thing as optimism. It is not the conviction that something will turn out well, but the certainty that something makes sense, regardless of how it turns out."

Václav Havel

"If you set out to be liked, you would be prepared to compromise on anything at any time, and you would achieve nothing."

Margaret Thatcher

Acknowledgements

I would like to express my gratitude to all people close to my heart, especially my parents and family, for their long lasting support and trust even in times when it was not easy to see which way to go.

I am grateful to Marek Taševský for his support and guidance during last several years, which were very important for the success of my PhD research.

My thanks belong also to Oldřich Kepka for many useful discussions. His deep understanding of the ATLAS Experiment and particle physics helped me to push the diffractive analysis forward. Last but not least, I would like to thank to many of my colleagues and friends at CERN and in Prague for a great ride during these last years, both in professional and personal sense.

I declare that I carried out this doctoral thesis independently, and only with the cited sources, literature and other professional sources.

I understand that my work relates to the rights and obligations under the Act No. 121/2000 Coll., the Copyright Act, as amended, in particular the fact that the Charles University in Prague has the right to conclude a license agreement on the use of this work as a school work pursuant to Section 60 paragraph 1 of the Copyright Act.

In Prague, 20.3.2015

signature of the author

Název práce: Studium difrakčních procesů v experimentu ATLAS
Autor: Vlastimil Kuš
Katedra: Ústav částicové a jaderné fyziky
Vedoucí práce: Mgr. Marek Taševský, Ph.D.
Fyzikální ústav Akademie věd ČR, v.v.i.

Abstrakt: Data z pp srážek odpovídající integrální luminositě 6.75 nb^{-1} byla zaznamenána detektorem ATLAS na urychlovači LHC při těžiškové energii $\sqrt{s} = 7 \text{ TeV}$. Události obsahující alespoň dva jety s $p_T > 20 \text{ GeV}$ jsou použity k provedení měření diferenciálního účinného průřezu difrakční dijetové produkce jakožto funkce velikosti tzv. gapu v rapiditě $\Delta\eta^F$, tj. největší dopředné oblasti začínající na $|\eta| = 4.8$ bez částic s hybností nad definovanou hranicí, a veličině $\tilde{\xi}^\pm$, kterážto aproximuje relativní úbytek hybnosti rozptýleného protonu za předpokladu jednoduché difrakční disociace ($pp \rightarrow pX$). Porovnání s různými Monte Carlo modely ukazuje, že ač je v oblasti malých $\tilde{\xi}^\pm$ a velkých gapů v rapiditě dominantní difrakční produkce, příspěvek od nedifrakčních událostí nelze zanedbat. Pravděpodobnost přežití gapů v rapiditě je určena na základě srovnání s Monte Carlo předpověďmi v oblasti $-3.2 < \log_{10} \tilde{\xi}^\pm < -2.5$ rozdělení $\tilde{\xi}^\pm$ s užitím dodatečného výběrového kritéria $\Delta\eta^F > 2$.

Klíčová slova: difrakce, difrakční dijety, pravděpodobnost přežití gapu v rapiditě

Title: Study of diffractive processes at the ATLAS Experiment
Author: Vlastimil Kuš
Department: Institute of Particle and Nuclear Physics
Supervisor: Mgr. Marek Taševský, Ph.D.
Institute of Physics of the Academy of Sciences of the CR, v.v.i.

Abstract: A data sample of pp collisions corresponding to an integrated luminosity of 6.75 nb^{-1} was collected at $\sqrt{s} = 7 \text{ TeV}$ using the ATLAS detector at the Large Hadron Collider. Collision events with at least two jets with $p_T > 20 \text{ GeV}$ are used to measure the differential cross section of the diffractive dijet production as a function of the rapidity gap size $\Delta\eta^F$, the largest forward region extending from $|\eta| = 4.8$ devoid of particle activity above threshold momentum cuts, and an estimator of the fractional momentum loss of the scattered proton assuming the single diffractive dissociation ($pp \rightarrow pX$), $\tilde{\xi}^\pm$. Comparisons with various Monte Carlo models reveal that though the region of small $\tilde{\xi}^\pm$ and large rapidity gaps is dominated by diffraction, a contribution from non-diffractive events cannot be neglected. The rapidity gap survival probability is estimated based on data to Monte Carlo comparisons in the $-3.2 < \log_{10} \tilde{\xi}^\pm < -2.5$ region of the $\tilde{\xi}^\pm$ distribution with the $\Delta\eta^F > 2$ requirement.

Keywords: diffraction, diffractive dijets, rapidity gap survival probability

Contents

Introduction	3
1 Strong interactions and diffraction	5
1.1 The Standard Model of particle physics	5
1.2 Strong interactions	5
1.3 The diffraction	7
1.3.1 Regge theory and the concept of the pomeron	8
1.3.2 Diffractive dissociation	9
1.3.3 Hard diffraction	11
1.3.4 Diffractive variables	12
1.3.5 Factorization breaking	13
1.3.6 Gap survival probability	14
1.4 Diffractive dijets measured by the CMS Collaboration	15
2 The LHC accelerator and the ATLAS detector	17
2.1 The Large Hadron Collider	17
2.2 Multiple proton-proton interactions (pile-up)	18
2.3 The ATLAS Experiment	19
2.3.1 The Inner Detector	19
2.3.2 Calorimeter system	21
2.3.3 Muon chambers	23
2.3.4 MBTS	25
2.4 ATLAS forward detectors	25
2.4.1 LUCID	26
2.4.2 ZDC	26
2.4.3 ALFA	26
2.5 Data acquisition and trigger system	27
3 Software and computing	29
3.1 Distributed grid computing	29
3.2 ATLAS framework	29
3.3 D3PD production	30
3.4 ROOT	31
4 Monte Carlo simulations	33
4.1 General Monte Carlo concepts	33
4.2 PYTHIA8	33
4.2.1 Non-diffractive modelling	34
4.2.2 Diffractive modelling	34
4.3 Herwig++	34
4.4 POMWIG	35
4.5 POWHEG	35
4.6 Monte Carlo event generation of diffractive dijet events	36
4.6.1 ATLAS Monte Carlo request	36
4.6.2 Private MC production	38

5	Testing the Jet Energy Scale using dijet events	39
5.1	Introduction to the in-situ pseudorapidity intercalibration method	39
5.1.1	Standard method	39
5.1.2	Matrix method	40
5.2	Event selection	41
5.3	Monte Carlo simulations	41
5.4	Results	42
5.4.1	Dijets in 2010 data	42
5.4.2	Dijets in 2011 data	42
5.4.3	Conclusions	44
6	The event selection	49
6.1	Data samples	49
6.2	Trigger selection	50
6.2.1	Jet and minimum bias triggers	50
6.2.2	Trigger prescales	51
6.2.3	Luminosity and cross section	52
6.2.4	Inclusive 2010 dijet analysis	53
6.2.5	Trigger scheme optimization	54
6.2.6	Trigger efficiency measurement	55
6.2.7	New trigger selection in period F	57
6.2.8	New trigger selection in period B	60
6.2.9	Validation of the new trigger scheme	62
6.2.10	Trigger closure test	62
6.3	Event selection cuts	64
6.3.1	Vertex requirements	64
6.3.2	Jet kinematic selection	66
6.3.3	Jet cleaning	67
7	Rapidity gap measurement	69
7.1	The Forward Rapidity Gap	69
7.2	Noise removal	69
7.2.1	Track cleaning	70
7.2.2	Cluster noise	70
7.3	TopoClusters	71
7.3.1	Cluster energy correction in MC	71
7.3.2	Basic kinematic properties	73
7.4	Rapidity gap definition in the soft gap analysis (“ p_T -method”) . .	74
7.4.1	Herwig++ issues	75
7.5	Optimization of the Forward Rapidity Gap definition (“hybrid method”)	76
7.6	Rapidity gap acceptance	80
7.7	Irregularities in the rapidity gap spectrum	82
7.8	Influence of the Inner Detector	82
7.9	The detector level data to MC comparisons	82

8	Measurement of ξ	85
8.1	Approximation of ξ	86
8.2	ξ acceptance	91
8.3	The detector level Data vs. Monte Carlo comparisons	93
9	Unfolding	95
9.1	1D unfolding	95
9.2	2D unfolding	96
9.2.1	Choice of bins	99
9.2.2	Monte Carlo scaling for the use in the unfolding	100
9.2.3	Unfolding tests	101
9.2.4	Choice of the number of iterations	105
9.2.5	Statistical uncertainties	105
9.3	Comparison of 1D and 2D unfolding techniques	106
10	Evaluation of systematic uncertainties	109
10.1	Jet-related systematic uncertainties	109
10.1.1	Uncertainty of the L1_J5 Trigger Efficiency Fits	109
10.1.2	Trigger uncertainty	110
10.1.3	Jet Energy Scale uncertainty (JES)	110
10.1.4	Jet Energy Resolution (JER)	112
10.1.5	Jet Angular Resolution (JAR)	112
10.1.6	Jet Reconstruction Efficiency (JRE)	113
10.1.7	Jet Cleaning Efficiency (JCE)	113
10.2	Diffraction systematic uncertainties	113
10.2.1	Left-right asymmetry of the rapidity gap start	114
10.2.2	Cluster energy scale uncertainty (CES)	114
10.2.3	Cell Significance Threshold Uncertainty (CST)	114
10.2.4	Tracking uncertainty	115
10.3	Other sources	115
10.3.1	Luminosity uncertainty	115
10.3.2	Primary vertex requirement	116
10.3.3	Additional material	116
10.3.4	Unfolding uncertainty	116
10.4	Summary: combined systematic uncertainties	117
11	Background influence	121
11.1	In-time pile-up	121
11.2	Out-of-time pile-up	121
11.3	Beam induced background	122
12	Results	123
12.1	Measurement of $\Delta\eta^F$ and $\tilde{\xi}^\pm$	123
12.1.1	Process decomposition	123
12.1.2	Comparisons to non-diffractive models	125
12.1.3	Double Pomeron Exchange irreducible background	126
12.1.4	Comparisons to various diffractive models	126
12.2	Estimate of the gap survival probability	129

13 Conclusions	133
A Reproduction of the 2010 inclusive dijet measurement	135
B Systematic uncertainties: summary tables	137

Introduction

In last decades, diffraction has always had an important place among physics goals of high energy collision experiments involving hadrons. A significant progress came with measurements by the H1 Collaboration at HERA electron-proton accelerator at DESY laboratory: new results and achieved precision of diffractive measurements were unprecedented. The success of H1 Collaboration was followed by experiments with proton-antiproton collisions at the Tevatron accelerator at the Fermi National Accelerator Laboratory, which pushed the boundaries of the diffractive understanding even further. Finally, currently the largest ever built accelerator, called LHC, has been built at CERN and it incited the curiosity of the diffractive community once again, as a significant part of proton-proton interactions is made up by diffractive processes.

These most important milestones, along with other relevant topics, are briefly discussed in the introductory Chapter 1. Chapter 2 provides a curious reader with a technical overview of the LHC accelerator and the ATLAS detector, followed by a description of a software equipment (Chapter 3) and Monte Carlo generators (Chapter 4) used for the study presented in this thesis. Chapter 5 gives a brief but complete description of a jet-related performance work done within the ATLAS Calorimeter Section and Chapter 6 summarizes in detail all important studies crucial for the feasibility of the diffractive dijet analysis - a design and validation of new trigger selection scheme, pile-up studies and jet selection criteria. Chapters 7 and 8 define and validate the measurable quantities, the rapidity gap size $\Delta\eta^F$ and the fractional momentum loss of the diffractive proton, ξ^\pm . This turned out to be a challenge since all detector effects and limitations have to be well understood and matched to the generator level, to which the measurement of $\Delta\eta^F$ and ξ^\pm is corrected (details can be found in Chapter 9). Each experimental research is influenced by a number of systematic uncertainties, quantified in Chapter 10, and contributions from background processes (Chapter 11). Finally, fully corrected results (compared to various Monte Carlo models) and conclusions are discussed in detail in Chapter 12 and summarized in Chapter 13.

The physics analysis presented in this document is based on the work performed during my PhD studies. It was regularly presented and thoroughly discussed within the ATLAS Standard Model Soft QCD and Diffractive Physics group meetings and is currently in an advanced state of the approval process within the ATLAS Collaboration, which will lead to the ATLAS publication.

1. Strong interactions and diffraction

1.1 The Standard Model of particle physics

The Standard Model (SM) of particle physics (summarized e.g. in [1]), based on a quantum field theory, describes the universe of elementary particles and basic interactions acting among them. It is based on $SU(3)_C \otimes SU(2)_L \otimes U(1)_Y$ symmetry group, where C stands for the color charge, L for the left handed coupling of the weak isospin doublets and Y for the weak hypercharge. According to the Standard Model describing the electromagnetic, weak and strong interactions, the elementary particles interact via the exchange of gauge bosons (arising from the requirement of the local gauge invariance of corresponding Lagrangians) having an integer spin. The field particle for electromagnetic interaction is γ (photon), for weak interaction W^\pm and Z^0 and for strong interaction the field particles are gluons (eight of them corresponding to eight generators of the $SU(3)_C$ color group).

The matter fields are grouped in three generations, each of which consists of two leptons and two quarks. Leptons are either electron e , muon μ or tauon τ and their corresponding neutrinos ν_e , ν_μ and ν_τ , while quarks of flavors up (u), down (d), charm (c), strange (s), top (t) and bottom (b) are grouped as (ud), (cs) and (tb). Each of the fermions (particles with half-integer spin) has moreover an antimatter counterpart of the same mass but opposite additive quantum numbers and each of the quarks has one of the three independent color quantum numbers. While leptons e , μ and τ have an electric charge $-q_e$ ¹, the quarks have a fractional charge of $2/3 \cdot q_e$ (up-type) or $-1/3 \cdot q_e$ (down-type).

Finally, the spontaneous symmetry breaking is the mechanism which gives masses to the fermions and bosons. An essential feature of such a mechanism is an appearance of a new heavy scalar particle - the Higgs boson. After the discovery of the top quark at the Tevatron accelerator at the Fermi National Accelerator Laboratory, the Higgs boson was the last missing piece of the SM waiting to be discovered. That was the main challenge for the Large Hadron Collider (LHC) and its experiments such as the ATLAS. Eventually, three years of the LHC running and systematic data analysis resulted in the Higgs boson discovery in 2012 and led to the Nobel price in Physics award for Peter Higgs and Francois Englert.

1.2 Strong interactions

The so-called Mandelstam variables are often introduced to describe the generalised scattering process of the form $ab \rightarrow cd$, see Figure 1.1. The most commonly used ones are s and t , the square of the centre-of-mass energy of the interaction

¹The elementary electric charge $q_e \doteq 1.602 \cdot 10^{-19}$ C.

and the square of the four-momentum transfer:

$$s = (A + B)^2 = (C + D)^2 \approx 2A \cdot B \approx 2C \cdot D \quad (1.1)$$

$$t = q^2 = -Q^2 = (A - C)^2 = (B - D)^2 \approx -2A \cdot C \approx -2B \cdot D \quad (1.2)$$

The A , B , C and D are four-vectors of the incoming or outgoing particles. The commonly used approximations indicated in these equations are valid in the high energy limit, i.e. when the particle masses can be neglected.

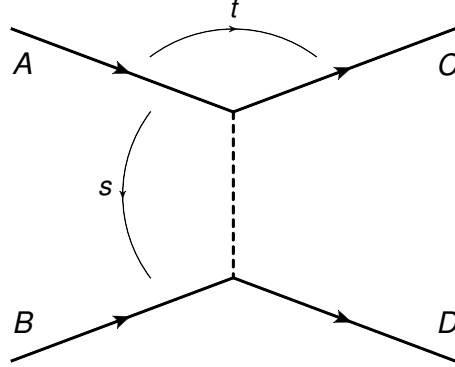


Figure 1.1: Generalised scattering process.

The Quantum Chromodynamics (QCD) [2] is a theory of strong interactions based on $SU(3)_C$ color group. The QCD Lagrangian containing colored quark fields is required to have the local gauge symmetry, which in turn leads to the massless vector bosons - gluons - as the mediators of the strong nuclear force. The QCD Lagrangian can be written as

$$\mathcal{L}_{QCD} = -\frac{1}{4}F_{\mu\nu}^a F^{a\ \mu\nu} + \sum_{\text{flavors } k}^{n_f} \bar{\Psi}_k(i\not{D} - m)\Psi_k + \mathcal{L}_{\text{gaugefix}} + \mathcal{L}_{\text{ghost}} \quad (1.3)$$

where

$$D_\mu = \partial_\mu - igA_\mu^a \frac{\lambda^a}{2} \quad (1.4)$$

$$F_{\mu\nu}^a = \partial_\mu A_\nu^a - \partial_\nu A_\mu^a + gf^{abc}A_\mu^b A_\nu^c. \quad (1.5)$$

The Ψ_k are quark fields of flavor k , $a = 1 \dots 8$ represent eight spin-1 massless gluon fields A_μ^a mediating the strong interaction, the kinetic term $-\frac{1}{4}F_{\mu\nu}^a F^{a\ \mu\nu}$ introduces the gluon self-interactions and the f_{abc} factors are related to the generators of the $SU(3)_C$ color group Gell-Mann matrices λ_{ij}^a ($[\lambda^a, \lambda^b] = i\lambda^c$). $\mathcal{L}_{\text{gaugefix}}$ is the gauge fixing term and the $\mathcal{L}_{\text{ghost}}$ is there to cancel the unphysical degrees of freedom of the gluon field which would otherwise appear in the measurable quantities.

The generators of the QCD symmetry group, the Gell-Mann matrices, result

in $3^2 - 1 = 8$ colored gluons². The QCD potential between two quarks can be approximated as

$$V(r) = kr - \frac{\alpha_S}{r}, \quad (1.6)$$

where k is a constant, r is a radial distance of the two quarks and α_S is the coupling of strong interactions. In this simple model, the potential energy increases linearly with r until it is energetically more favorable to produce the quark-antiquark pair.

The calculation of scattering amplitudes at the leading order (LO) is usually straightforward. When going to higher orders of the perturbation theory, however, one must account for the Feynman diagrams with fermion or boson loops. Calculations of such loops lead to the infinities due to the integrals over arbitrarily large momenta (so-called “UV divergences”). The resulting infinite cross-sections would thus be incapable to describe physical processes. To deal with this issue, the so-called “renormalization” procedure has been introduced to remove the UV divergences from the measurable quantities. The basic concept of the renormalization is in redefinitions of basic “bare” quantities such as the fermion masses, electrical charge, strong coupling constant α_S etc. The renormalization procedure introduces new quantities which are, unlike their “bare” predecessors, physically relevant.

In case of the strong coupling constant, its renormalized counterpart depends on the four-momentum transfer Q^2 (as defined above), which is a characteristic scale of the interaction. In the leading order, the α_S can be schematically expressed as

$$\alpha_S(Q^2) \approx \frac{1}{\beta_0 \ln(Q^2/\Lambda_{\text{QCD}}^2)}, \quad (1.7)$$

where β_0 is a negative constant (reflects the number of quark flavors) and $\Lambda_{\text{QCD}} \sim 200$ MeV is a scale where the coupling diverges. This perturbative result is not valid at small scales (below $Q \sim 1$ GeV) corresponding to the typical mass of light hadrons. Given the Equation 1.7, the α_S is rather than “constant” called the “running constant”, as it depends on the Q^2 . At low Q^2 (large distances) the coupling is large, which results in quarks and gluons being confined within hadrons. In the other limit where Q^2 is large (small distances), the asymptotic freedom exists and the perturbative approach of QCD calculations can be used. The decrease of α_S with increasing Q^2 was measured in several experiments and is plotted in Figure 1.2.

1.3 The diffraction

The total cross section in hadronic scattering experiments can be classified into three categories: the elastic, diffractive and non-diffractive (ND) component. At

²The ninth combination is a color singlet and thus must be excluded.

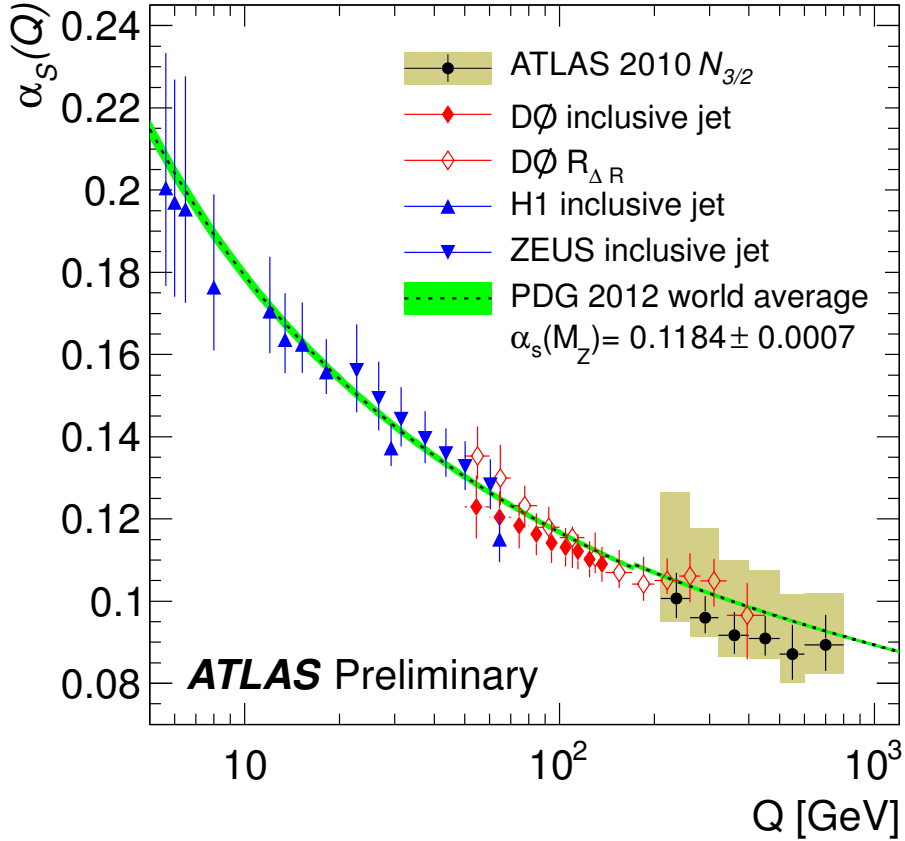


Figure 1.2: The running coupling constant α_s as a function of Q^2 as measured in various experiments and with the latest ATLAS results. Taken from [3].

LHC energies, the elastic part accounts for about 20 % of the total cross section while the inelastic contribution (diffractive and non-diffractive) is the remaining 80 % (out of which $\sim 25 - 30\%$ of the $\sigma_{\text{inelastic}}$ is attributed to the diffractive channels).

The diffraction can be defined as an interaction which is governed by the exchange of quantum numbers of the vacuum. This process can be described in the QCD at the lowest order by the exchange of two gluons in the overall color singlet state. This simple approach is not, however, able to describe the measured data. Moreover, as the diffraction processes are generally soft, i.e. governed via exchanges with typically small momentum transfers, their description in the realm of the QCD thus becomes complicated: the calculations at small momenta transfers (large running coupling constant) cannot be carried out via perturbative expansion. The diffraction is thus often described by models such as the Regge theory [4].

1.3.1 Regge theory and the concept of the pomeron

The Regge theory [4] was introduced to study properties of the particle scattering. It was based primarily on the analytical properties and unitarity of scattering

amplitudes. The quantum mechanics classifies the bound states of a spherically symmetric potential according to their angular momentum and the energy. These bound states appear as poles of the partial wave amplitude with a given integer angular momentum of the integer type (l). The idea introduced by the Regge theory was to consider the l in these amplitudes as complex rather than integer. This led to the concept of the *Regge trajectory* as the poles lie on a straight line in cases of “well behaved” potentials (such as Yukawa). The Regge trajectory is parametrized by the linear equation

$$\alpha(t) = \alpha(0) + \alpha'(t) \quad (1.8)$$

where $\alpha(0)$ is the so-called intercept and the α' is the t -dependent trajectory slope.

The hadronic interaction is modeled, within the Regge theory, in terms of exchanges of reggeons and pomerons, which are, rather than real single particles, a simplistic parametrizations of complicated soft gluon exchanges lying beneath. They are, in fact, defined by all particles located on the Regge trajectory. All known resonances lie on reggeon trajectories with $\alpha(0) < 1$, which leads to a major consequence: the total cross section should decrease with the increasing centre-of-mass collision energy.

The pomeron trajectory was introduced in order to explain the increase of the total cross section with the increasing center-of-mass energy, as the reggeon exchange only predicts a slow decrease. The experimental fit done by Donnachie and Landshof showed [5] that the scattering data is well described with a combination of two different Regge trajectories, the reggeon (\mathbb{R}) and the pomeron (\mathbb{P}). The pomeron intercept is found to be greater than one and can thus account for the increase of the total cross section. Note that the pomeron trajectory is there to only parametrize the partonic activity in the hadron scattering, it is not associated with any real particle exchange.

1.3.2 Diffractive dissociation

The diffractive contribution to the inelastic cross section can be classified into three types of processes:

- Single Diffractive dissociation (SD)
- Double Diffractive dissociation (DD)
- Central Diffraction (CD)

In terms of the final state properties, all these interactions are characterised by a presence of so-called rapidity gaps as regions in pseudorapidity η devoid of hadronic activity. Rapidity gaps can occur in non-diffractive events as well due to fluctuations in hadronisation, though the rapidity gap size is exponentially suppressed. This is in contrast with the SD, DD and CD processes where the large rapidity gap size is one of the key characteristics.

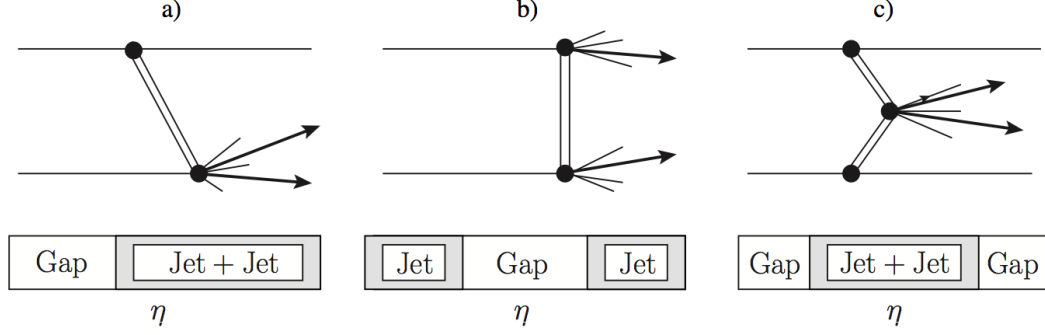


Figure 1.3: Schematic view of three diffractive interactions at hadron-hadron colliders: a) Single Diffractive dissociation, b) Double Diffractive dissociation, c) Central Diffraction.

Single Diffractive dissociation Single Diffraction, depicted in Figure 1.3a, is the process of the form $a + b \rightarrow a + X$. One of the interacting hadrons (a , b) remains intact while the other one dissociates into a multi-particle final state X with the same quantum numbers as the original particle. A rapidity gap occurs between the system X and the scattered hadron a . In Regge theory, the cross section is calculated in a so-called triple-Regge limit with a triple-pomeron vertex [6]. It can be written as

$$\frac{d^2\sigma^{SD}}{dM_X^2 dt} = f_{\mathbb{P}}(M_X^2, t) \sigma_{\mathbb{P}}(M_X^2) \quad (1.9)$$

where M_X is the invariant mass of the dissociated system, $\sigma_{\mathbb{P}}(M_X^2)$ is the cross section of interaction between the pomeron and the particle b and $f_{\mathbb{P}}(M_X^2, t)$, which is often referred to as the *pomeron flux*, is given by

$$f_{\mathbb{P}}(M_X^2, t) = \frac{1}{16\pi^2 s} |g_{\mathbb{P}}(t)|^2 \left(\frac{s}{M_X^2} \right)^{2\alpha_{\mathbb{P}}(t)-1}, \quad (1.10)$$

where $g_{\mathbb{P}}(t)$ is a function including terms corresponding to the triple-pomeron vertex and $\alpha_{\mathbb{P}}(t)$ is defined by Equation 1.8.

Double Diffractive dissociation These are processes of the form $a + b \rightarrow X + Y$, see Figure 1.3b. Both interacting particles dissociate into final systems X and Y with the same quantum numbers as original particles a and b . The rapidity gap is located between multi-particle states X and Y .

Central Diffraction Finally, the interactions of the form $a + b \rightarrow a + X + b$ (see Figure 1.3c) where two rapidity gaps are produced between system X and either scattered particle (a , b), are called Central Diffraction. This is achieved by radiating a pomeron from each interacting particle. CD processes are classified as a Central Exclusive Production where both pomerons bring all of their momenta into the hard subprocess and the Double Pomeron Exchange where only fractions of those momenta are used (consequently, pomeron remnants are observed).

1.3.3 Hard diffraction

Hard diffraction is an interaction where, next to the usual diffractive rapidity gap signature, the hard partonic scattering takes place. Just as in case of the soft diffraction, events can have forward, central or multiple rapidity gaps. However, unlike in soft interactions in which it is not possible to determine the underlying dynamics and understand the pomeron structure, the hard diffractive interaction containing jets in the final state (introduced by Ingelman and Schlein [7]) provides a way of probing the nature of the exchanged object. In this view, the probability that a proton emits the pomeron is also based on the Regge theory as in the soft diffraction, however the pomeron trajectory $\alpha(t)$ is different. While in the soft diffractive case the pomeron is described by the trajectory only, it is considered a compound object with partonic structure in the hard diffractive events.

The hard diffractive interactions can be, given their nature (presence of high mass state), calculated perturbatively. They provide a possibility to measure the diffractive parton distribution function (DPDF) of the proton. In the Ingelman-Schein approach, the cross section factorizes into the DPDF and the cross section of the hard partonic sub-process, $\hat{\sigma}(x, Q^2)$. The cross section can be schematically expressed as

$$\sigma = f^D(x, Q^2, \xi, t) \otimes \hat{\sigma}(x, Q^2) , \quad (1.11)$$

where the DPDF of the proton can be further decomposed into the pomeron flux factor ($f_{\mathbb{P}/p}$) and the probability to find a parton i in the pomeron ($f_{i/\mathbb{P}}$)

$$f^D(x, Q^2, \xi, t) = f_{\mathbb{P}/p}(t, \xi) f_{i/\mathbb{P}}(Q^2, x) . \quad (1.12)$$

ξ is the fractional momentum loss of the scattered proton. The Feynman diagram of the hard single diffractive event with the hard scatter is depicted in Figure 1.4. An additional variable $z_{\mathbb{P}}$ denoting the momentum fraction of the pomeron carried by the parton entering the hard interaction is introduced. It can be expressed in terms of the invariant mass of the diffractive final state as

$$z_{\mathbb{P}} = \frac{Q^2}{Q^2 + M_X^2} \quad (1.13)$$

and relates to the Bjorken x via the equation $x = x_{\mathbb{P}} z_{\mathbb{P}}$. The low invariant mass systems denoted as $X_{\mathbb{P}}$ and X_P are the pomeron and proton remnants.

Diffractive Parton Distribution Functions

The first experimental observation of a high- p_T jet production in diffractive interactions was done by the UA8 Collaboration in $p\bar{p}$ collisions at CERN [8]. Scattered protons were detected in forward spectrometers, while the center of the detector was occupied by jets having similar distributions as those from the inelastic parton-parton interactions. This measurement thus suggested a parton scattering beneath the diffractive processes which in turn allowed for the interpretation of the measurement in terms of diffractive PDFs.

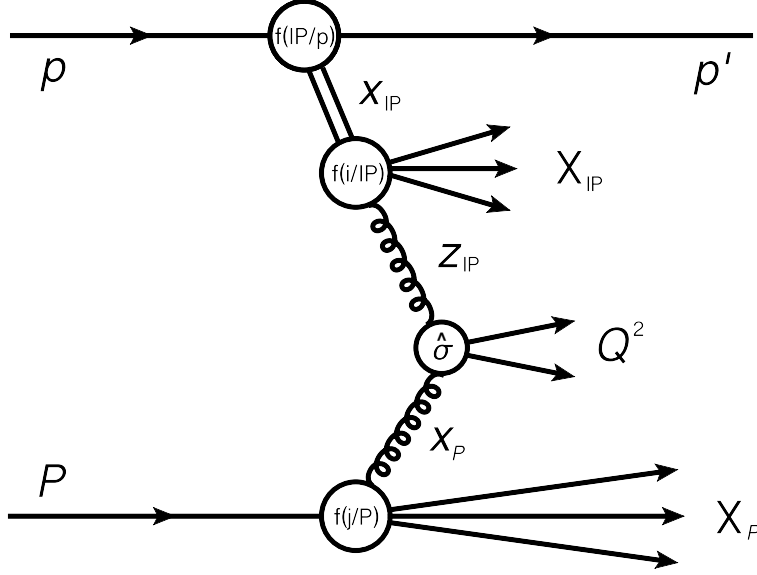


Figure 1.4: Single diffractive proton-proton interaction with hard scatter.

The DPDFs have been precisely measured by the HERA experiments by performing NLO QCD fits [9] of a general form for gluon and quark densities

$$zf_i^{\mathbb{P}}(z, Q^2) = A_i z^{B_i} (1 - z)^{C_i} \quad (1.14)$$

where $f_i^{\mathbb{P}}$ is the DPDF, z is the longitudinal proton's momentum fraction carried by the parton entering the sub-process and A_i , B_i , C_i are the fit parameters. These fits were performed on the diffractive deep inelastic scattering data and are denoted as “H1 2006 DPDF Fit A” and “H1 2006 DPDF Fit B”, where in the “Fit A” the B term for gluons was omitted while in the “Fit B” both the B and C gluon terms were omitted. In both of these DPDFs the majority of the pomeron momentum is carried by gluons at small $z_{\mathbb{P}}$, with a small quark contribution. Results are presented in Figure 1.5 along with the comparison to the Tevatron data.

The DPDF set used in the physics analysis presented in this thesis are the “H1 2006 DPDF Fits B” [9], for which both leading order and NLO PDF sets are available, with little difference between them. The fit used to extract these PDFs simultaneously obtained an effective pomeron trajectory with $\alpha_{\mathbb{P}}(0) = 1.118 \pm 0.008$ (exp.) $^{+0.029}_{-0.010}$ (sys).

1.3.4 Diffractive variables

Among commonly used variables describing the diffractive dissociation are:

- $M_{X(Y)}$ - the invariant mass of the dissociation system X (Y)
- ξ - fractional momentum loss of the scattered proton
- $\Delta\eta$ - a size of the rapidity gap

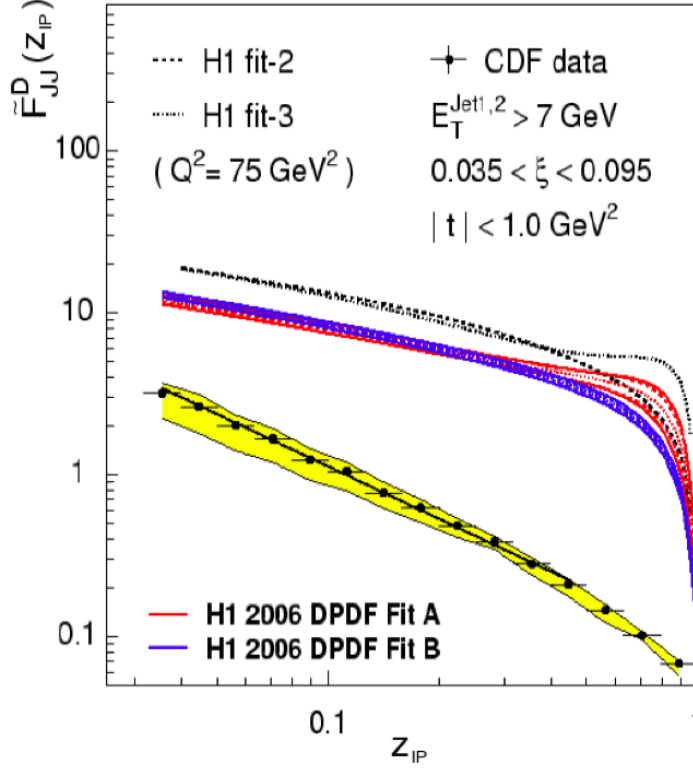


Figure 1.5: Comparison of the Tevatron data (in the yellow band) to the predictions based on the H1 measurement of the DPDFs, as a function of the momentum fraction of the pomeron carried by the parton involved in the hard scatter [10].

What is worth noting is the fact that these variables are not independent. The fractional momentum loss can be expressed in terms of the invariant mass

$$\xi = \frac{p_Z^{\text{In}} - p_Z^{\text{Out}}}{p_Z^{\text{In}}} = \frac{M_X^2}{s}. \quad (1.15)$$

Moreover, the size of the rapidity gap is closely correlated with ξ via

$$\Delta\eta \sim -\log \xi, \quad (1.16)$$

meaning that the smaller the ξ (M_X), the bigger the rapidity gap. It is therefore obvious that the regions of interest for providing an evidence of a hard diffractive contribution into the dijet cross section are large rapidity gaps and small ξ .

1.3.5 Factorization breaking

The QCD factorization, expressed by Equation 1.11, works well for the ep deep inelastic collisions as confirmed by many HERA measurements and it was also proven theoretically [11]. At proton-antiproton collisions at Tevatron, however, the factorization was observed to be broken, as evidenced e.g. by Figure 1.5 where the measured DPDF extracted from diffractive dijet events is compared with predictions based on HERA measurements. At the leading order, the ratio

of the SD to ND events is equal to the ratio of the respective structure functions. The ratio $R(x, \xi)$ integrated over t and jet E_T is

$$R_{\text{SD/DD}}(x, \xi) = \frac{n_{jj}^{\text{SD}}}{n_{jj}^{\text{ND}}} \simeq \frac{F_{jj}^{\text{SD}}(x, \xi)}{F_{jj}^{\text{ND}}(x)}, \quad (1.17)$$

where $n_{jj}^{\text{SD (ND)}}$ is the number of single-diffractive (non-diffractive) dijet events, $F_{jj}^{\text{ND}}(x)$ is the known ND structure function and $F_{jj}^{\text{SD}}(x, \xi)$ is the diffractive structure function, which can thus be extracted as $F_{jj}^{\text{SD}}(x, \xi) = R_{\text{SD/DD}}(x, \xi) F_{jj}^{\text{ND}}(x)$. The CDF experiment measured the diffractive dijets in proton-antiproton collisions, see e.g. [10]. If the QCD factorization held, the production cross-section could be written as a convolution

$$d\sigma^{p\bar{p} \rightarrow p \oplus jj^X} = f_{\mathbb{P}/p}(\xi, t) \cdot f_{i/\mathbb{P}}(z_{\mathbb{P}} = x/\xi, \mu) \cdot f_{j/p}(x_2, \mu) \otimes d\sigma_{\text{sub}}^{jj}(z_{\mathbb{P}}, x_2, \mu), \quad (1.18)$$

where $f_{\mathbb{P}/p}(\xi, t)$ is the pomeron flux, $f_{i/\mathbb{P}}(z_{\mathbb{P}}, \mu)$ is the density function of a parton i carrying fraction $z_{\mathbb{P}}$ of the pomeron momentum, $f_{j/p}(x_2, \mu)$ is the density function of a parton j carrying a momentum fraction x_2 of the proton, μ is the factorization and renormalization scale (set to equal values) and the $d\sigma_{\text{sub}}^{jj}(z_{\mathbb{P}}, x_2, \mu)$ is the sub-process cross-section of the inelastic hadron-hadron scattering. The CDF measurement has proven that the universal QCD factorization in diffraction is broken.

1.3.6 Gap survival probability

It was believed that the diffractive parton distribution functions measured at HERA in the ep collisions are universal, i.e. that they can be used to provide predictions for other diffractive experiments, such as the structure function measurement in $p\bar{p}$ collisions at the Tevatron. This comparison, presented in Figure 1.5, reveals a significant disagreement. The Tevatron measurement is suppressed by an approximately constant factor 10 with respect to the HERA-based predictions, though some $z_{\mathbb{P}}$ -dependence is observed. This is caused by the above mentioned factorization breaking. While the QCD factorization works very well in diffractive ep collisions, it is broken in hadron-hadron collisions due to additional soft partonic interactions and rescattering among spectator partons. The soft interactions lead to the breaking of the outgoing proton and a loss of the rapidity gap, which is filled by this additional particle production. This effect is usually referred to as the *gap survival probability*, denoted as S^2 . The diffractive cross section in hadron-hadron colliders can then be expressed as the cross section of the hard scattering multiplied by the S^2 .

The so-called KMR model [12], implementing the QCD factorization breaking by multi-pomeron exchanges, is successful in reproducing the Tevatron measurement for the single diffraction in dijet events, where the soft survival probability was found to be $S^2 \sim 0.1$. A similar prediction was made for the LHC collisions at 7 TeV of the center-of-mass energy which is expected to be around 0.1, but probably smaller.

1.4 Diffractive dijets measured by the CMS Collaboration

The CMS Collaboration has published a measurement of the diffractive contribution to the dijet production as a function of the fractional momentum loss of the scattered proton. The overall integrated luminosity used for this analysis was 2.7 nb^{-1} and only runs with low instantaneous luminosity (low rate of multiple interactions per bunch crossing) were used.

The events of interest were selected by requiring two high- p_T jets ($p_T^{j1, j2} > 20 \text{ GeV}$) reconstructed by the anti- k_T jet finding algorithm with distance parameter 0.5. Moreover, the diffractive contribution was enhanced by requiring that the most forward particle flow (PF) object (calorimeter cluster or track) has $\eta_{\min} > -3$ or $\eta_{\max} < 3$. Since the measurement is done in the region $|\eta| < 4.9$, these cuts are equivalent to a requirement on a rapidity gap size $\Delta\eta > 1.9$ ranging from the edge of the CMS detector. Charged PF objects in the central region ($|\eta| < 2.4$) entering the ξ calculation were selected by $p_T > 200 \text{ MeV}$ cut while in the forward region ($3 < |\eta| < 4.9$) the energy cut $E > 4 \text{ GeV}$ was employed.

Results are presented in Figure 1.6. The data are compared to various Monte Carlo models, both diffractive (POMPYT SD, POMWIG SD and PYTHIA8 SD+DD at the leading order (LO) and POWHEG at the next-to-leading order (NLO)) and non-diffractive (PYTHIA6 and PYTHIA8 at the LO). The DPDFs used in diffractive models are from the H1 2006 fit B. The non-diffractive MC significantly underestimate data in the lowest ξ bin ($3 \cdot 10^{-4} < \xi < 2 \cdot 10^{-3}$), while the SD models predict about five times more events in the same region. Therefore, this bin can be used to obtain an upper limit on S^2 by dividing the cross section given by the POMWIG or POMPYT and the cross section seen in data (ND contribution neglected): $S^2 = 0.21 \pm 0.07$. This result needs to be corrected for a contribution from the proton dissociation of the scattered proton into a low-mass state, which escapes undetected into the forward region. Correcting for this effect, the gap survival probability is $S^2 = 0.12 \pm 0.05$. Doing the same procedure but with the NLO POWHEG generator, the survival probability is found to be $S^2 = 0.08 \pm 0.04$. Given the large uncertainties of both the measurement and the KMR prediction [12] for the LHC, these results can be considered in rather good agreement with the theoretical prediction.

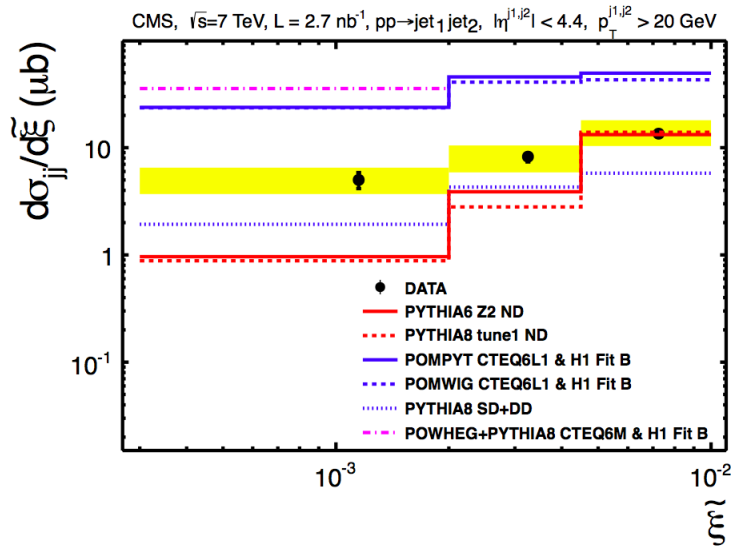


Figure 1.6: Results of the CMS Collaboration on the single diffractive dissociation in dijet events at $\sqrt{s} = 7$ TeV. The differential cross section is measured as a function of the fractional momentum loss ξ . The S^2 is extracted from the lowest- ξ bin by comparing the data and the SD POMPYT and POMWIG. [13]

2. The LHC accelerator and the ATLAS detector

The European Organisation for the Nuclear Research (CERN¹) is an international organisation founded in 1954 on the Swiss-French border near Geneva. Throughout its history it played an important role in the advancement of not only the fundamentals of the particle physics, but of related as well as seemingly unrelated areas such as a significant science-to-business (and vice versa) technology transfer or the creation of the World Wide Web. Being founded on a principle of an open access for every scientist regardless the politics or nationality, it provides a long-term platform not only for a free exchange of ideas, but also for bringing together people of different political, cultural, historical and religious background and playing thus its part in building a better comprehension in the world recovering from the two worst wars in human history.

2.1 The Large Hadron Collider

The Large Hadron Collider (LHC) [14] is an accelerator with 27 km in circumference built at CERN and designed to accelerate and collide protons, Pb ions or proton-ions. It can thus be regarded as an multi-purpose collider providing a basis for a variety of distinctive particle physics measurements. The main physics program is focused on proton-proton collisions at the $\sqrt{s} = 14$ TeV centre-of-mass energy (the designed value; in reality, it was 7 TeV during the first phase of the running) with the instantaneous luminosities of $\mathcal{L} = 10^{34} \text{cm}^{-2}\text{s}^{-1}$. In case of Pb-Pb collisions, the centre-of-mass energy can range up to 5.5 TeV per nucleon pair with the instantaneous luminosity of $10^{27} \text{cm}^{-2}\text{s}^{-1}$.

Along the LHC ring, two general purpose detectors were built for probing proton and Pb ion collisions: the ATLAS (A Toroidal LHC ApparatuS) and CMS (Compact Muon Solenoid). In addition to the ATLAS and CMS, three other experiments were built: the ALICE specialized in heavy ion collision studies, the LHCb probing the B-physics and the TOTEM measuring the total proton-proton cross section (and sharing the interaction point with the ATLAS).

From the technological perspective, the LHC is a ring made of 1232 superconducting dipole magnets producing a magnetic field of the strength of 8.33 T. The operating temperature is 1.9 K which is achieved by the super-fluid liquid helium. The dipole magnets contain two beampipes (for a simultaneous clockwise and counter-clockwise acceleration) surrounded by magnetic coils made of niobium-titanium cables. The acceleration process takes place in radio-frequency cavities installed in sector 4 of the LHC. In addition to the dipole magnets, magnetic elements of higher orders (such as quadrupole focusing magnets) are also installed to maintain the quality of the beam of particles and to, eventually, col-

¹The acronym stems from the French *Conseil Européen pour la Recherche Nucléaire*.

lide them in one of the four interaction point (IP). In total there are over 6600 superconducting magnets installed at the LHC.

The beam of particles accelerated in the LHC can be composed of up to 2808 bunches, each of them having $\sim 10^{11}$ protons. The time distance between bunches can go down to 25 ns which makes about 8 m in length as the protons are accelerated nearly to the speed of light. The typical bunch length is 7.55 cm and their transverse dimension at the ATLAS IP is $16.7 \mu\text{m}$.

An important characteristics of the hadron colliders is the luminosity, which relates the number of interactions and the cross section of the given physics process via formula $N_{int} = \sigma \cdot L$. As the LHC beams have a Gaussian profile, the instantaneous luminosity can be expressed as

$$\mathcal{L} = \frac{n_b f_r n_1 n_2}{2\pi \sigma_x \sigma_y}. \quad (2.1)$$

Here the n_b is the number of bunches, f_r the bunch-crossing frequency, n_1 and n_2 the number of protons per a bunch in each beam and σ_x and σ_y are the Gaussian profiles in each x and y axis.

2.2 Multiple proton-proton interactions (pile-up)

Due to properties of bunches at the LHC such as a beam profile, number of protons in a bunch etc., there is a significant probability of more than just one interaction per bunch crossing. This is known as a *pile-up*. It is made of soft-scale interactions which form a background to hard-scale interactions, such as high- p_T jet production. Since pile-up arises from multiple independent interactions, the effect of the high pile-up environment on a physics measurement can be inferred from studies of isolated soft interactions.

Using a collision rate, a total proton-proton cross section and an instantaneous luminosity, the mean number of interactions per bunch crossing can be calculated as

$$\mu = \frac{\sigma_{tot} \cdot \mathcal{L}}{f}. \quad (2.2)$$

Taking the nominal instantaneous luminosity value $\mathcal{L} = 10^{34} \text{cm}^{-2} \text{s}^{-1}$, the mean collision frequency $f = 31.5 \text{ MHz}$ and assuming the total cross section $\sigma = 100 \text{ mb} = 10^{-25} \text{cm}^2$, we get to approximately 32 interactions per bunch crossing.

The in-time pile-up discussed above (multiple interactions) is just one contribution to overall pile-up effects. Another one is so-called out-of-time pile-up, which is caused by superimposing signals being read-out from the detector in the current bunch crossing with part of the signal from a previous bunch crossing. This can happen when the signal response of a particular detector (such as calorimeter) is much longer than the frequency of bunch crossings.

2.3 The ATLAS Experiment

The ATLAS Experiment is by volume the largest detector currently installed at the CERN complex, having approximately 44m in length, 25m in height and weighting 7000 tonnes. Its forward-backward symmetry layout is shown in Figure 2.1. Going from the collision point outwards, it has onion-like design with concentric rings of detector layers covering almost the entire 4π solid angle. It was built as a general-purpose detector capable to measure as wide range of physics processes as possible. This section is dedicated to the more detailed description of its individual sub-detectors in more detail [15].

It is appropriate to introduce coordinate system and nomenclature first. The origin of the right-handed coordinate system is defined as the nominal interaction point, while the beam direction defines the z -axis and the $x-y$ plane is transverse to the beam direction. The positive x -axis points from the interaction point to the center of the LHC ring while the positive y -axis points upwards. The side-A (side-C) of the detector is defined as that with positive (negative) z . The azimuthal angle ϕ is measured around the beam axis while the polar angle θ is that from the beam axis. The pseudorapidity is defined as $\eta = -\ln \tan (\theta/2)$, in case of massive objects the rapidity is $y = \ln[(E + p_z)/(E - p_z)]/2$. The transverse quantities, such as a momentum p_T or an energy E_T , are defined in the $x-y$ plane. The distance in pseudorapidity-azimuthal space is defined as $\Delta R = \sqrt{\Delta\eta^2 + \Delta\phi^2}$.

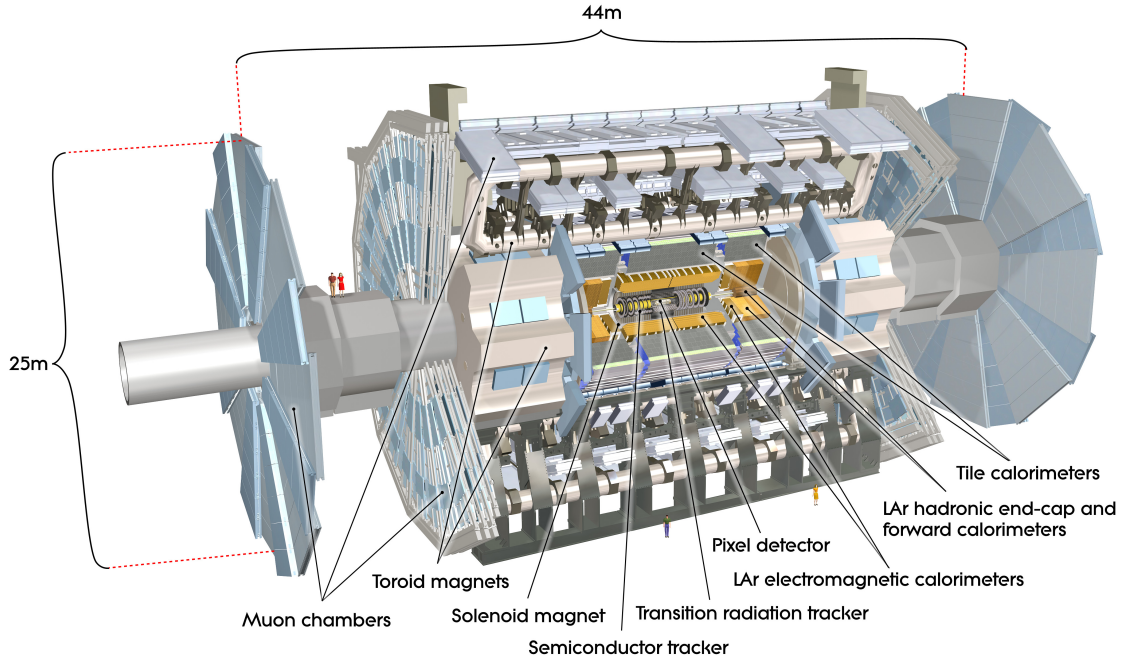


Figure 2.1: The ATLAS detector with its major sub-detectors [15].

2.3.1 The Inner Detector

The closest to the interaction point is the so-called Inner Detector (ID) [16] dedicated to the precision measurement of trajectories of charged particles. It is

designed to provide a robust tracking in a high radiation environment produced at the LHC luminosities. The ID consists of three different layers depicted in Figure 2.2, all of them placed in the magnetic solenoid field of the strength of 2 T. This detector system has to provide a sufficiently high resolution to identify secondary vertices associated with long lived states such as b -hadrons. The ID measurement range is within $|\eta| < 2.5$ and is especially effective for $0.2 \text{ GeV} < p_T < 150 \text{ GeV}$.

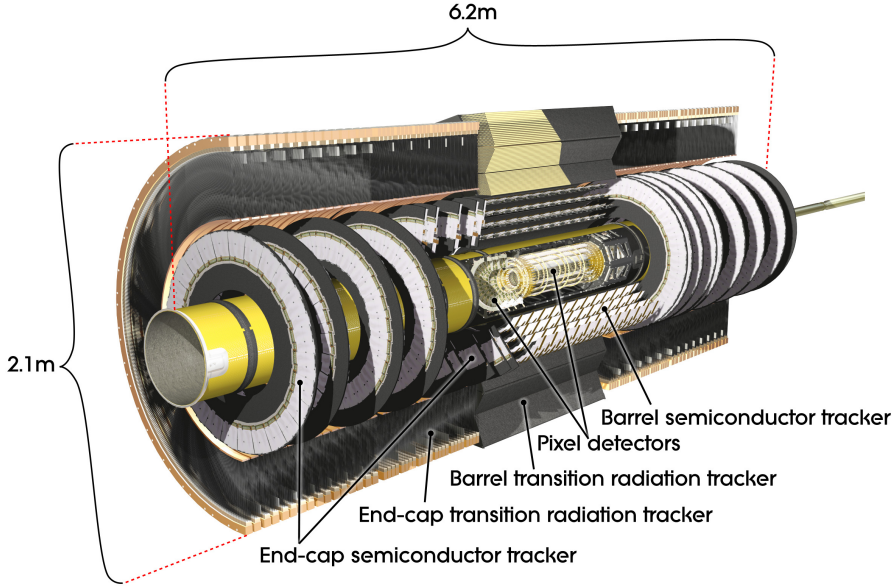


Figure 2.2: The layout of the Inner Detector with its subsystems [15].

To achieve the momentum and vertex resolution requirements, high-precision measurements must be made with fine detector granularity. The Pixel Detector (the closest to the beam) provides the highest granularity. The ATLAS experiment contains three pixel layers, each of which has pixels of nominal size $50 \times 400 \mu\text{m}$ with intrinsic accuracy of $10 \mu\text{m}$ in $R - \phi$ and $115 \mu\text{m}$ in z . The pixel detector has approximately 80.4 million readout channels.

The Pixel Detector is surrounded by the Semi-Conductor Tracker (SCT) with eight strip layers (providing four space points) crossed by each track. The mean pitch of the strips is approximately $80 \mu\text{m}$ yielding a $17 \mu\text{m}$ hit resolution in $R - \phi$ and $580 \mu\text{m}$ in z . The total number of readout channels in the SCT is approximately 6.3 million.

The outer part of the Inner Detector is made of the 4 mm wide straw tubes of the Transition Radiation Tracker (TRT). The transition radiation photons are emitted by charged particles passing through inhomogeneous media such as a boundary between materials with different dielectric constants. These are absorbed by the xenon-based gas mixture in the straw tubes. A large number of hits (typically 36 per track) is provided for particles with pseudorapidity up to $|\eta| < 2.0$, resulting in a comparable measurement precision to pixels and SCT in spite of the smaller TRT resolution. This is due to a better magnetic separation

at higher radii. The total number of TRT readout channels is approximately 351,000.

The precisions of the Inner Detector in the plane perpendicular to the z axis ($\sigma_{R-\phi}$) and in the longitudinal z direction (σ_z) are expected to be

$$\sigma_{R-\phi}(\mu\text{m}) = 13 \oplus \frac{62}{p_T \sqrt{\sin \theta}} \quad (2.3)$$

$$\sigma_z(\mu\text{m}) = 39 \oplus \frac{90}{p_T \sqrt{\sin \theta}} \quad (2.4)$$

2.3.2 Calorimeter system

The ATLAS calorimeter system is presented in Figure 2.4. All calorimeters installed are of the sampling type where regions of absorber material are alternated with active medium. This calorimeter systems covers the pseudorapidity range up to $|\eta| < 4.9$ utilizing different technologies. In the central part where there is an overlap with the Inner Detector, the calorimeters have high granularity to provide for a precision measurement of electrons and photons. Starting from the central pseudorapidities, there is an electromagnetic calorimeter covering a range $|\eta| < 3.2$, a hadronic barrel calorimeter covering $|\eta| < 1.7$, a hadronic end-cap calorimeter in the range of $1.5 < |\eta| < 3.2$ and a forward calorimeter in $3.1 < |\eta| < 4.9$. These segments are made of two different techniques satisfying different physics requirements and varying radiation environment: a scintillating technique in the barrel hadronic calorimeter and the liquid Argon (LAr) technique in the rest. The latter is more radiation resistant and is therefore more suitable for segments closer to the beam pipe.

Calorimeters are required to provide a good containment of electromagnetic and hadronic showers. Their dimensions are thus carefully chosen. For the EM calorimeter the total thickness is approximately 22 radiation lengths (X_0) in the barrel and 24 X_0 in end-caps. A good resolution of high energy jets can be achieved by the 9.7 interaction lengths (λ) of active calorimeter in the barrel (10 λ in the end-caps). The thickness together with the large η -coverage also ensures a good missing transverse energy measurement.

Electromagnetic calorimetry

The Electromagnetic Calorimeter (ECal) is dedicated to the measurement of the energy of electrons and photons. It consists of barrel part (covering $|\eta| < 1.475$) and two end-caps $1.375 < |\eta| < 3.2$). The EM calorimeter is using a liquid Argon as an active medium and an accordion-shaped kapton electrodes and lead absorbers for showering. The accordion symmetry provides complete ϕ coverage without cracks. The lead thickness of absorber plates has been optimized as a function of η to provide good performance in energy resolution.

Over the high precision measurement region which overlaps with the Inner Detector ($|\eta| < 2.5$), the ECal is segmented in three sections of high granularity.

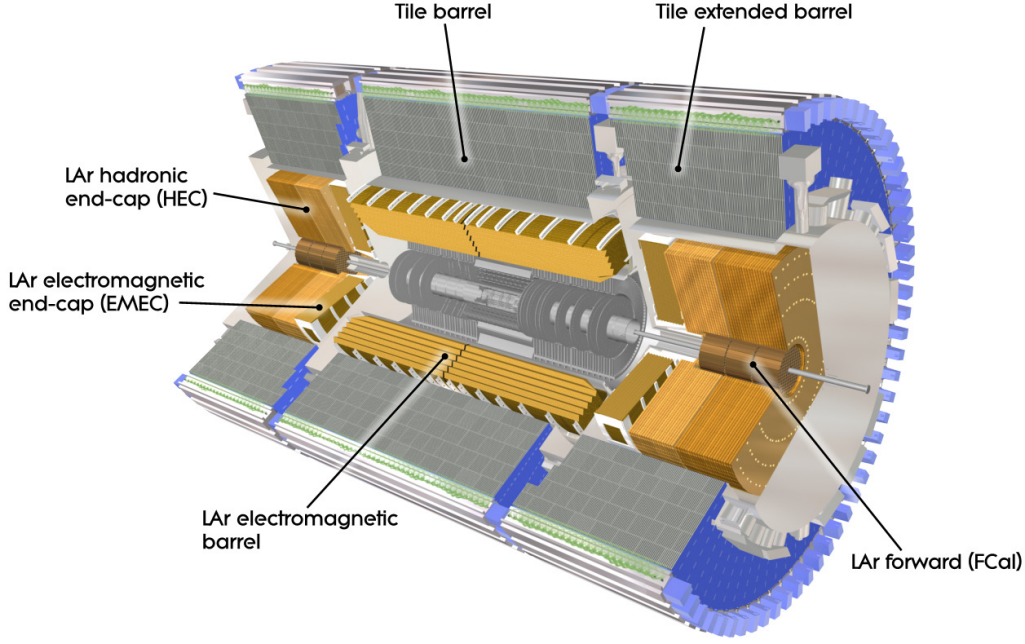


Figure 2.3: The ATLAS calorimeter system [15].

For the rest of the acceptance, the calorimeter is segmented in two sections with coarser granularity.

In the region of $|\eta| < 1.8$, a presampler precedes the ECal. It is used to correct for the energy lost by electrons and photons before reaching the EM calorimeter. The presampler consists of an active LAr layer of thickness 1.1 cm (0.5 cm) in the barrel (end-cap) region.

The energy resolution of the EM calorimeter, consisting of the sampling, noise and constant terms, was measured [17]

$$\frac{\sigma(E)}{E} = \frac{10\%}{\sqrt{E[\text{GeV}]}} \oplus \frac{0.39\text{GeV}}{E} \oplus 0.3\%. \quad (2.5)$$

Hadronic calorimetry

The hadronic calorimeters form another detector-layer right outside the ECal envelope. Both the LAr and steel-scintillator technology are used in the ATLAS hadronic system. It consists of the hadronic barrel (TileCal) covering $|\eta| < 1.7$, the Hadronic End-cap extending the range to $1.5 < |\eta| < 3.2$ and finally the Forward Calorimeter (FCal) in $3.1 < |\eta| < 4.9$.

Showers caused by hadrons consist typically of an electromagnetic component and a wider hadronic shower. The nuclear interaction length λ is introduced as a counterpart to the radiation length X_0 . It is a length scale required to reduce the hadron's energy by a factor of e . It is important in order to decide in the matter of the calorimeter thickness which should be big enough to absorb all

the energy of hadronic showers. Failing to do so would cause punch-throughs (a leakage of a part of the hadronic energy out of the calorimeter) to the muon system. Building the calorimeter with too high thickness would, on the other hand, cause an undesirable multiple scattering of muons affecting thus negatively the muon momentum measurement resolution. The total thickness of the hadronic calorimeter is 11λ at the $\eta = 0$. The amount of material in different calorimeter segments as a function of a pseudorapidity is shown in Figure 2.4.

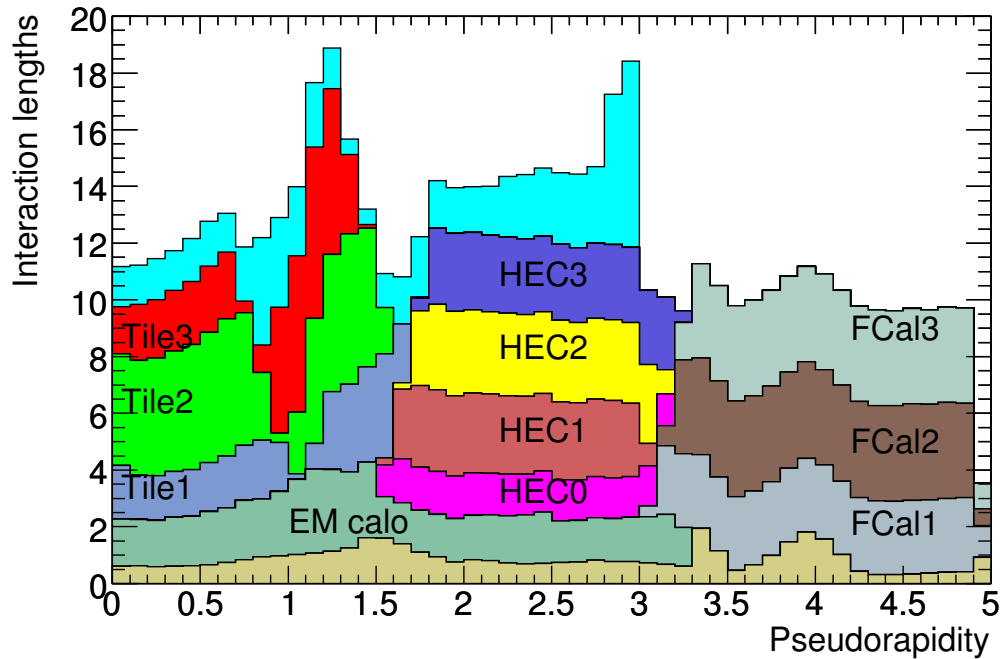


Figure 2.4: The amount of material in different calorimeters in units of interaction length λ ([15]). The material in front of the EM calorimeters is also shown, as well as the total amount of material in front of the first active layer of the muon spectrometer (up to $|\eta| < 3.0$).

The TileCal resolution was measured in a pion test beam [18] and found to be

$$\frac{\sigma(E)}{E} = \frac{52\%}{\sqrt{E[\text{GeV}]}} \oplus 5\%. \quad (2.6)$$

2.3.3 Muon chambers

The presence of a high p_T muon in the collision event is a signature of many Standard Model as well as Beyond Standard Model interactions. Their relatively easy measurement can be also exploited by trigger system (described later on in this Chapter). Muons originating in the interaction point in the center of the ATLAS detector leave hits in the Inner Detector and deposit energy in calorimeters before reaching the muon spectrometer located at the outer part of the ATLAS experiment. The general idea of the muon detection method is a measurement of a curvature of a muon track in the large superconducting air-core toroid magnets.

In the region $|\eta| < 1.4$, the magnetic bending is provided by the barrel toroid, while in the $1.6 < |\eta| < 2.7$ region there are two smaller end-cap magnets. In the $1.4 < |\eta| < 1.6$ transition region, the magnetic deflection is provided by combination of both barrel and end-cap fields. The magnetic field is designed to be orthogonal to the most of the muon flight directions. Toroids are instrumented with separate trigger and high-precision tracking chambers.

The ATLAS muon system is outlined in Figure 2.5. Over most of the pseudorapidity range, the precision tracking is provided by the Monitored Drift Tubes (MDTs). They are aluminium tubes of 30 mm in diameter filled with the argon gas and with a central tungsten wire. The position resolution provided is of $80\ \mu\text{m}$. At larger pseudorapidities, namely $2 < |\eta| < 2.7$, the Cathod Strip Chambers (CSCs) with larger granularity are used. CSCs are multi-wire proportional chambers with cathodes segmented into strips. Their position resolution is $60\ \mu\text{m}$.

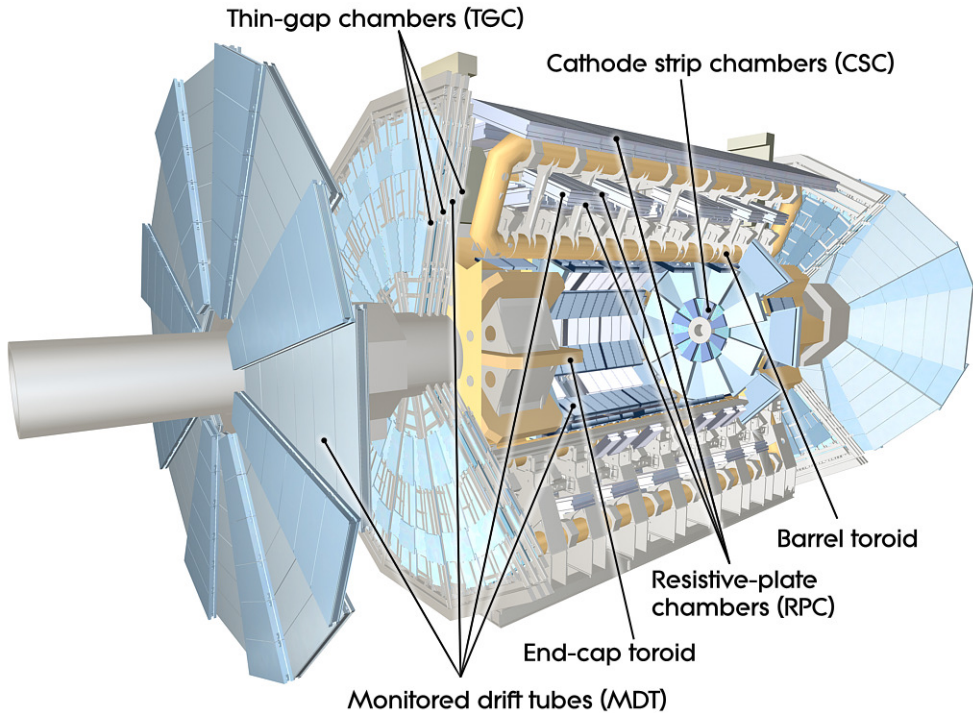


Figure 2.5: The ATLAS muon system [15].

The fast muon trigger system covering the $|\eta| < 2.4$ range consists of the Resistive Plate Chambers (RPCs) in the barrel region and the Thin Gap Chambers (TGCs) in the end-cap regions. The muon chambers provide, moreover, a position measurement in the orthogonal plane determined by the precision-tracking MDT chambers.

In overall, the required transverse momentum resolution for 1 TeV muons is

$$\frac{\sigma(p_T)}{p_T} = 10\%. \quad (2.7)$$

2.3.4 MBTS

The Minimum Bias Trigger Scintillator (MBTS) is a detector used for triggering on the so-called minimum bias events, that is events of any kind (soft as well as hard scale interactions). It consists of sixteen counters positioned symmetrically on both sides of the ATLAS detector, right on the inner face of the end-cap calorimeter cryostat. Each scintillator is segmented in eight units of ϕ (azimuthal plane) and two units of η (polar angle plane). They are located about 3.6 m from the interaction point in the longitudinal direction. The inner radii wheels cover $2.82 < |\eta| < 3.84$ region while the outermost wheels cover $2.09 < |\eta| < 2.82$. The MBTS counters can be also exploited as a veto for selecting exclusive diffractive events with large rapidity gaps.

2.4 ATLAS forward detectors

In addition to the main ATLAS detector systems described in previous sections, three smaller detectors were built to provide a coverage in the very forward region. They can serve the purpose of luminosity monitoring, absolute luminosity measurements as well as other forward physics studies. Besides these three detectors already installed in the LHC tunnel, others are in the approval process within the ATLAS Collaboration aiming at enhancing the forward physics studies possibilities. They are called ATLAS Forward Proton (AFP).

The general layout of the forward detector system is presented in Figure 2.6. The system closest to the interaction point is the LUCID (Luminosity measurement using Cerenkov Integrating Detector) located at a distance of 17 m from the interaction point on each side ($\pm z$). LUCID is followed by the ZDC (Zero Degree Calorimeter) at a distance of 140 m on each side of the IP. Finally, the most remote forward detector currently installed is the ALFA (Absolute Luminosity For ATLAS) at a distance of approximately ± 240 m.

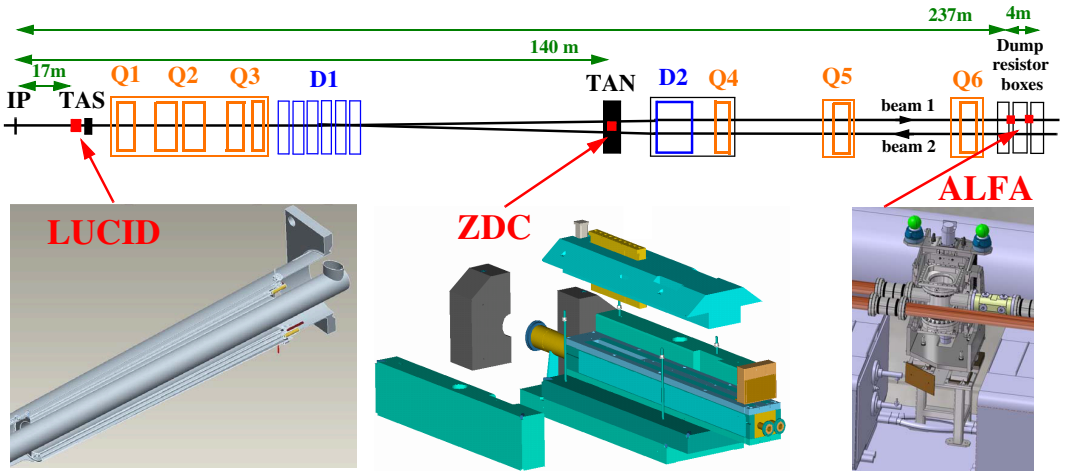


Figure 2.6: The forward detectors placement around the ATLAS interaction point [15].

2.4.1 LUCID

The LUCID is the only ATLAS detector primarily dedicated to the online luminosity monitoring via a detection of the inelastic pp scattering in the forward region. This detector has also a potential to be used for diffractive studies as a veto for selecting diffractive events with large rapidity gaps.

The LUCID detector consists of 1.5 m long tubes with a diameter of 15 mm surrounding the beam-pipe and pointing toward the interaction point. Tubes are filled with C_4F_{10} gas providing a Cerenkov threshold of 2.8 GeV for pions and 10 MeV for electrons. The Cerenkov light is detected by photomultipliers (PMTs) at the end of each tube. The benefit of this design is that it is possible to determine the number of passing-through particles by measuring the pulse height. The two detectors are installed in each end-cap region about 17 m from the interaction point and in the radial distance of about 10 cm from the beam-pipe. In this set-up the detector covers a pseudorapidity range $5.4 < |\eta| < 6.1$.

The instantaneous luminosity is measured from the detection of charged particles going into the forward direction, as well as their arrival time, in each bunch crossing. The principle that the number of particles detected is proportional to the number of inelastic interactions is exploited. One can thus measure not only the luminosity, but the average number of interactions per bunch crossing as well.

2.4.2 ZDC

The Zero Degree Calorimeter's primary purpose is to detect forward neutrons with $|\eta| > 8.3$ in heavy-ion collisions. Besides this, it can also help with a beam tuning, luminosity monitoring and triggering on minimum bias events. It can also enhance, during the LHC start-up phase, the acceptance of the ATLAS experiment for diffractive processes.

This detector, positioned about ± 140 m from the interaction point, is a segmented electromagnetic and hadronic calorimeter corresponding to about $29 X_0$ radiation lengths and 1.14λ nuclear interaction length respectively. The ZDC has tungsten plates perpendicular to the beam direction, steel plates as an absorber and quartz strips as an active medium. The PMTs and multi-anode phototubes collect the Cerenkov light from shower products of incident particles.

2.4.3 ALFA

The ALFA detector exploits the optical theorem connecting the elastic scattering amplitude in the forward direction to the total cross section. Thus, the ALFA can measure the absolute luminosity via the elastic scattering at small angles. Special runs with high β^* optics in combination with reduced beam emittance are necessary and, moreover, the detector has to be placed far away from the interaction point and as close to the beam as possible. The Roman pots technique has been adopted. It consists of a movable detector volume (the pot) separated

from the vacuum of the beam pipe by a thin window and it is able to move as close as 1 mm to the beam. The main requirements on the detector placed in the Roman pots are a spatial resolution (about $30\ \mu\text{m}$), no significant inactive edge region, minimal sensitivity to the radio-frequency noise from the LHC beams and a compatibility with the vacuum in the Roman pots. Therefore, a scintillating-fibre tracker has been chosen.

2.5 Data acquisition and trigger system

The typical average event size when collecting information from all the ATLAS sub-detectors is about 1.5 Mbytes. That gives, at nominal design conditions such as bunch collisions every 25 ns with up to 30 interactions per bunch crossing, the data rate of about $1.5\ \text{PB s}^{-1}$. This amount of data flow is too large to be processed and stored, given the current level of computing technology. Therefore, an event selection procedure called trigger system has been developed to provide a significant reduction of data to be processed, stored and eventually transferred to the Grid system (see Section 3.1) for end-user analysis. The aim is to reduce the original event rate from 40 MHz to about 200 Hz (equivalent to $\sim 300\ \text{MB/s}$) which is achieved by the three level trigger system comprising Level 1 (L1), Level 2 (L2) and finally the Event Filter (EF). The L2 and EF together form the so-called High-Level Trigger (HLT) and are software based, while the L1 trigger is hardware-based.

The Level 1 trigger provides a fast decision based on the potential signal identification in parts of the calorimeters and muon detectors of reduced granularity. This coarse analysis lies in searching for signatures of high- p_T muons, electrons, photons, jets and τ -leptons decaying into hadrons. Another signal candidates of interest are events with large missing transverse energy E_T^{miss} . Altogether, the L1 trigger decision has to be made within $2.5\ \mu\text{s}$ from the time of the collision, reducing the accept rate to 75 kHz. This task is far from trivial as, for example, the muon arrival time to muon chambers is comparable with the collision rate 25 ns. Similar situation occurs with reading-out signals from the LAr calorimeter. For this reason of the latency in trigger decision with respect to the bunch crossing rate, the information from all the read-out channels has to be stored in a buffer, the so-called pipeline memory. Once the decision is reached, the event can be thrown away or on the contrary - the front-end electronics can be signaled to retrieve and transmit the data from the pipeline.

The Level 2 trigger is seeded by the Level 1. Around each seed, the Region-of-Interest (RoI) window of the size depending on the type of the seed object is constructed. The L2 then performs a refined analysis of the L1 object and, moreover, adds an additional information not accessible in the L1 trigger decision analysis, such as track reconstruction from the Inner Detector. The L2 decision is reached, on average, within 40 ms and it reduces the event rate to below 3.5 kHz.

The last stage of the ATLAS trigger system, the Event Filter, performs a detailed analysis on the L2 candidates. Unlike in the L1 and L2 case, the full information

from all the sub-detectors is available. The EF decision has an average processing time of the order of four seconds and it reduces the event rate down to about 200 Hz. This data can then be recorded to hard drives and made available to end-users for physics analyses.

To refine the trigger selections, the HLT algorithms take advantage of the full granularity of calorimeters and muon chambers, as well as the measurements provided by the Inner Detector. Thus, the improvement of threshold cuts due to a better energy deposition information or an enhancement of the particle identification (such as electrons vs. photons) benefiting from the precise track reconstruction in the Inner Detector can be achieved. In early stages of the LHC running, i.e. at low instantaneous luminosities and low number of bunches in bunch trains, the HLT triggers operated in pass-through mode allowing thus to understand and tune the L2 and EF functionality.

3. Software and computing

Even though the complex trigger system has been put in place in order to pre-select potentially interesting events only, the event rate that needs to be recorded is about 200 Hz. Given the scale of the ATLAS experiment and an extensive amount of active detector channels needed to be read-out, these 200 events per second represent 300 MB/s (15 Petabytes per year) that need to be handled: stored, calibrated, reconstructed and eventually analysed by a large scientific community spread around the world. Therefore, a very sophisticated software framework and hardware facilities are essential for manipulating the acquired data.

3.1 Distributed grid computing

No existing single super-computer nor any computing farm composed of chained PCs can provide a sufficient CPU power and a storage capacity for a data taking over many years. Therefore, the CERN and collaborating institutes have been working on a development of a world-wide computing network connecting together hundreds of originally isolated computing farms into a network called the LHC Computing Grid (LCG) [19], also known simply as the Grid. This network is large enough to provide sufficient computing power not only to the CERN community, but also to other scientific endeavours, such as bioinformatics (study of human genome and proteome), nanotechnology (design of nano-materials), medical applications (imaging, diagnosis and treatment), the SETI project (Search for Extraterrestrial Intelligence; analysis of data from radio telescopes) or simulations of complex systems (meteorological and atmospheric modeling, earth observation, ...).

The Grid is a complex four-level structure of so-called “Tier” centers. The Tier-0, located at CERN, is at the very top of the system where all the data collected by LHC experiments are stored and where a first processing of the data occurs. The raw data as well as the pre-processed data are then distributed in several copies to Tier-1 centers, large regional computing farms spread around the world. Tier-1 sites are connected to Tier-0 via a dedicated 10 Gb s^{-1} network and provide, besides partial or full copies of the collected data, a significant computational power for re-reconstruction with newer calibrations and reconstruction algorithms. The third level are smaller Tier-2 sites, located usually at collaborating universities and institutes. They hold fully reconstructed data in formats used by end-users (physicists) who can connect to the Grid via small university clusters or individual computers. This is the third level called Tier-3.

3.2 ATLAS framework

Given the complexity of all sub-detectors, calibrations, reconstruction algorithms, simulation methods etc., a unified software framework called ATHENA [20] has

been created by the ATLAS Collaboration for its members. It is build upon an existing framework Gaudi. The baseline programming language is the C++, in which all individual software packages are written. The Python scripting language acts as a key user interface allowing to control the ATHENA framework along with all its packages.

The ATHENA provides, among others, a modeling software called *full-chain*. It is an event reconstruction procedure allowing to produce fully reconstructed files ready for a physics analysis. It can be based on both the data and the Monte Carlo simulated events. Speaking of the MC events, generated particles are first passed through the Geant4 [21] simulation of the ATLAS detector (modeling of a passage through the ATLAS sub-detectors as well as a dead material, magnetic fields etc.), simulating thus the energy deposition in active parts of sub-detectors. These so-called “hits” are then digitalized into a byte-stream format of the same type as the data digitization procedure provides and stored as Raw Data Objects (RDO) files. The following steps are then the same in both the data and the MC events: the entries in RDO files are converted into physics objects such as tracks, jets, electron and muon candidates etc. and stored into the Event Summary Data (ESD) files. The ESD is the most comprehensive data format which contains a sufficiently detailed information allowing a re-reconstruction when needed. They are not, however, used for an end-user physics analysis due to their large size. Therefore, an Analysis Object Data (AOD) files are created by keeping only the information relevant for end-user analyses. It is possible to further reduce the size of datasets by keeping only the essential physical information: such format is called Derived 3rd level Physics Data (D3PD).

3.3 D3PD production

The measurement presented in this thesis is primarily based on analysing the D3PD files as an input to the C++ based analysis framework developed specially for the sake of this measurement. Most of the computing resources used to process the 2010 data and Monte Carlo simulations come from the computing farm called Goliáš (located at the Institute of Physics of the Academy of Sciences in Prague) and acting also as the Tier-2 Grid site. The direct access provided to Czech scientists allows much more efficient and faster usage of available resources than via an official Grid structure. However, the Grid resources have been also used, especially for a dedicated Monte Carlo production (see Chapter 4) and a new production of the D3PD files. New production of the D3PD files was essential as the rapidity gap analysis requires, as is explained in Chapter 6, a specific variable called “cell significance” being present in the datasets, which is not there by default. All the data used for this measurement were therefore reproduced from the existing ESD files by running the D3PD-maker in Athena’s release 16.0.3.6.1 using the *JetMetAnalysis* package.

3.4 ROOT

The ROOT system [22] is an object-oriented framework developed by René Brun and Fons Rademakers. It is currently the most commonly used data analysis software in the particle physics community, specifically designed to allow an efficient way of processing the huge amount of data coming from the LHC experiments. Due to its liberal development style, it is possible to think of ROOT as the analysis system developed by physicists for physicists, which makes it very useful and powerful tool for the use by scientific community members.

A significant advantage of the ROOT framework is a built-in C++ interpreter CINT, meaning that one does not need to learn another programming language, but rather use the interactive command line mode, scripting or macros in a way familiar and friendly to the current physicist surrounded by the C++ based software (such as Athena). It is also easy to include ROOT libraries into a C++ based analysis code and thus use the powerful ROOT tools (namely histogram classes, random number generators, math functions, objects for an efficient storage of data called “trees”, etc.) for a systematic structured object-oriented offline data analysis. This is also the case of the analysis summarized in this thesis.

4. Monte Carlo simulations

4.1 General Monte Carlo concepts

Monte Carlo simulation methods are, in general, mathematical tools exploiting numerical methods for demanding calculations. They are used to solve problems that are too complicated to be solved analytically, for example multidimensional integrals over parton densities. In contrast to other simulation methods, these ones are stochastic (nondeterministic) - their nature is in generating suitable (pseudo-)random numbers. Monte Carlo methods are especially effective in solving problems with a large number of degrees of freedom. Their efficiency relative to other numerical methods increases with increasing dimension of the problem.

In nuclear and particle physics (or, more accurately, in processes involving quantum mechanics) a concept of randomness plays a key role in a behaviour of physical systems and Monte Carlo techniques allow us to simulate this randomness. The essential part of event generator is thus a random number generator, in practice substituted by a pseudo-random number generator, which is able to approximate random numbers by complex algorithms which always start from a user-defined “seed”, i.e. the starting value.

There is a lot Monte Carlo generators available for particle scattering simulations. Some of them are generators dedicated to a particular physical process while others, such as PYTHIA8 and HERWIG++ discussed later in this chapter, are multipurpose generators capable of modeling a large range of physical processes.

4.2 PYTHIA8

The PYTHIA8 [23] Monte Carlo generator implements the modelling of elastic, non-diffractive and diffractive (both the SD and the DD) processes. It also contains a model of the Underlying Event (UE) using the multi-parton interactions (MPI; multiple soft scatters in one event) as well as parton showering models.

At the end of the parton shower, quarks and gluons have to be transformed into the observable hadrons. For such hadronisation process, PYTHIA8 uses the phenomenological Lund string model [24]. In the Lund model, gluons are treated as color field lines which create, in contrast to the electromagnetic field lines that spread out over all space, a thin tubelike region of colour flux. This is happening due to the three-gluon coupling (gluon self-interaction), a process which has no analogy in electromagnetic interactions. In case of the $q\bar{q}$ pair with quarks moving apart from each other, the tube of color flux is being stretched out like a string (therefore the “string model”), up to a point where it breaks and a new $q\bar{q}$ pair is created from the available field energy. The original $q\bar{q}$ system keeps breaking via this process up to the point where only ordinary hadrons remain.

The PYTHIA8 samples were generated using the “ATLAS UE Tune AU2-CT10” tune [25]. It is based on previous “Tune 4C” [26] (reflecting CDF data), but modified to be more suited to LHC conditions.

4.2.1 Non-diffractive modelling

The ND interactions are simulated with the leading-order perturbative $2 \rightarrow 2$ partonic scatters. For small transverse momenta, the cross section is divergent and therefore a renormalization by introducing the $p_{T,\min}$ cut is necessary. Other processes such as colour screening or parton saturation simulation are introduced. By default, the CTEQ10 PDFs [27] are used.

4.2.2 Diffractive modelling

In the PYTHIA8, both the soft and hard diffraction are implemented. While the soft diffraction comes from the PYTHIA6 [28] and is based on the Schuler-Sjöstrand [29] model (having an exponential t dependence), the hard diffraction treatment in PYTHIA8 is significantly improved and the Ingelman-Schlein model [30] is used. In general, PYTHIA8 is better adjusted for the LHC environment than PYTHIA6 and is thus used as a default PYTHIA generator by the ATLAS Collaboration.

The diffraction in PYTHIA is calculated as a combination of the pomeron flux of the pomeron radiated from one of the interacting protons and a pomeron-proton interaction. In the SD and DD cross section, a triple-pomeron coupling factor and an exponential t dependence are present. By default, the H1 2006 Fit B Leading Order DPDFs is used [9].

PYTHIA8 currently provides an implementation of five different pomeron fluxes. The default one is the Schuler-Sjöstrand [29] flux with the pomeron intercept $\alpha_{\mathbb{P}}(0) = 1$. The Bruni and Ingelman flux [31] has also the pomeron intercept of unity, but the t slope is modeled by a sum of two exponentials. The remaining three fluxes use more conventional values of the pomeron intercept, that is $\alpha_{\mathbb{P}}(0) > 1$. The Berger and Streng parametrization [32] [33] uses as default $\alpha_{\mathbb{P}}(0) = 1.085$ and the pomeron trajectory slope $\alpha' = 0.25 \text{ GeV}^2$ with the diffractive slope exponential in t , but with an additional mass dependence. The Donnachie and Landshoff flux [5] uses the same mass dependence and $\alpha_{\mathbb{P}}(t)$ as the Berger and Streng, but instead of the exponential t dependence a power law t dependence is used. Finally, the Minimum Bias Rockefeller (MBR) parametrization [34] following a renormalized-Regge-theory model successfully tested using CDF data is implemented with the default $\alpha_{\mathbb{P}}(0) = 1.104$ and $\alpha' = 0.25 \text{ GeV}^2$ values.

4.3 Herwig++

The Herwig++ [35] is, such as PYTHIA, a multi-purpose MC generator dealing with hard lepton-lepton, lepton-hadron, and hadron-hadron collisions and aiming to provide similar or improved simulation compared to PYTHIA, such as using

the angular ordered (in η and E) parton shower evolution or the cluster hadronisation model. It also contains, similarly to PYTHIA, an UE model in which multiple scatters are treated as independent of each other.

In Herwig++, a so-called cluster hadronisation model is implemented. Partons from parton showering are combined to form color singlet quark-antiquark pairs - called clusters - with the momentum given as a sum of momenta of the constituent partons. Such clusters have mostly low masses and can be regarded as excited hadronic resonances, which can decay into observable hadrons. Some clusters are, however, too heavy for this direct approach and must be first split to lighter clusters before final hadrons can be produced. As an addition to this basic model, the Colour Reconnection (CR) mechanism has been introduced to improve modelling of charged particle multiplicities in pp collisions via reconnecting partons between cluster pairs.

The hard diffraction is modeled using the Ingelman-Schlein parametrization with default values of the pomeron intercept $\alpha_{\mathbb{P}}(0) = 1.104$ and the trajectory slope $\alpha' = 0.06 \text{ GeV}^2$. These parameters can be, just as in PYTHIA, adjusted by the user. The implemented DPDFs are based on H1 2006 A, 2006 B and 2007 Jets fits.

4.4 POMWIG

The POMWIG generator [36] v2.0 beta is actually a HERWIG [37] (the older Fortran version) modified in such a way that diffractive interactions can be simulated. All standard Herwig hard subprocesses are available for pomeron-proton, photon-pomeron and pomeron-pomeron collisions, reggeons were also made available.

The idea behind POMWIG is based on a simple observation: interactions with an exchange of the pomeron in hadron-hadron collisions are similar to the photo-production in lepton-hadron events, which are modeled by radiating a quasi-real photon (according to the photon flux formula) by the incoming electron. The emitted photon is then treated as an object with structure function entering the collision with the incoming hadron. Therefore, all that is needed to be done to produce a diffractive event in pp collision is to substitute the photon flux with the pomeron flux and the photon structure function by the pomeron structure function. All that remains to do is to run the Herwig in ep mode, where the electron can be thought of as the diffractive proton remaining intact after the diffractive scattering.

The diffractive PDFs and the pomeron flux implemented in POMWIG are based on the result of the NLO H1 2006 fit B [9].

4.5 POWHEG

The POWHEG [38] (Positive Weight Hardest Emission Generator) is a framework implementing the next-to-leading order calculations of the dijet production in hadron collisions. It is based on generating the hardest radiation first and then providing the result to other shower generators for subsequent softer radiation modelling, such as PYTHIA6, PYTHIA8, Herwig++ or HERWIG+Jimmy [39].

This NLO MC generator was used in the physics analysis presented in this thesis to provide additional ND predictions to the existing LO PYTHIA8.

4.6 Monte Carlo event generation of diffractive dijet events

Since diffractive processes are not well understood yet, there is a wide range of models with different implementations, parameters, hadronisation models etc. giving rather different predictions, as shall be discussed later on. For this reason, having several MC models for comparisons with data is very advisable. However, the Monte Carlo dijet samples generated by the ATLAS Collaboration for proton-proton collisions at $\sqrt{s} = 7$ TeV turned out insufficient with respect to the model variety and statistics in our regions of interest (large rapidity gaps, small ξ). Therefore, a new production was necessary, both the full chain ATLAS detector simulation as described in Section 3.2 and private hadron level MCs for final comparisons to fully corrected data.

4.6.1 ATLAS Monte Carlo request

One of the ways how to get new Monte Carlo samples is to submit an official request to the ATLAS production team, while having an approval of such a request by a particular physics group related to the topic of the analysis. The advantage of this approach is that the full chain detector simulation, which is very complex (many parameters, software versions, detector geometries, etc.), is done by ATLAS experts and thus trusted by the whole Collaboration.

Such request was submitted to provide us with PYTHIA8 ND, SD and DD and Herwig++ ND and SD dijet samples at $\sqrt{s} = 7$ TeV. The ATLAS detector geometry was chosen such that it corresponds to 2010 layout. All samples are generated with one pp interaction per event only, that is without pile-up (not more than one pp interaction per bunch crossing). The diffractive samples were generated using diffractive parton distribution functions based on HERA measurement (see Section 1.3.3) and the Schuler-Sjöstrand pomeron flux parametrization was used for PYTHIA8 generation.

To achieve a sufficiently high statistics of events with large gaps (small ξ), a rapidity gap filter has been implemented. It is designed to filter events generated by PYTHIA8 (Herwig++ respectively) so that only a subset of events is stored into the output files. The subset is chosen in such a way that the generated ra-

pidity gap spectrum is flat (instead of exponentially falling) for smaller gap sizes ($0 < \Delta\eta^F < \Delta\eta_{\text{Thr}}^F$, where “Thr” stands for “Threshold”). The particle level rapidity gap algorithm is similar to the one discussed in Chapter 7, except that it takes into consideration all final state particles (full sensitivity to the real rapidity gap in the event) within the ATLAS acceptance ($|\eta| < 4.9$). For events in the region where the filtering is applied, a specific weight that needs to be applied to get a correct cross section is stored as well.

Since this is a dijet measurement, a standard ATLAS procedure is followed regarding requirements on hard scale. In case of PYTHIA8 ND samples, that means generating events in five different ranges of transverse momentum of the outgoing partons from the hard interaction (\hat{p}_T). This cannot be done for SD and DD samples due to the way PYTHIA8 generates them (it uses models of both soft and hard interactions, which cannot be separated so inclusive samples are produced). The way around is using jet filter which which reconstructs particle level anti- k_T $R = 0.4$ jets and allows thus to put requirements on jet transverse momenta (three different ranges with $p_T > 12$ GeV were generated). The normalization to cross section is then done by multiplying the generated cross section of the process the mean generator filter efficiency. Details of the generated and reconstructed samples are listed in Tables 4.1-4.3.

\hat{p}_T (GeV)	Jet ID	Run Number	$\Delta\eta_{\text{Thr}}^F$	Events generated	Events recon.	Cross section [nb]	Mean Gen. Filter Eff.
8-17	J0	147251	3.0	200000	199848	6.803×10^6	2.286×10^{-6}
17-35	J1	147252	4.0	600000	600000	5.210×10^5	2.217×10^{-4}
35-70	J2	147253	4.0	200000	198948	3.392×10^4	2.364×10^{-4}
70-140	J3	147254	4.0	100000	100000	1.923×10^3	1.694×10^{-4}
140-280	J4	147255	4.0	100000	99949	8.136×10^1	1.849×10^{-4}

Table 4.1: Details for PYTHIA8 non-diffractive samples generated with the forward gap filter.

p_T^{jet} (GeV)	Jet ID	Run Number	$\Delta\eta_{\text{Thr}}^F$	Events generated	Events recon.	Cross section [nb]	Mean Gen. Filter Eff.
12-20	J0	147256	5.0	300000	293950	1.238×10^7	4.980×10^{-6}
20-30	J1	147257	4.5	500000	400599	1.238×10^7	3.112×10^{-6}
30+	J2	147258	3.5	299300	179250	1.238×10^7	2.348×10^{-6}

Table 4.2: Details for PYTHIA8 single diffractive samples generated with the forward gap filter and jet filter.

4.6.2 Private MC production

A much simpler MC production than the full chain simulation is a private particle level generation. Such production is useful for creating MC predictions of high statistics for comparison with fully corrected data. Generators of interest for the diffractive dijet analysis are PYTHIA8 SD and DD for different pomeron

p_T^{jet} (GeV)	Jet ID	Run Number	$\Delta\eta_{\text{Thr}}^F$	Events generated	Events recon.	Cross section [nb]	Mean Gen. Filter Eff.
12-20	J0	147259	4.5	300000	269947	8.105×10^6	1.044×10^{-5}
20-30	J1	147260	4.5	408600	339647	8.105×10^6	4.026×10^{-6}
30+	J2	147261	3.5	300000	196950	8.105×10^6	2.343×10^{-6}

Table 4.3: Details for PYTHIA8 double diffractive samples generated with the forward gap filter and jet filter.

fluxes and $\alpha_{\mathbb{P}}$, POMWIG (providing additional SD model) and POWHEG (ND NLO samples).

5. Testing the Jet Energy Scale using dijet events

An important part of the PhD research summarized in this thesis consisted of a performance work within the Jet Eta-intercalibration subgroup of the ATLAS Jet and Missing E_T Group. It was focused on testing the quality of energy calibration of jets in 2010 and early 2011 data and as such, it provided the author of these lines a valuable insight into details of the jet reconstruction by the ATLAS calorimeter system, which was eventually exploited later on for the rapidity gap analysis in dijet events.

The results presented in this chapter contributed to two ATLAS internal notes, [40] and [41]. They were also presented at the 2011 ATLAS Hadronic Calibration Workshop held in SLAC National Accelerator Laboratory and as such they were valued by the ATLAS Collaboration.

5.1 Introduction to the in-situ pseudorapidity intercalibration method

The ATLAS calorimeter system, described in detail in Section 2.3.2, is represented by several layers with different technology and varying amount of dead material in front of them. Therefore, the response to jets is dependent on the jet direction and a calibration is needed to ensure uniform calorimeter response. This is achieved by applying correction factors (so-called Jet Energy Scale, denoted as JES) derived from Monte Carlo simulations. One of the validation methods of the JES is the in-situ pseudorapidity intercalibration method [42], to which this Chapter is dedicated. It is based on the transverse momentum conservation assumption in the head-on high-energy proton-proton collisions at $\sqrt{s} = 7$ TeV, which is exploited by studying dijet events, in which the transverse momenta of the two jets are expected to be balanced.

5.1.1 Standard method

The standard approach is to define the reference jet (required to be in the central region, $|\eta| < 0.8$) and the probe jet (jets from other regions) and calculate the transverse momentum asymmetry A as

$$A = \frac{p_T^{\text{probe}} - p_T^{\text{ref}}}{p_T^{\text{avg}}} , \quad (5.1)$$

where $p_T^{\text{avg}} = (p_T^{\text{probe}} + p_T^{\text{ref}})/2$. In case of both jets being in the central region, each jet is used, in turn, to probe the other. The average asymmetry in the reference region is, therefore, zero by construction.

The probe jet response relative to the reference jet, $1/c$, is then defined as

$$\frac{p_T^{\text{probe}}}{p_T^{\text{ref}}} = \frac{2 + A}{2 - A} = \frac{1}{c} . \quad (5.2)$$

The standard analysis is then done in several jet η and p_T^{avg} bins, resulting in an asymmetry distribution A_{ik} (i represents probe jet η -bin and k corresponds to p_T^{avg} -bin). Following Equation 5.2, the intercalibration factors are calculated as

$$c_{ik} = \frac{2 - \langle A_{ik} \rangle}{2 + \langle A_{ik} \rangle} , \quad (5.3)$$

where the mean value of the asymmetry in each $\eta - p_T^{\text{avg}}$ bin is denoted as $\langle A_{ik} \rangle$. The uncertainty of such mean value is calculated as the RMS/\sqrt{N} , with N being the number of events in the bin.

5.1.2 Matrix method

The above discussed method has a significant disadvantage: a significant loss of statistics due to the requirement that the reference jet is in the central region. This affects especially the forward region as it requires a large rapidity interval between jets, which has significantly lower cross section than dijets with small rapidity difference. To better use the available statistics, reference and probe jet definitions are replaced by “left” and “right” based on their pseudorapidities, $\eta^{\text{left}} < \eta^{\text{right}}$. The asymmetry is then defined as

$$A = \frac{p_T^{\text{left}} - p_T^{\text{right}}}{p_T^{\text{avg}}} \quad (5.4)$$

and the relative response R is calculated as

$$R = \frac{p_T^{\text{left}}}{p_T^{\text{right}}} = \frac{c^{\text{right}}}{c^{\text{left}}} = \frac{2 + A}{2 - A} , \quad (5.5)$$

where c^{left} (c^{right}) are the η -intercalibration factors for the left (right) jets.

This approach to the intercalibration leads to a response ratio distribution, R_{ijk} , which has an average value $\langle R_{ijk} \rangle$ evaluated for each bin i (η of the left jet), j (η of the right jet) and k (p_T^{avg}). The relative correction factors c_{ik} for a fixed p_T^{avg} -bin are obtained by minimizing a set of linear equations

$$S(c_{1k}, \dots, c_{Nk}) = \sum_{j=1}^N \sum_{i=1}^{j-1} \left(\frac{1}{\Delta \langle R_{ijk} \rangle} (c_{ik} \langle R_{ijk} \rangle - c_{jk}) \right)^2 + X(c_{ik}) , \quad (5.6)$$

where N is the number of η -bins, $\Delta \langle R \rangle$ is the statistical uncertainty of the $\langle R \rangle$ and the function $X(c_{ik}) = K(N^{-1} \sum_{i=1}^N c_{ik} - 1)^2$ (the value of constant K does not influence the solution if it is sufficiently large, $K \approx 10^6$) is used to prevent the minimization from choosing the trivial solution (all c_{ik} equal to zero). The minimization is done for each p_T^{avg} -bin (k) by running 50 pseudo-experiments (to limit statistical fluctuations due to the Gaussian smearing used in the procedure). The final factors c_i (per η -bin i) are scaled in such a way that the average calibration factor in the reference region $0.1 < |\eta| < 0.8$ equals unity.

5.2 Event selection

Jets are reconstructed using the anti- k_T algorithm [43] with the distance parameter $R = 0.6$. The default calibration is EM+JES (though others such as GCW+JES and LC+JES were evaluated as well, see the Section 5.4), which uses the energy and η dependent factors derived from fully simulated PYTHIA6 events by matching particle level jets (reconstructed from the information in the MC event record) with calorimeter jets at the EM-scale¹; the correction factors are calculated as a ratio of true particle jet energy and the EM-scale jet energy.

Events are required to pass the standard ATLAS data-quality assessment procedure and only those with one good primary vertex (i.e. vertex having at least five associated tracks with $p_T > 500$ MeV) are allowed to enter the analysis. A presence of at least two jets above the jet reconstruction threshold of $p_T > 7$ GeV is requested, both of which have to pass the standard jet cleaning criteria, which are designed to identify fake jets due to the noise or out-of-time energy deposition². Finally, the trigger selection detailed in Table 5.1 is tuned in such a way that the trigger efficiency for a specific p_T region is greater than 99%. That is achieved by using the Minimum Bias Trigger Scintillators (MBTS) for low- p_T jets and jet triggers (central and forward ones) for higher- p_T jets.

p_T (GeV)	Period A	Periods B-D	Periods E5-F	Periods G-I
20 - 45	L1_MBTS.1	L1_MBTS.1	L1_MBTS.1	EF_mbMbts.1_eff
45 - 60	L1_MBTS.1	L1_J5 or L1_FJ5	L1_MBTS.1	EF_mbMbts.1_eff
60 - 80	L1_MBTS.1	L1_J10 or L1_FJ10	L1_J10 or L1_FJ10	EF_J35_jetNoEF or EF_FJ30_jetNoEF
> 80	L1_MBTS.1	L1_J15 or L1_FJ15	L1_J30 or L1_FJ30	EF_J35_jetNoEF or EF_FJ50_jetNoEF

Table 5.1: Trigger selection used for the η -intercalibration dijet analysis.

There are three additional criteria whose purpose is to ensure the $2 \rightarrow 2$ event topology:

- $p_T > 20$ GeV
- $\Delta\phi(j_1, j_2) > 2.6$ rad (azimuthal angle between the two highest- p_T jets j_1, j_2)
- $p_T(j_3) < \max(0.15p_T^{\text{avg}}, 7\text{GeV})$ (j_3 is the third highest- p_T jet)

The lowest p_T^{avg} bins are influenced by biases. One of the sources is the inefficiency of the selection cut on the third jet (used to suppress the unbalancing effects of soft-radiation) due to the jet reconstruction being limited to the region of $p_T^{\text{avg}} > 7$ GeV. Another effect is the jet reconstruction efficiency, which deteriorates with decreasing jet transverse momentum. The third source of bias for low p_T jets is the inaccuracy of the Jet Energy Scale for $p_T < 10$ GeV jets.

5.3 Monte Carlo simulations

Results from the analysis of the data are compared to various MC models, namely PYTHIA6, HERWIG++ and ALPGEN. This allows to compare the measurement

¹The electromagnetic scale (EM) gives the correct energy response from electromagnetic showers, but does not correct for lower hadron response.

²More on out-of-time pile-up in Chapter 11

with different approaches to parton showering, hadronisation etc. PYTHIA6 implements leading-order matrix elements from perturbative QCD for $2 \rightarrow 2$ processes, parton showers in leading-logarithm approximation and uses the Lund string model for hadronisation. Two sets of PYTHIA6 samples are available: the ATLAS MC10 and the Perugia2010 tune. HERWIG++ has similar $2 \rightarrow 2$ matrix element, but uses angular-ordered parton shower and a cluster hadronisation model. ALPGEN uses the same parton showering and hadronisation as HERWIG++. All these MC events, generated at the center-of-mass energy $\sqrt{s} = 7$ TeV, were fully reconstructed using the same procedure as for the reconstruction of the data.

5.4 Results

5.4.1 Dijets in 2010 data

This η -intercalibration analysis started with two goals: to finalize studies based on 2010 data that were performed within the Eta-intercalibration subgroup and to apply the acquired know-how on latest 2011 data. Studies of 2010 data were so far focused on EM+JES calibration and anti- k_T jet reconstruction algorithm with distance parameter $R = 0.6$. The main contribution was thus to expand the studies to other available calibrations (GCW+JES, LC+JES) and to the $R = 0.4$. An example of such extension is presented in Figure 5.1 for the lowest and highest examined p_T^{avg} range and for all three calibrations. The general observation based on already existing studies of EM+JES calibration was confirmed for other calibrations and jets reconstructed by the anti- k_T algorithm with $R = 0.4$ as well: the response in data is reasonably well described by all MC simulations in the central region (within $\sim 2\%$ for $|\eta| < 2.8$) and still rather well in forward region (within $\sim 5\%$ for $|\eta| > 2.8$) in higher p_T^{avg} ranges. At lower p_T^{avg} in the forward region, however, the discrepancies between data and MC samples are around 10% up (HERWIG++ and ALPGEN) as well as down (PYTHIA6 and Perugia). These model differences are caused by different parton shower and hadronisation models between PYTHIA6/Perugia and HERWIG++/ALPGEN and are rather consistent in all jet calibrations studied in this analysis.

Since the MC predictions for relative jet response are systematically shifted away from data and the data lies right between these different predictions, an uncertainty on the relative jet response must be introduced. It is calculated as the RMS deviation of the MC models from the data and presented in Figure 5.2 for the central and the most forward η regions and both $R = 0.6$ and $R = 0.4$ anti- k_T jet reconstruction algorithms. The low p_T^{avg} and large η region gives the largest uncertainties (up to about 12%), which are dominated by physics modelling uncertainty, while the high p_T^{avg} region (spread of MC predictions small) is characterized by the true difference between the response in the data and MC.

5.4.2 Dijets in 2011 data

Data taking in 2011 was done at the same center-of-mass energy $\sqrt{s} = 7$ TeV, but with much larger instantaneous luminosities. The consequence is that such col-

lisions are characterized by larger pile-up³, which requires certain caution when drawing conclusions. The additional energy added to reconstructed jets from overlays of the main hard scale jet event with multiple pile-up interactions is by default subtracted. What however turned out to be a challenge from the η -intercalibration perspective were the event selection criteria, namely the cut on the third highest p_T jet.

Third jet cut optimization

The standard event selection introduced in Section 5.2 turned out to be insufficient for high pile-up events in 2011 data. The essential requirement on $2 \rightarrow 2$ dijet topology could no longer be ensured by the standard third jet cut, i.e. $p_T(j_3) < \max(0.15p_T^{\text{avg}}, 7\text{GeV})$. This is demonstrated in Figure 5.3. Figure 5.3(a) showing a distribution of the Jet Origin⁴ for the third jet demonstrates that about 20-30% of third jets are associated to other than the primary vertex (corresponding to the Jet Origin = 0), i.e. they come from pile-up interactions. Figure 5.3(b) shows the third jet p_T relative to p_T^{avg} and demonstrates that events with low p_T jets (i.e. collected especially by triggers EF_j10_a4_EFFS and EF_j15_a4_EFFS) contain third jets with significant relative transverse momentum.

There is a useful variable called Jet Vertex Fraction (JVF), which can be exploited to solve this issue. The JVF is calculated based on matching reconstructed tracks with reconstructed jets and it gives a percentage of the sum of transverse momenta of tracks that point back to the primary vertex (PV0) with respect to $\sum p_T$ of all tracks associated with the given jet. It is therefore a measure of how significant part of the jet can be directly attributed to the primary vertex: JVF is equal to 1 when all tracks come from the PV0, JVF=0 when none track can be matched to the PV0 (pile-up jets) and JVF=-1 for forward jets (tracking is limited to $|\eta| < 2.5$ region). Figure 5.4(a) presents a distribution of JVF for third jets and Figure 5.4(b) shows distribution of transverse momenta of third jets relative to p_T^{avg} . There is a clear separation between the inclusive spectrum and spectra with jet origin identified to be PV0 (JVF > 0.6 cut used) or jets from the forward region (JVF=-1). Therefore, the idea is to define a new third jet cut that is applied to the correct jet, i.e. a jet coming from the hard interaction, not a pile-up event. Two additional “third jet” definitions are therefore introduced: the third highest p_T jet selected only from jets that pass the JVF > 0.6 cut (denoted as “VtxConfJ3”, i.e. Vertex Confirmed third jet) and the third highest p_T jet selected only from jets that have JVF=-1 (denoted as “FwdJ3”, i.e. forward jets from the region $|\eta| > 2.5$). The new third jet cut has then two levels:

- VtxConfJ3 jet is required to have $p_T(j_3) < \max(0.25p_T^{\text{avg}}, 12\text{GeV})$
- FwdJ3 jet is required to have $p_T(j_3) < \max(0.20p_T^{\text{avg}}, 9\text{GeV})$

³Multiple proton-proton interactions within the same bunch crossing.

⁴Jet Origin is an integer number giving the position of the vertex in the vertex list from which a given jet originates. This is decided based on origin of tracks associated to the jet. Primary vertex has value 0, pile-up vertices have jet origin ≥ 1 and jets outside the Inner Detector acceptance ($|\eta| > 2.5$) have a value -1.

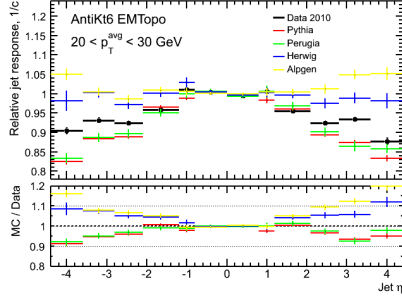
The effect of new third jet cut is demonstrated in Figure 5.5. There is a clear improvement in absolute value of relative jet response in the forward regions, especially for PYTHIA6 predictions. More importantly, the MC to data comparisons are notably improved. The new third jet cut is therefore a success and has been used as the default for processing 2011 data.

Relative jet response

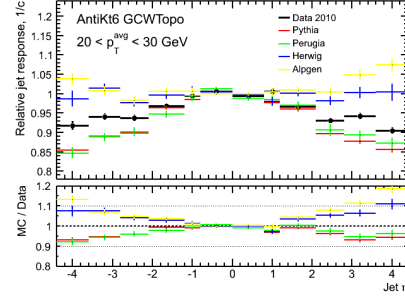
As in case of 2010 data, the η -intercalibration studies were performed for both $R = 0.6$ and $R = 0.4$ distance parameters of the anti- k_T jet reconstruction algorithm and for EM+JES and LC+JES calibrations. Comparisons of data to MC models (HERWIG++ and PYTHIA6) reveal similar behaviour as was already discussed for 2010 data. Jet responses between both jet algorithms are stable. Similar observation can be drawn for the difference between jet calibrations. An example of relative jet responses in 2011 data is presented in Figure 5.6 for three p_T^{avg} ranges. The response in data is well described by both MC models in the central region ($\sim 2\%$ in $|\eta| < 2.8$ range) and still reasonably well in the forward region ($\sim 5\%$ in $|\eta| > 2.8$ range) for higher values of p_T^{avg} . In the forward region and lower p_T^{avg} ranges, the MC to data ratios are found to be within $\sim 10\%$. Again, as in the 2010 data studies, we can observe the model differences due to different parton showers and hadronisation models, resulting in systematic overestimates of the data by HERWIG++ and underestimates by PYTHIA6.

5.4.3 Conclusions

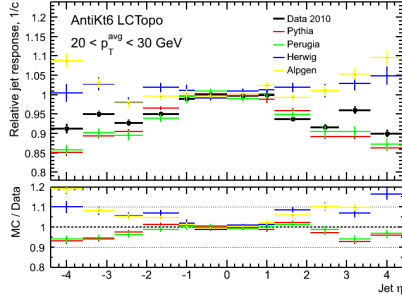
The analysis work on testing the Jet Energy Scale by balancing jet momenta in dijet events represented an important contribution to the ATLAS Collaboration. A new third jet cut, crucial for selecting a clean sample of dijet events usable for this analysis, had to be developed and it ensures that the cutting is done on real third jet (third highest p_T jet coming from the hard interaction) and not on the jet coming from a pile-up interaction. The η -intercalibration studies were performed on 2010 and 2011 data for two distance parameters of the anti- k_T jet reconstruction algorithm ($R = 0.6$ and $R = 0.4$) and for various jet energy calibration methods. These outputs provide a useful insight used in ATLAS analyses dealing with jets in 2010 and 2011 data.



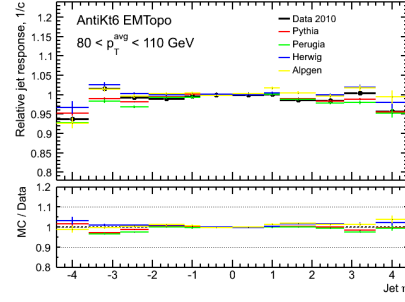
(a) EM+JES



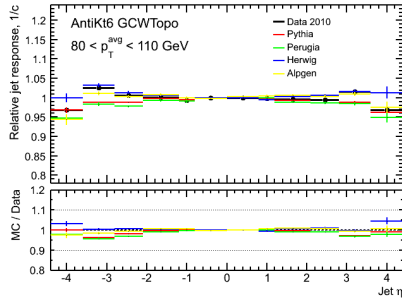
(b) GCW+JES



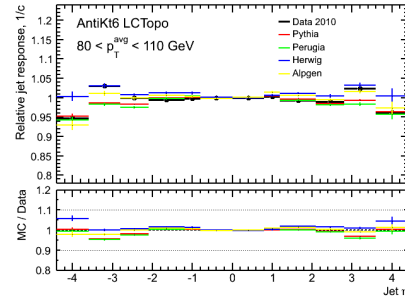
(c) LC+JES



(d) EM+JES



(e) GCW+JES



(f) LC+JES

Figure 5.1: Relative jet response as a function of the pseudorapidity of the probe jet in two different p_T^{avg} regions for EM+JES, GCW+JES and LC+JES jet calibrations. 2010 data (periods A to I) compared to various Monte Carlo models.

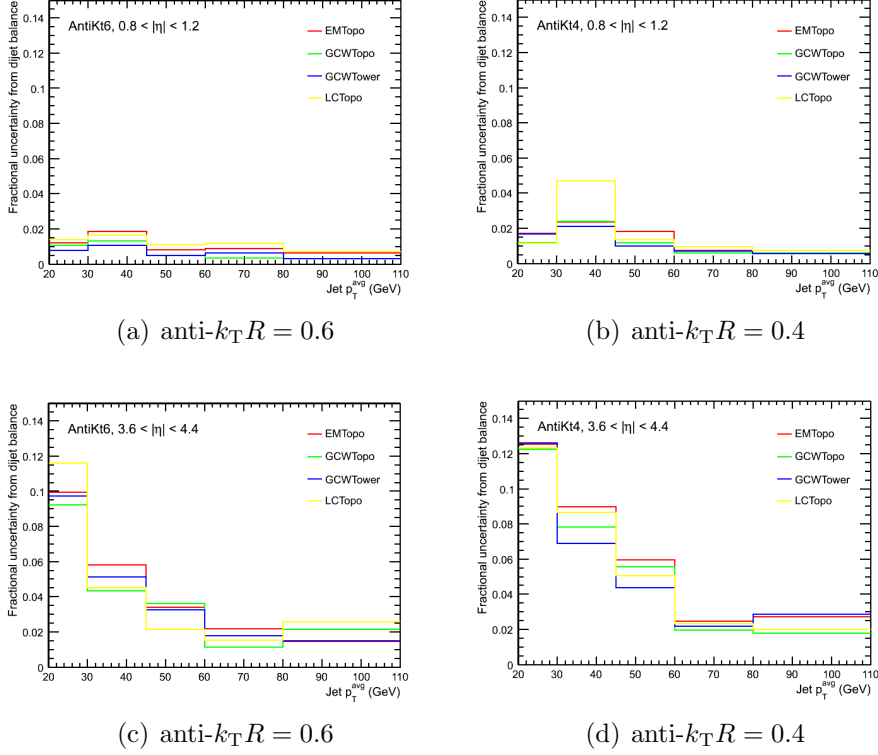


Figure 5.2: Uncertainty in the jet response as a function of the p_T^{avg} in two different pseudorapidity regions for all studied jet calibrations: EM+JES, GCW+JES and LC+JES. Jets reconstructed by the anti- k_T algorithm with radii $R = 0.6$ and $R = 0.4$.

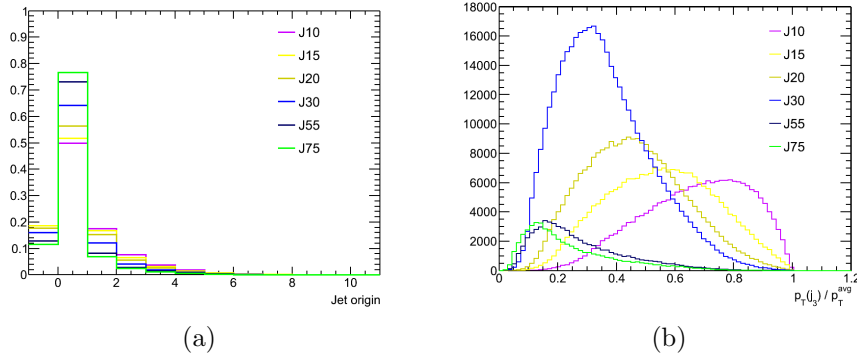


Figure 5.3: Event distributions (no scaling applied, 2011 data) for jet vertex fraction of the third jet (left) and the third jet transverse momentum relative to p_T^{avg} . Events are separated based on the trigger that fired in the given event. Standard selection cuts applied ($p_T^{\text{avg}} > 20$ GeV, $\Delta\phi(j_1, j_2) > 2.6$). Jets reconstructed by the anti- k_T algorithm with radius $R = 0.6$.

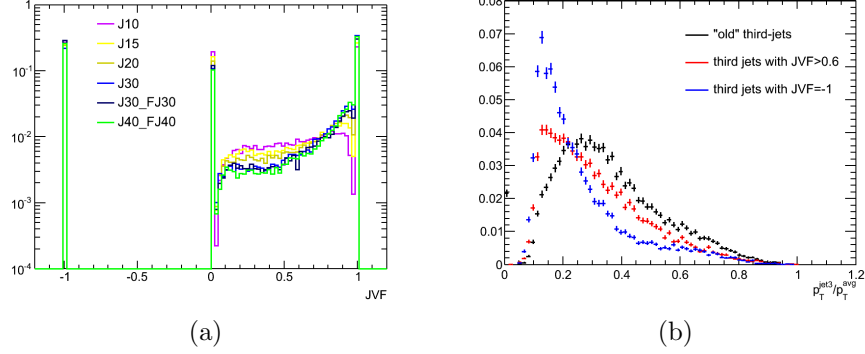


Figure 5.4: Distributions of Jet Vertex Fraction of third jets for events (2011 data) collected by various jet triggers (left) and of the transverse momentum of third jets relative to p_T^{avg} for EF_j30_a4_EFFS jet trigger (right). In Figure b), different third jet cuts are examined ("old" refers to the $p_T^{j3} < 0.15 p_T^{avg}$ cut). Distributions are normalized to unity. Jets reconstructed by the anti- k_T algorithm with radius $R = 0.6$.

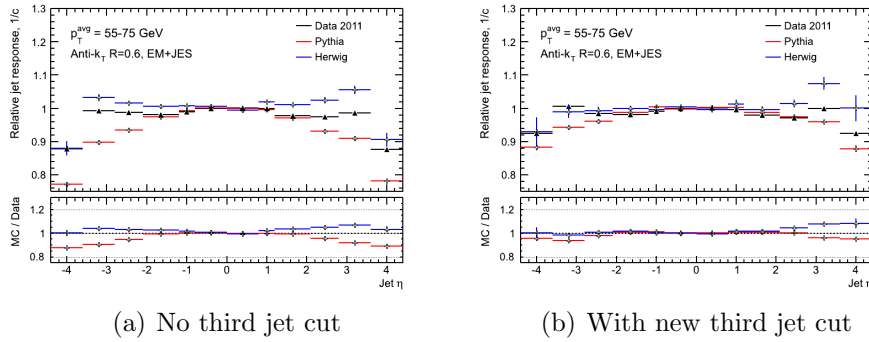


Figure 5.5: Relative jet response as a function of the pseudorapidity in period D of 2011 data without using third jet cut (left) and with new third jet cut (right).

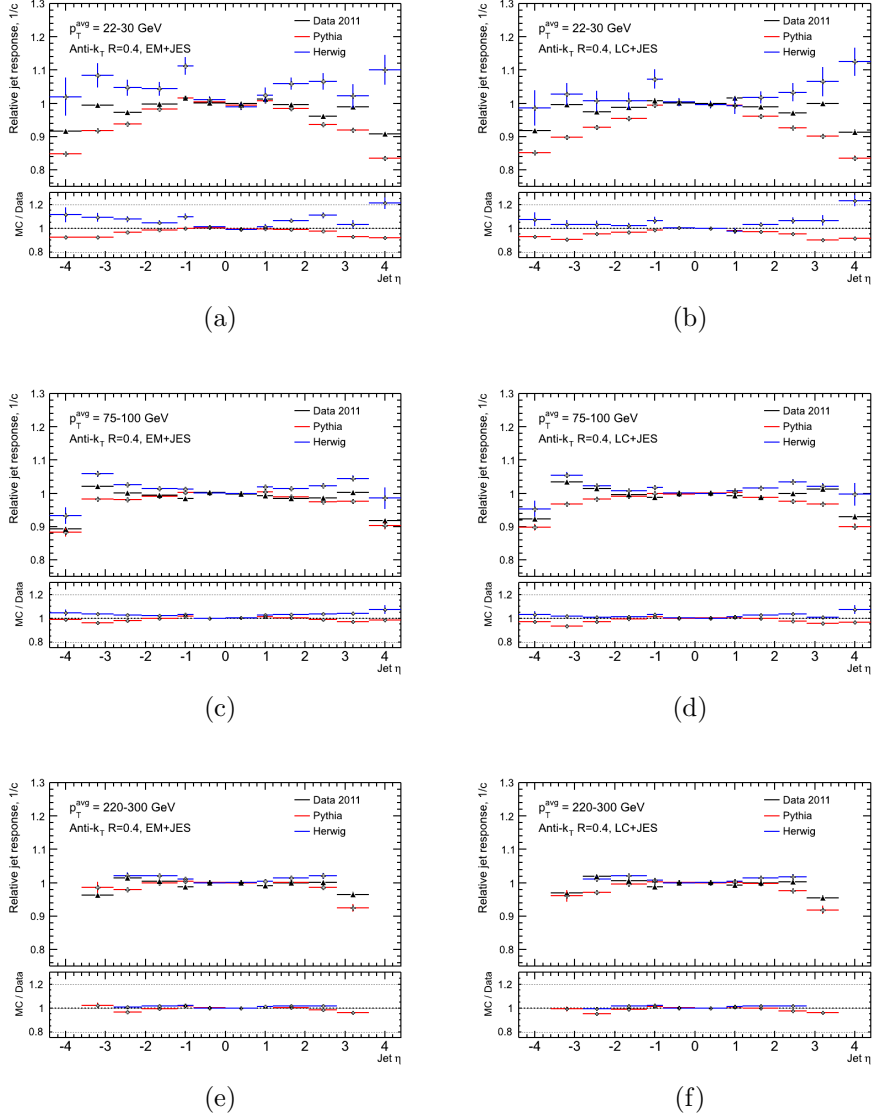


Figure 5.6: Relative jet response as a function of the pseudorapidity of the probe jet in three different p_T^{avg} regions for EM+JES and LC+JES jet calibrations. 2011 data (periods D to I) compared to HERWIG++ and PYTHIA6 models.

6. The event selection

The ATLAS Collaboration has already published two measurements which are relevant to the diffractive dijet analysis presented in this thesis:

- 2010 inclusive dijet measurement [44]
- Soft rapidity gaps analysis [45]

Both of these works will be referred to throughout this and next chapters. Though they provide a solid basis to start from, they are in their basic state for many reasons insufficient and need to be significantly adapted.

6.1 Data samples

The organization of the data acquired by the ATLAS experiment can be thought of as a structure of several levels. First, the data is classified according to the year it was taken in. Each year is divided into several so-called “Periods”, each of them gathering data with similar LHC beam conditions and physics goals. A period further comprises of so-called “Runs” characterised by a six-digit number, which are finally divided into “lumi-blocks” (LB) - short data taking time stamps of a duration in the order of tens of seconds to minutes.

In order to observe a hard diffractive dijet event with a large rapidity gap, a non pile-up environment (i.e. not more than one interaction per bunch crossing) is crucial. If the hard SD event is overlayed with another interaction, mostly a minimum-bias pp collision, the rapidity gap is partly or completely filled with particles from this additional inclusive interaction. Since only early LHC running conditions (with some rare exceptions) were favorable to this fundamental requirement specific for our diffractive analysis, the data sample selection is limited to early 2010 data at $\sqrt{s} = 7$ TeV, particularly periods A and B.

The Period A 2010, in which the LHC was being filled with unsqueezed bunches (a typical beam spot width of 50-60 μm in x and y), could have a large diffractive potential as the pile-up was negligible. However, given the low integrated luminosity collected in that period, the number of events with a hard scatter producing two high p_T jets and having large rapidity gap is small. Period B, by contrast, is more promising. Beams circulating the LHC were squeezed (a typical beam spot width of 30-40 μm), but the pile-up was still low enough, as can be read from Table 6.1 from the column denoted as “Peak $\langle\mu\rangle$ ” (μ is an average number of interactions per bunch crossing).

Data selected by trigger menus are sorted out into several different streams. The physics streams are L1Calo (events selected mostly by jet, e/γ , τ and sum E_T triggers) and MinBias (triggered mostly by MBTS counters and forward detectors). Overlays of events between these two streams are possible and have to be removed from the analysis.

A basic selection of runs usable for a physics analysis is done via so-called Good Runs List (GRL). To each run, a list of LBs which can be safely used (all important sub-detectors on high performance) is provided. In this analysis, the same GRL as in the 2010 dijet measurement was used. It is based on recommendations of the Jet/ E_T performance group, requiring green Data Quality flags for all important sub-systems, such as calorimeters and tracking detectors. After this selection, five runs of period B are available for this analysis. Their basic characteristics are summarized in table 6.1.

Run Num.	Peak $\langle\mu\rangle$	N_{bunch}	Δt_{bunch} (ns)	L_{stable} (μb^{-1})	$L_{\text{after GRL}}$ (μb^{-1})
153565	0.044	2	44625	754.7	715.2
155073	0.108	2	66825	1195	1120.7
155112	0.144	3	5000	3691	3279.6
155116	0.114	3	5000	564.5	453.6
155160	0.123	3	5000	1361	1263.3

Table 6.1: Run conditions for the selected runs (those used for the analysis) in 2010 Period B. Number of bunches per train (N_{bunch}), time distance between two neighbouring bunches (Δt_{bunch}), integrated luminosity of stable beams (L_{stable}) and after Good Runs List selection ($L_{\text{after GRL}}$) are presented.

6.2 Trigger selection

Since the analysis presented in this document starts from a basic inclusive dijet sample of events, jet trigger selection is naturally assumed to be the most appropriate choice. Even though other possibilities were also explored, the jet triggers eventually turned out to be the best available option.

Before settling down with the option that is eventually used for this analysis, a number of approaches have been investigated. The author does not feel it necessary to go into details of all these (semi-) dead ends, but a few notes (spread throughout this section) demonstrating some of the difficulties of the diffractive dijet analysis are in order.

6.2.1 Jet and minimum bias triggers

The most commonly used triggers in analyses dealing with jets are so-called jet triggers (central and forward) and a Minimum Bias Trigger Scintillator (MBTS). The MBTS trigger called L1_MBTS_1 requires at least one hit in minimum bias scintillators (see Section 2.3.4) covering $2.09 < |\eta| < 3.84$. It is the primary trigger used to select inclusive minimum-bias events and is found to have a negligible inefficiency for events with jets with a transverse momentum between 20-60 GeV [44]. Jet triggers, both central and forward ones, select collision events based on a presence of a jet with sufficient E_T at the electromagnetic (EM) scale¹. Level-1

¹The electromagnetic scale is the basic calorimeter signal scale for the ATLAS calorimeters. It is based on test-beam measurements of a response for the energy deposited in electromagnetic

thresholds for central triggers such as L1_J5, L1_J10, L1_J15 are 5, 10 and 15 GeV, respectively, and for forward triggers such as L1_FJ10, L1_FJ30, etc. are 10 and 30 GeV, respectively.

6.2.2 Trigger prescales

The ATLAS triggers represent a key tool for deciding whether a particular event will be recorded or not (see Section 2.5). To enhance (suppress) certain types of collision events, trigger prescales (PS) have been introduced. If the prescale is set to $PS_t = n$, it means that only in every n -th event a decision of the trigger t is considered for final *yes* or *no*. It is therefore obvious that the PS can be one of the key parameters to consider when preparing a trigger-selection strategy for a physics analysis.

Figures 6.1 and 6.2 present an overview of prescales of Level-1 triggers (EF respectively) across 2010 pp -collision periods. Up to the period F, Level-1 triggers were used to collect data. Since period G, HLT triggers were fully commissioned. Some of the HLT triggers were on before period G already, but they were in the so-called “pass-through” mode (they were not used for collecting data).

Given the pile-up conditions in later periods, this analysis is built upon early 2010 data. That also simplifies the trigger selection as in period A and B, no jet trigger was prescaled. In period C, a small average prescale $PS \sim 1.1$ is there for the lowest- p_T threshold jet trigger L1_J5. In period D and above, prescales of events with low- p_T jets are growing significantly. The L1_MBTS_1 trigger is not prescaled in period A, has an average PS ~ 50 in B and grows to around 500 in C. Since then, the prescale is so high that only negligible amount of the data collected is due to this trigger.

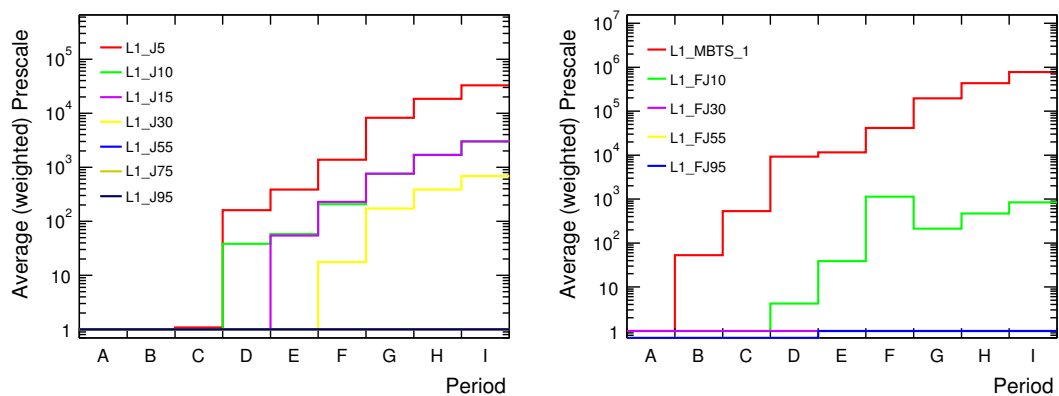


Figure 6.1: Prescales of central (left) and forward (right) Level-1 triggers in 2010 periods of the ATLAS data-taking. Prescales are calculated as weighted average (according to the luminosity) across LBs in a given period.

showers by electrons and muons with known energy (from the so-called “test-beam”). No correction for hadron response is applied.

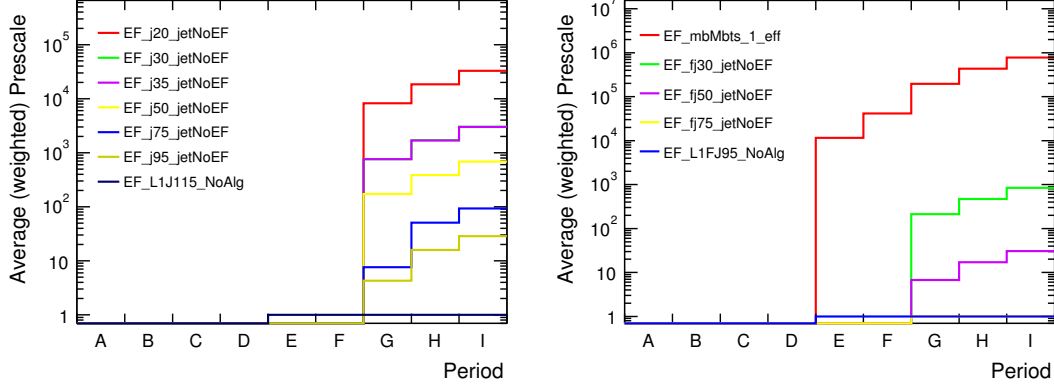


Figure 6.2: Prescales of central (left) and forward (right) EF-level triggers in 2010 periods of the ATLAS data-taking. Prescales are calculated as weighted average (according to the luminosity) accross LBs in a given period.

6.2.3 Luminosity and cross section

The ATLAS luminosity calculation tool (*iLumiCalc*) provides a way to access detailed information on triggers (such as trigger prescales) and luminosities in given runs. To get the information relevant for the particular analysis, the GRL is supplied as an input along with a luminosity tag specifying the actual database with records of collected luminosities (*OfLumi-7TeV-004*). The “L1-live fraction trigger” (L1_MBTs.2) also needs to be specified as it is used to determine a fraction of luminosity that ATLAS could record (after correcting for effects as dead-time etc.).

The usual way of calculating the total integrated luminosity of a given data period is by summing over LBs passing a particular GRL in all involved runs. Such luminosity can then be used to get the measured cross section according to the usual formula

$$\sigma = \frac{N_{\text{events}}}{L}, \quad (6.1)$$

where L is the integrated luminosity of a given dataset and N is the number of events collected.

The effective luminosity in case of events collected by a trigger with prescale, which can vary significantly throughout the run, can be calculated as

$$L_J = \sum_{\text{LB}} \frac{L_{\text{LB}}}{P_{\text{LB}}^J}, \quad (6.2)$$

where L_{LB} is the luminosity of the given LB and P_{LB}^J is the prescale of trigger J in the given LB. This equation yields, in case of period B, $L_{\text{L1J5}} = 6.753 \text{ nb}^{-1}$ and $L_{\text{L1MBTs.1}} = 0.303 \text{ nb}^{-1}$. As the prescale of L1_J5 is 1, the L_{L1J5} is equal to the total luminosity of period B.

It is not unusual, as we shall see later on, that a trigger strategy is more complicated than requiring just a single trigger. It can be convenient to combine,

for example, central and forward jet triggers into a logical OR. In this case, the luminosity can be calculated, as shown in [44], as

$$L_{A \text{ OR } B} = \sum_{LB} \frac{L_{LB}}{P_{LB}^A P_{LB}^B / (P_{LB}^A + P_{LB}^B - 1)} \quad (6.3)$$

This equation comes from a simple consideration of two overlaying sets, A and B. The probability of their logical OR is $P(A||B) = P(A) + P(B) - P(A \cap B)$, where the last item being subtracted from the rest is due to removing events that are double-counted due to the overlay of the two sets. In terms of trigger luminosities, this can be rewritten as $L(A||B) = \frac{L}{P_A} + \frac{L}{P_B} - \frac{L}{P_A P_B}$. The equation 6.3 can be retrieved by a simple mathematical modification.

For triggers $A = \text{L1_J5}$ and $B = \text{L1_MBTS_1}$, the effective luminosity is found to be $L_{A \text{ OR } B} = 0.303 \text{ nb}^{-1}$.

The final cross section can be calculated as

$$\sigma = \frac{N_{J5}}{L_{J5}} + \frac{N_{MBTS}}{L_{MBTS}} + \frac{N_{J5 \text{ OR } MBTS}}{L_{J5 \text{ OR } MBTS}} \quad (6.4)$$

which makes sure that events are properly treated by separating them to three separate categories. Here $N_{\text{L1_J5}}$, $N_{\text{L1_MBTS_1}}$ and $N_{\text{L1_J5ORL1_MBTS_1}}$ denote the number of events for which the central, MBTS and both triggers are required (based on p_T and η of both leading and sub-leading jets).

6.2.4 Inclusive 2010 dijet analysis

The measurement of the dijet invariant mass m_{12} [44] performed on full 2010 data sample became eventually a baseline for the diffractive dijet analysis presented in this thesis. The basic selection is done by requiring a presence of two high- p_T jets (the two jets with the highest transverse momentum are required to have $p_T^{\text{jet 1 (jet 2)}} > 30$ (20) GeV) well contained within the calorimeter system ($|\eta^{\text{jet 1 (jet 2)}}| < 4.4$) present in a collision event with good primary vertex (having at least five associated tracks). The trigger strategy was designed in such a way that it optimizes the usage of the available (and limited) statistics for low invariant masses by creating a *per-jet* trigger scheme. In this approach, two triggers are attributed to each event based on the p_T and η range of the two highest- p_T jets (so-called “leading” and “sub-leading” jet) with a requirement that triggers are used in the region where they are at least 99% efficient (so-called “trigger plateau”). Events collected by different trigger combinations must be stored to separate histograms which are, before final merging, normalized to the cross section based on trigger luminosities as calculated by equations 6.2 and 6.3. This approach, though more complicated, allows to exploit the available statistics in a better way than the standard inclusive “per-event” strategy (see [44]) as it optimizes the use of less prescaled higher p_T -threshold jet triggers at lower p_T (while still being on trigger plateau). There is also a number of trigger inefficiency corrections (such as for the “crack” region $1.3 < |\eta| < 1.6$, dead FCal towers in certain η -regions, etc.) that need to be applied as a weight to the whole

collision event.

The goal of the 2010 dijet analysis was to measure the dijet invariant mass spectrum in the widest possible range, that is with a focus on low masses as well. It was done in several y^* bins, where $y^* = |y_1 - y_2|/2$ ($y_{1,2}$ is a rapidity of the leading or sub-leading jet) with the selection cuts and trigger scheme briefly outlined above. As an important cross-check, this whole complex measurement was reproduced with hopes that it will become a cornerstone of the diffractive dijet analysis where large rapidity gaps (small invariant masses, see equations 1.16 and 1.15) are in the center of our interest. Therefore, the dijet analysis was run across full ATLAS 2010 data sample (periods A to I) and the detector level invariant mass spectrum was then compared to the one provided to us by the original ATLAS inclusive dijet group². This comparison is presented in Figure 6.3 (a per-period cut-flow table is included in Appendix A) and clearly demonstrates that the official dijet trigger strategy was understood and implemented well.

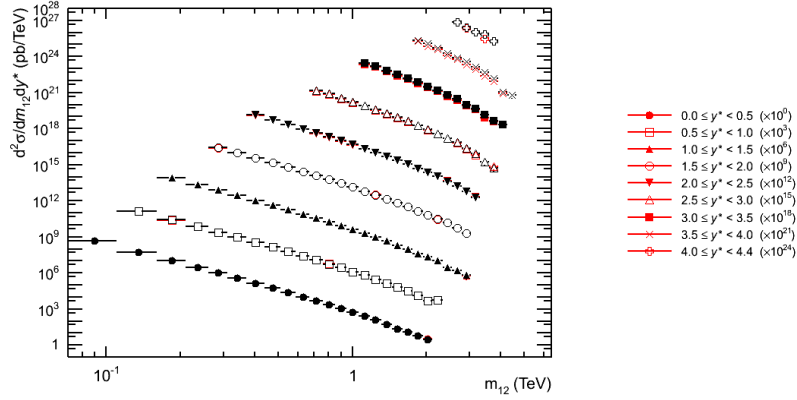


Figure 6.3: Detector level dijet invariant mass cross section in several different $y^* = |y_1 - y_2|/2$ ranges as measured by the inclusive dijet group (red) and as reproduced (black).

6.2.5 Trigger scheme optimization

Unfortunately, the performance of per-jet triggers (as developed by the inclusive dijet group) at large rapidity gaps is not high enough to allow for a statistically significant measurement, as can be deduced from the cut-flow table in Appendix A (while keeping in mind that only early 2010 data periods can be used due to significant pile-up later on). That does not mean, however, that the events are not present in the data sample being examined, as can be seen from the Figure 6.4 (period B) where the no-trigger-selection option is also explored. The quantitative summary of these findings is in the Table 6.2. The trigger strategy has to be, therefore, modified to be able to select a diffractive enhanced event sample with low p_T jets.

As a starting point, even before implementing the inclusive dijet trigger scheme, the trigger strategy used for the dijet performance work (see Chapter 5) was

²Many thanks to Christopher Meyer.

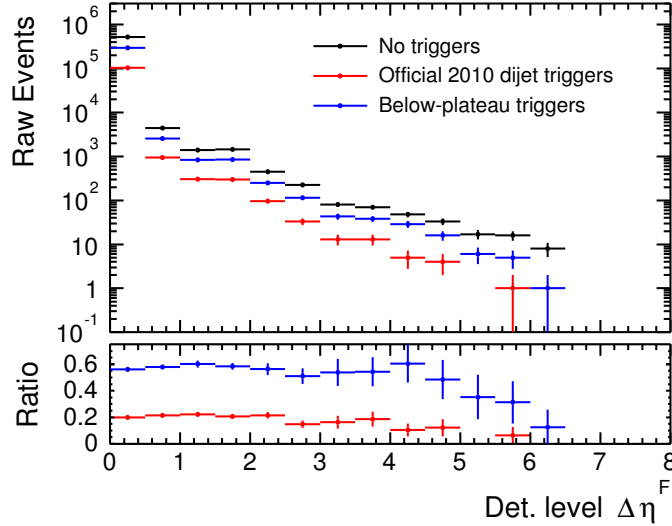


Figure 6.4: Rapidity gap spectrum for different trigger strategies for period B. Event selection cuts: $p_T^{\text{jet } 1 (\text{jet } 2)} > 30 \text{ (20) GeV}$, $n_{\text{vertices}}(2\text{trk}) = 1$.

examined in its original as well as modified form. The modification lies in a realization that it should not be necessary to keep insisting on collecting events on the trigger efficiency plateau only - if appropriate correction factors in the form of event weights are applied. This option was explored by lowering the minimal p_T^{avg} cut for L1_J5 trigger from 45 GeV to 30 GeV, bypassing thus the highly prescaled MBTS trigger for events with jet transverse momenta in the range 30-45 GeV. Though it led to a significant increase of statistics compared to the original p_T ranges, this trigger selection was, after a number of validation efforts (trigger inefficiencies were taken into account by measuring the trigger efficiency curves as a function of p_T^{avg} and fitting their turn-on parts), abandoned as unsuitable for a physics analysis. This conclusion was mainly based on validation attempts against the official inclusive dijet strategy for m_{12} , p_T^{jet} and η^{jet} spectra.

The same outcome eventually came from attempts to investigate a possibility of using non-jet triggers, as studies with going significantly below jet trigger efficiency plateaux showed that there is still very large amount of events fired by “something else”. Figure 6.5 summarizes the event yields of the most important triggers gathering events with rapidity gaps bigger than three units of pseudorapidity. Significant number of events are gathered by tau-jet (TAU), electromagnetic (EM) or missing E_T triggers, none of which are appropriate for the diffractive dijet analysis, as more detailed studies showed.

It was eventually decided, after these trigger studies (plus some other simpler checks like logical OR of all jet triggers), to use the inclusive dijet trigger strategy with a modification allowing to use jet triggers below the efficiency plateaux.

6.2.6 Trigger efficiency measurement

The usability of a trigger selecting events in the region where it is not at least 99% efficient relies on an assumption that the inefficiency can be well described. The jet-trigger performance depends not only on the transverse momentum of

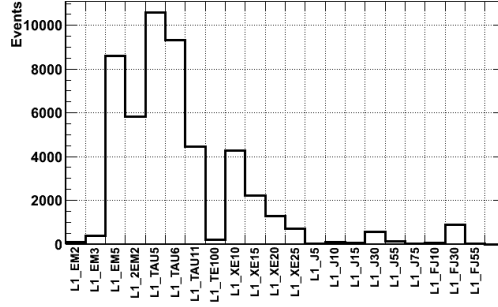


Figure 6.5: Overview of the most important triggers (in period F) that fired events with rapidity gaps of the size $\Delta\eta^F > 3$. “EM” stands for triggers based on energy deposition in electromagnetic calorimeter, “TAU” are based on identification of tau-jets, “TE” evaluate total transverse energy and “XE” are triggers based upon missing energy.

Trigger scheme	Events with $\Delta\eta^F > 3$
No triggers	272
Official 2010 dijet triggers	36
Below-plateau triggers	138

Table 6.2: Event yields (period B) after applying different trigger strategies for the standard cuts of the inclusive 2010 dijet analysis (with the pile-up suppression cut). Jets were reconstructed by the anti- k_T $R = 0.6$ algorithm.

the jet in question, but also on its η . If we are interested in measuring the trigger efficiency as a function of a transverse momentum, it is advisable to separate this measurement into several η -ranges and vice versa. The default η -ranges used in inclusive dijet analysis are $|\eta| < 0.3$, $0.3 < |\eta| < 1.2$, $1.2 < |\eta| < 2.1$, $2.1 < |\eta| < 2.8$, $2.8 < |\eta| < 3.6$ and $3.6 < |\eta| < 4.4$.

The measurement of trigger efficiencies was done by a so-called “bootstrap” method. The basic event sample is selected with a trigger which is fully efficient in the full p_T - η region of the trigger under investigation, so for example the L1_MBTS_1 trigger in the MinBias stream. From this selection, a sub-set of events in which the tested trigger fired is chosen. For being able to distinguish which jet actually fired the given trigger, a cut $\Delta R = \sqrt{\Delta\eta^2 + \Delta\phi^2} < 0.5$ between the physical jet and the jet RoI (Region of Interest; a jet candidate that fired the given trigger, reconstructed on-line by a simplified procedure during the trigger evaluation time - not to be mismatched with fully reconstructed jets used in a physics analysis) is required.

The trigger efficiency curves (as a function of p_T) have two distinctive regions: the turn-on part (steeply falling with decreasing jet p_T) and the plateau (region with no p_T -dependence). The turn-on parts can be fitted with a function

$$\epsilon_{\text{trig}}(p_T) = a_0 \cdot f_{\text{Err}} \left(\frac{p_T - a_1}{a_2} + 1 \right) \quad (6.5)$$

where a_i are the fit parameters, f_{Err} is the error function and p_T is the transverse momentum of the jet that fired given trigger.

An example of such trigger efficiency measurement is presented in Figure 6.6, where the comparison among periods B, D and F is plotted for a selected central and forward jet trigger. The forward jet comparison reveals a significant shift of period B trigger efficiency curve versus period D or F respectively. This can be also a manifestation of the fact that in early 2010 periods (A to D), the forward jet triggers were not fully commissioned yet and therefore should not be used for physics analysis.

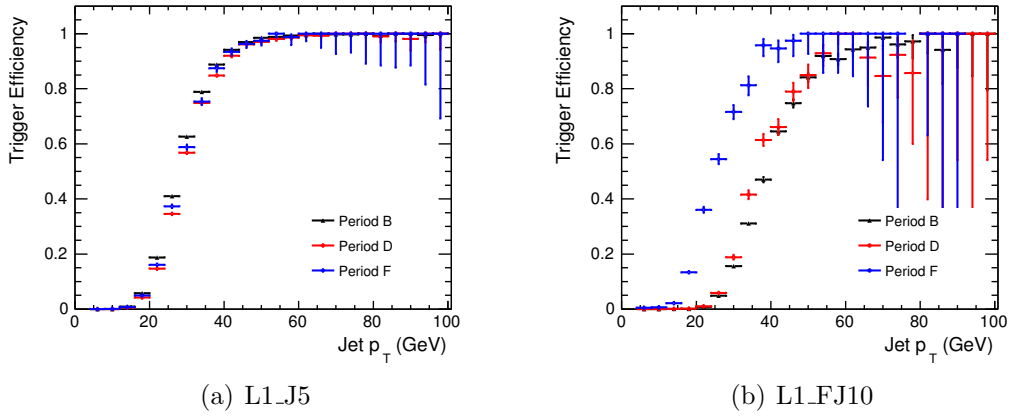


Figure 6.6: Comparisons of trigger efficiency curves between 2010 data periods. The central L1_J5 trigger (left) measured in the eta region $|\eta| < 2.8$, the forward L1_FJ10 trigger in $3.3 < |\eta| < 4.4$.

6.2.7 New trigger selection in period F

The period F was chosen as a starting point of attempts to optimize the trigger strategy due to its highest statistics in the region of interest (rapidity gaps of the size larger than three units of pseudorapidity, see table A.1) and still relatively simple trigger selection based on Level-1 triggers only (L2 chains were used from period G onwards).

The inclusive dijet analysis used a combination of four central jet triggers (L1_J5, L1_J15, L1_J30, L1_J55) within $|\eta| < 3.1$, two forward jet triggers (L1_FJ10, L1_FJ30) within $3.1 < |\eta| < 4.4$ and L1_MBTS.1 trigger for lowest p_T jets in full $|\eta| < 4.4$ range. As discussed above, a possible way how to boost statistics of events with low- p_T jets is to use higher- p_T threshold triggers (which are significantly less prescaled, see Figures 6.1 and 6.1) at lower p_T ranges. The question is how much below the trigger efficiency plateau is it possible to go. Several practical experiments with different thresholds ($\epsilon > 85\%$, $\epsilon > 70\%$, $\epsilon > 60\%$, $\epsilon > 50\%$) led to the conclusion that 70% is a reasonable compromise between getting the

highest possible event statistics and staying in the “safe” region (where the efficiency measurement is not significantly biased by trigger uncertainties and other technical aspects of trigger implementation in the ATLAS Data Acquisition system).

The 70% efficiency threshold was found out in such a way that in no η -region studied, the efficiency gets below 70%. Efficiencies were measured and fitted by the function 6.5 in four η -ranges ($|\eta| < 0.3$, $0.3 < |\eta| < 1.2$, $1.2 < |\eta| < 2.1$, $2.1 < |\eta| < 2.8$) for all five central triggers and in two forward η -ranges ($2.8 < |\eta| < 3.6$ and $3.6 < |\eta| < 4.4$) for both FJ triggers. Each of these 24 fits were incorporated into the analysis to provide per-event scaling factors to correct for the trigger inefficiencies. In case that both jets fired their jet trigger and are located in the region below the trigger efficiency plateau, the scaling factor is calculated as $1/\epsilon_1 + 1/\epsilon_2 - 1/(\epsilon_1\epsilon_2)$ (it comes from consideration that two partly-overlaying sets are merged as logical OR, hence the subtraction of the factor $1/(\epsilon_1\epsilon_2)$: $A \cup B = A + B - A \cap B$). An example of the trigger efficiency dependence in different η -regions is demonstrated in Figure 6.7.

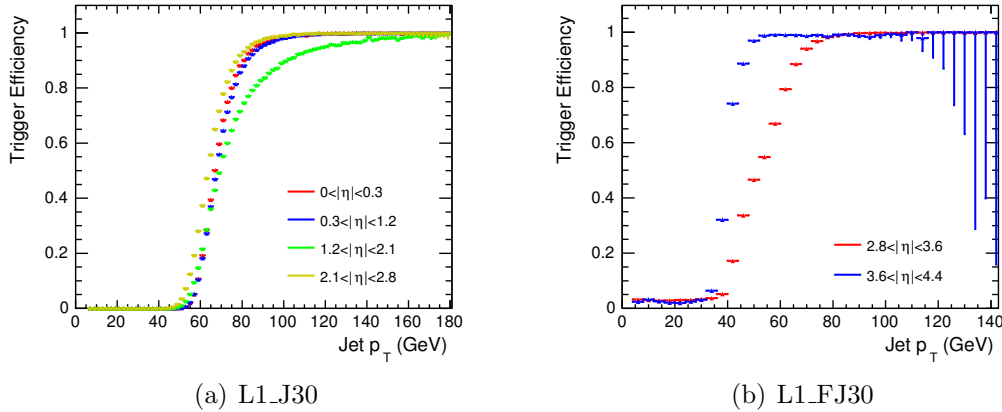


Figure 6.7: Trigger efficiency curves of the central L1_J30 (left) and the forward L1_FJ30 trigger in different η -ranges in 2010 data period F.

The optimized (below-plateau) trigger strategy used for period F data is summarized in tables 6.3 and 6.4. The central (forward) region is defined as area of the ATLAS calorimeter where the central (forward) jet triggers are fully efficient. The HEC-FCal transition region ($2.9 < |\eta| < 3.3$) is specific for any jet analysis as the trigger efficiency of the central jet triggers is steeply falling as a function of η , while forward triggers are not fully efficient yet. It was however shown [44] (and confirmed by our efficiency measurements) that efficiencies of logical OR of central and forward triggers (e.g. L1_J10 OR L1_FJ10) are 100% efficient even in this region. Therefore, when a jet is within $2.9 < |\eta| < 3.3$, a logical OR between triggers from table 6.3 and 6.4 is done. To decide which trigger was actually fired by this particular jet, $\Delta R = \sqrt{\Delta\eta^2 + \Delta\phi^2}$ between the reconstructed jet and L1 jet RoI (of given central and forward trigger) is calculated and required to be within $\Delta R < 0.5$ (to avoid fake matches).

Jet p_T (GeV)	$ \eta^{\text{jet}} < 2.9$
20 – 34	L1_MBTS_1
34 – 42	L1_J5
42 – 50	L1_J10
50 – 78	L1_J15
78 – 122	L1_J30
> 122	L1_J55

Table 6.3: The trigger selection in the central region developed for diffractive dijet analysis with 2010 period F data sample.

Jet p_T (GeV)	$3.3 < \eta^{\text{jet}} < 4.4$
20 – 26.5	L1_MBTS_1
26.5 – 48	L1_FJ10
48 – 100	L1_FJ30
> 100	L1_FJ55

Table 6.4: The trigger selection in the forward region developed for diffractive dijet analysis with 2010 period F data sample.

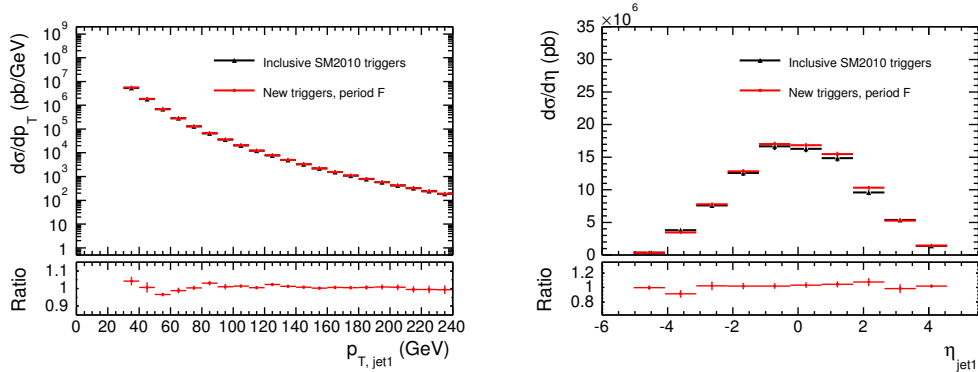


Figure 6.8: Detector level p_T (left) and η (right) comparisons between the official inclusive 2010 dijet trigger strategy (black) and the new below-plateaux triggers (red) for period F.

As shown above for invariant mass comparisons, an implementation of the official 2010 dijet trigger scheme was successful. Another reference distributions, such as jet p_T and η , can thus be prepared. From now on, new trigger strategies can be validated not only to the m_{12} spectra, but to p_T and η as well. Such validation plots are shown in Figure 6.8. It is clear that a very good agreement was achieved, mostly within 5% (with the exception of two η bins where it goes up to 8%). Given the very steep turn-on parts of trigger efficiency curves, this is an excellent result. Moreover, using jet triggers down to 70% of their efficiencies gained us about three times more events with large gaps above three units of rapidity in size.

Though the period F is promising with respect to the available statistics, there are two set-backs. First one is going to be discussed in Chapter 7 as it relates to the noise removal for the rapidity gap definition - there is a need for new D3PD

production (making available an additional cluster moment called “significance”), but since this is the old data, the ESD files (necessary for new D3PD production) are no longer available on the Grid. Second, there is a worry of a significant pile-up contribution ($\langle \mu \rangle = 2$), namely the in-time and out-of-time pile-up, as will be discussed in Chapter 11. It was therefore decided to base the diffractive dijet analysis on the period B only.

6.2.8 New trigger selection in period B

As mentioned in the previous paragraph, the period B is the default data sample used for this physics analysis. The trigger selection was tuned in a similar way as for period F, but this time it is much simpler: no jet trigger is prescaled (we can thus use the L1_J5 for full p_T range) and the forward jet triggers were not commissioned yet. Therefore, for the low- p_T and forward jets, L1_MBTS_1 trigger is used (in accordance with the inclusive dijet trigger selection).

In addition to selecting events by triggers with efficiency below 100%, the η -ranges were adapted based on Figure 6.9(a), where the L1_J5 trigger efficiency measurement as a function of η^{jet} in the region of interest (below plateau) is demonstrated. The measurement of central jets is split into five different sub-regions ($|\eta| < 0.8$, $0.8 < |\eta| < 1.3$, $1.3 < |\eta| < 1.7$, $1.7 < |\eta| < 2.4$, $2.4 < |\eta| < 2.9$; for efficiencies, see Figure 6.9(b)), each of which is fitted by the error function presented in equation 6.5 (for results, see Figure 6.10). The thresholds for using L1_J5 trigger were set to $p_T = 34$ GeV (anti- k_T $R = 0.6$ jets) and $p_T = 29$ GeV (anti- k_T $R = 0.4$ jets). This corresponds to efficiencies $> 60\%$ in the $1.3 < |\eta| < 1.7$ region and $> 75\%$ in other regions.

Figure 6.9(a) also reveals a problematic “crack” region $1.3 < |\eta| < 1.6$ (transition between calorimeter barrel and end-caps), where the jet triggers never become fully efficient due to inhomogeneities. This effect is corrected for in the analysis by constant scaling factor 0.89 for $p_T < 78$ GeV and 1.0 for larger p_T (based on [44], confirmed by our efficiency measurement).

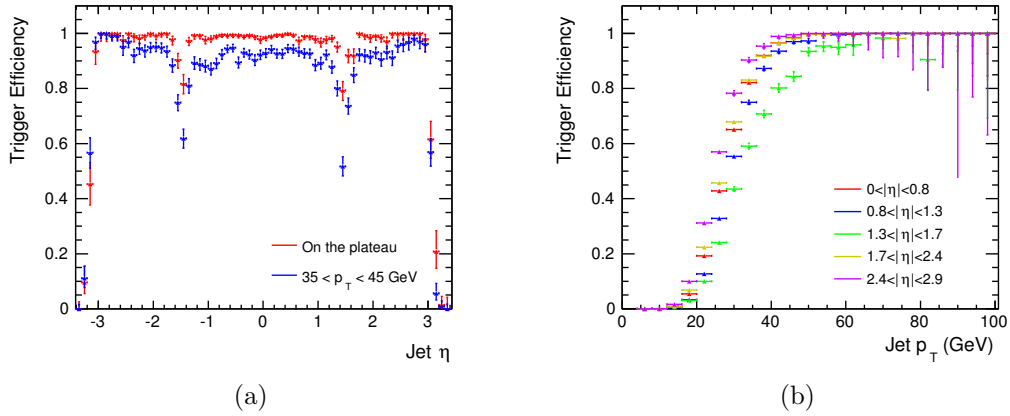


Figure 6.9: Trigger efficiencies as a function of (a) η and (b) p_T for anti- k_T $R = 0.6$ jets.

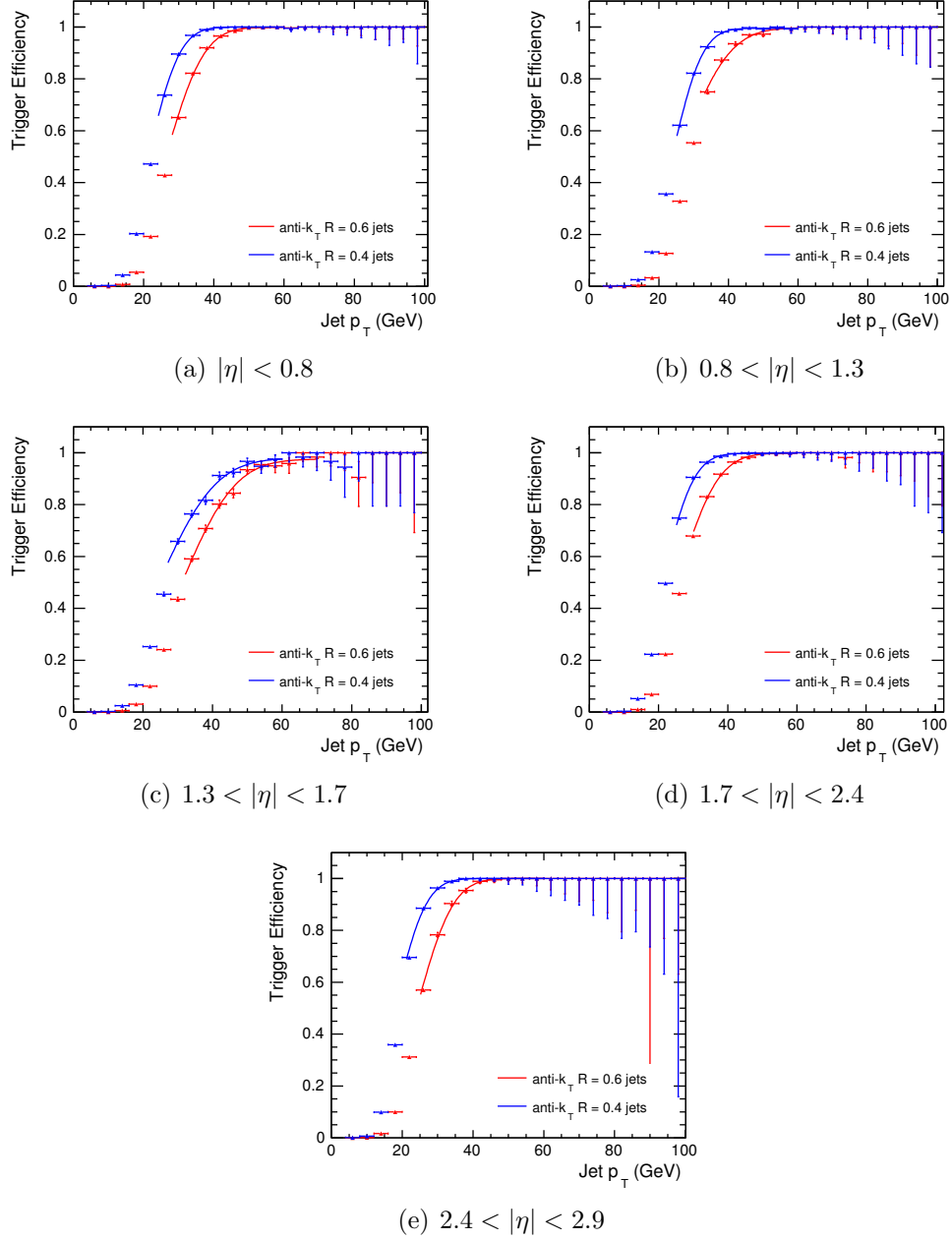


Figure 6.10: L1_J5 efficiencies in data as a function of the jet p_T for anti- k_T jets with $R = 0.4$ and $R = 0.6$ for different η -regions.

The practical implementation is the same as for period F or the inclusive dijet selection: for a particular event, a logical OR of two triggers (one corresponding to the leading and the latter one to the sub-leading jet) is requested. The event can thus be classified into three distinctive categories depending on the required combination of triggers: L1_J5 only (events normalized by $L_{\text{L1_J5}} = 6.753 \text{ nb}^{-1}$), L1_MBTS_1 only (events normalized by $L_{\text{L1_MBTS_1}} = 0.303 \text{ nb}^{-1}$) and logical OR of both ($L_{\text{OR}} = 0.303 \text{ nb}^{-1}$, see equation 6.3).

Just as in case of the period F, the adapted inclusive dijet trigger strategy is a success, as was shown already in Figure 6.4 and table 6.2. The increase of statistics in the region of interest (large rapidity gaps) is almost by factor four.

The new trigger scheme summary is presented in Table 6.5

Jet algorithm	p_T (GeV)	$ \eta_{\text{jets}} < 2.9$	$ \eta_{\text{jets}} > 2.9$
Anti- k_T $R = 0.6$	$20 < p_T < 34$	L1_MBTS_1	L1_MBTS_1
	$p_T > 34$	L1_J5	L1_MBTS_1
Anti- k_T $R = 0.4$	$20 < p_T < 29$	L1_MBTS_1	L1_MBTS_1
	$p_T > 29$	L1_J5	L1_MBTS_1

Table 6.5: The new below-plateau dijet trigger scheme for 2010 period B.

6.2.9 Validation of the new trigger scheme

Since the ATLAS 2010 dijet measurement was successfully reproduced by implementing the official dijet trigger strategy, as demonstrated in Figure 6.11, it can be used to produce the p_T and η spectra. These, along with the uncorrected m_{12} distributions that we received from the inclusive dijet group, can be used to validate the newly proposed trigger strategy against. These validation plots are shown in Figures 6.12 and 6.13. The invariant mass spectra are obviously reproduced with an excellent precision of $\sim 1\%$ with the exception of the lowest m_{12} bin, where the agreement is within 2%. This is consistent with the distributions in Figure 6.13, where the p_T and η spectra collected by the new below-plateau triggers are compared to those acquired by implementing the official inclusive dijet trigger strategy.

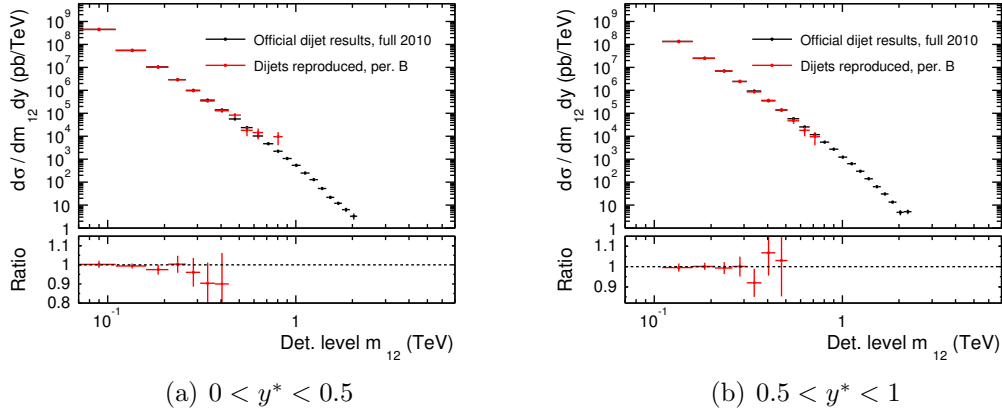


Figure 6.11: Detector level dijet invariant mass in two different y^* bins. Comparison between the 2010 inclusive dijet analysis (full 2010 data sample) and our reproduction of these results (period B) by implementing the inclusive cuts and trigger scheme. Jets were reconstructed by the anti- k_T $R = 0.6$ algorithm.

6.2.10 Trigger closure test

The trigger closure test is designed to test the influence of the trigger efficiency weighting on the shape of the $\Delta\eta^F$ (see Chapter 7) and $\tilde{\xi}^\pm$ (see Chapter 8) spectra. A bias could arise from the possible trigger efficiency dependence on

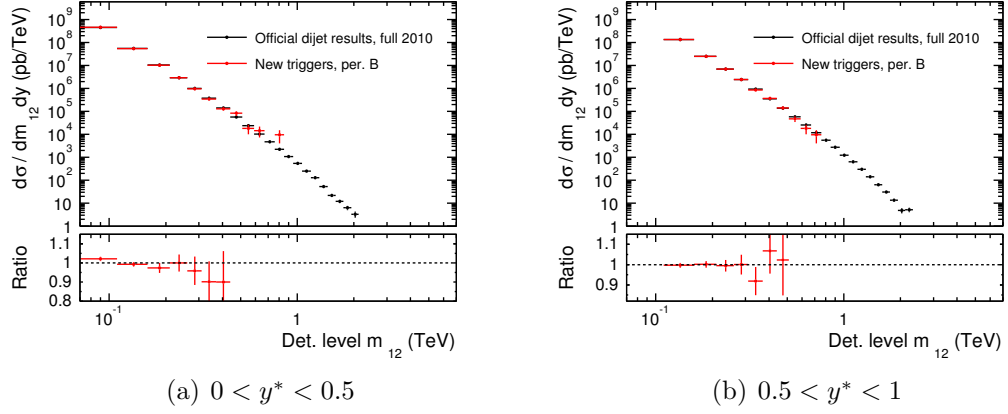


Figure 6.12: Detector level dijet invariant mass in two different y^* bins. Comparison between the 2010 inclusive dijet analysis (full 2010 data sample) and the new (below-plateau) trigger scheme (period B). Jets were reconstructed by the anti- k_T $R = 0.6$ algorithm.

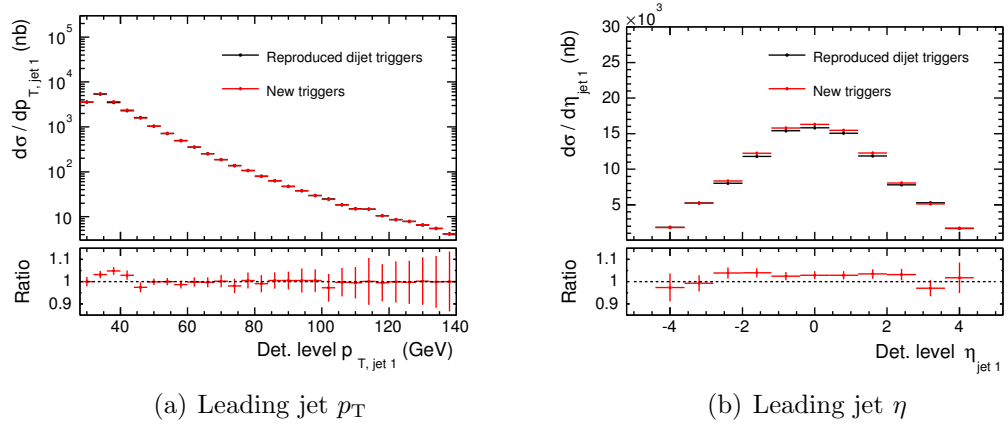


Figure 6.13: Detector level p_T and η of the leading jet as acquired by the use of the new (below-plateau) trigger scheme compared to the spectra obtained by implementing the official inclusive 2010 dijet trigger scheme. Based on the period B data, jets reconstructed by the anti- k_T $R = 0.6$ algorithm.

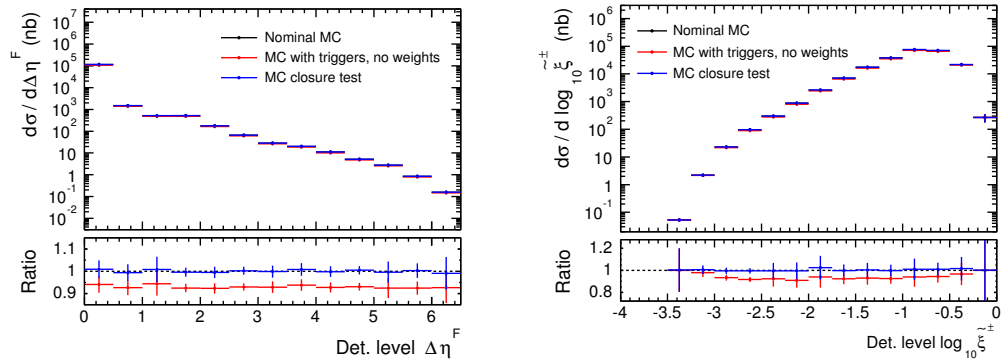


Figure 6.14: Trigger closure test on the below-plateau efficiency weighting. Ratios are calculated with respect to the “Nominal MC”. PYTHIA8 ND+SD+DD.

the $\Delta\eta^F$ and $\tilde{\xi}^\pm$ variables. To test this effect, the Monte Carlo samples well populated up to the largest gaps (smallest ξ) can be exploited. As the goal is to test the L1.J5 trigger efficiency weighting (this trigger is used starting from the $p_T^{\text{jet}} > 34$ GeV), the PYTHIA8 Monte Carlo sample can be restricted to events with the leading-jet $p_T > 34$ GeV. The trigger performance is then simulated by a random removal of events given by the trigger efficiency fits as retrieved from the data. The remaining events collected in the jet p_T region corresponding to the trigger efficiency below plateau are then normalized by the same scaling factors as are used in the data analysis. The result of this trigger closure test shown in Figure 6.14 for both the $\Delta\eta^F$ and $\tilde{\xi}^\pm$ variables clearly indicates stability of both distributions against the trigger efficiency weighting within 2%. Distributions without the weighting (but with trigger simulation) are also drawn.

6.3 Event selection cuts

The basic dijet selection cuts are based on the inclusive dijet analysis [44]. The first level of the event selection is done via the Good Runs List, already mentioned in Section 6.1. Other steps include requirements on reconstructed vertices, the already discussed trigger selection and a dijet acceptance definition based on cut on jet p_T and η .

6.3.1 Vertex requirements

There are three layers of the ATLAS tracking system which are dedicated to a precision measurement of trajectories of charged particles produced in the center of the detector. These tracks can be used to reconstruct vertices, i.e. points in the x, y, z coordinates³ where two or more tracks (after meeting certain quality criteria) originate from. Distributions of all reconstructed vertices with at least two associated tracks is shown in Figure 6.15.

Generally, the vertex reconstruction algorithm provides basic information about so-called primary vertex (PV0), i.e. the most probable candidate on the pp collision point of the hard-scale interaction, and “pile-up” vertices (additional vertices having two or more associated tracks) made-up by secondary minimum bias pp interaction. In case of diffractive events, it is possible that there is no PV0 as the diffractive system can be boosted into the forward direction, outside the acceptance of the Inner Detector. The selection of events for a usual jet-related analysis contains a requirement on the presence of PV0 with at least five associated tracks, which is designed to reject events due to cosmic ray muons and beam-induced background. This cut was also used in our analysis with a requirement that there are at least two associated tracks to the PV0⁴.

³ATLAS uses the right-handed coordinate system with the z axis pointing in the direction of the beam, x axis to the geometrical center of the LHC and y axis perpendicular to both x and z .

⁴Requiring five tracks would pose an additional requirement on larger particle activity in the central region, which is unnecessary limitation for the rapidity gap measurement; two associated tracks is sufficient for removing cosmics and beam-induced background

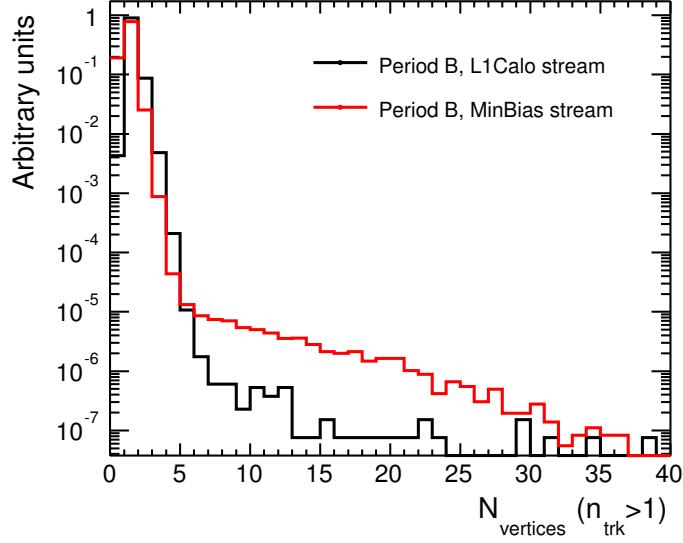


Figure 6.15: Distributions of reconstructed vertices with two or more associated tracks in L1Calo and MinBias stream of 2010 period B. Distributions are normalized to unity.

Since the instantaneous luminosity in examined data runs is such that there is a potential for multiple collisions in the same bunch crossing, additional vertex requirement was employed to reject such events: besides the primary vertex with at least two associated tracks, there should not be any additional pile-up vertex (having two or more associated tracks).

The probability that there are zero ($P(0)$), one ($P(1)$) or more ($P(\geq 2)$) interactions in the same bunch crossing can be calculated using Poisson statistics. After asking that a primary vertex is reconstructed, and taking the mean number of interactions per bunch crossing to be 0.144, corresponding to the peak $\langle\mu\rangle$ value in run 155112 (Table 6.1), the multiplier factor f by which the data with pile-up suppression cut must be corrected, is

$$f = 1 + \frac{P(\geq 2)}{P(\geq 1)} = 1 + \frac{1 - P(0) - P(1)}{1 - P(0)}. \quad (6.6)$$

Using the Poisson statistics to evaluate $P(0)$ and $P(1)$, the result is $f^{\text{Theor.}} = 1.07$.

The primary vertex (with 2 or more associated tracks) requirement removes approximately 0.4% of events passing the GRL in the L1Calo and 19.1% in the MinBias data stream. From a sample with at least one primary vertex, the fraction of events with more than one interaction in the same bunch crossing is measured to be approximately 9.3% in L1Calo and 3.3% in MinBias stream. Once the event is triggered and the dijet selection criteria is met, the requirement on a presence of the primary vertex removes 0.3% of events in L1Calo and 0.2% in MinBias stream, while the actual fraction of events rejected by the pile-up suppression cut is 9.4% in L1Calo and 6.5% in MinBias stream. We therefore get $f^{\text{L1Calo}} = 1.094$ and $f^{\text{MinBias}} = 1.065$. These values are used to scale the measured cross section to account for the loss of events due to the pile-up suppression cut

(not more than one reconstructed vertex with two or more associated tracks per event).

6.3.2 Jet kinematic selection

Jets in data are reconstructed from topological clusters (TopoClusters or simply clusters)⁵ [46] at the EM+JES scale, that is with calibration based on the electromagnetic scale (EM) with jet energy scale factors (JES)⁶ [47] based on a jet energy and rapidity (known as EM+JES). The anti- k_T algorithm of two jet resolution parameters, $R = 0.4$ and $R = 0.6$ [43], was used. The corresponding particle level definition is based on all stable final state particles, using also the anti- k_T algorithm of the same resolution parameters.

The dijet selection adopted in this analysis requires leading and sub-leading jets (ordered according to their p_T) with transverse momenta $p_T > 20$ GeV and with jet barycenters within $|\eta| < 4.4$. The η cut ensures that jets are well contained within the ATLAS calorimeter acceptance range so that no significant jet energy escapes undetected.

The transverse momentum cut $p_T > 20$ was chosen with respect to the attempt to boost statistics at large rapidity gaps (small ξ) and to the limitation of the jet energy scale (not well understood for $p_T < 20$ GeV). The same p_T and η cuts are used for particle level Monte Carlo studies. Data to MC comparisons are shown in Figure 6.16, which suggests that the PYTHIA8 systematically overestimates inclusive dijet production cross section by factor ~ 1.4 .

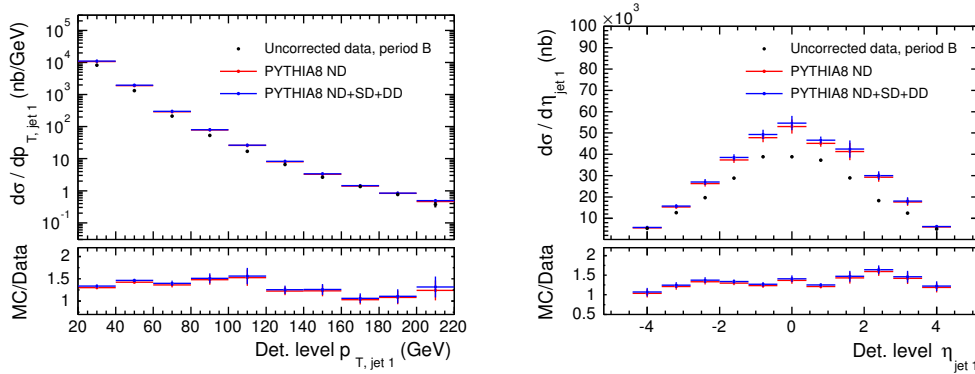


Figure 6.16: Detector level p_T and η distributions of the leading jet in comparison with the PYTHIA8 Monte Carlo events.

⁵TopoCluster is reconstructed from a seed calorimeter cell with $|E_{\text{cell}}| > 4\sigma$, where σ is the RMS of the noise of the cell. Neighbouring cells are iteratively added in case they have $|E_{\text{cell}}| > 2\sigma$.

⁶Energy calibration factors that must be applied to reconstructed jets to account for a limited calorimeter response to the deposited energy.

6.3.3 Jet cleaning

Both the leading and the sub-leading jet are required to pass ATLAS medium-type quality cleaning cuts⁷ and not to be “ugly”⁸ (for jet cleaning details, see [44]). The effect of the jet cleaning differs based on the jet p_T and η range and must be corrected for in the physics analysis by introducing appropriate event weights. These correction factors are depicted in Figure 6.17.

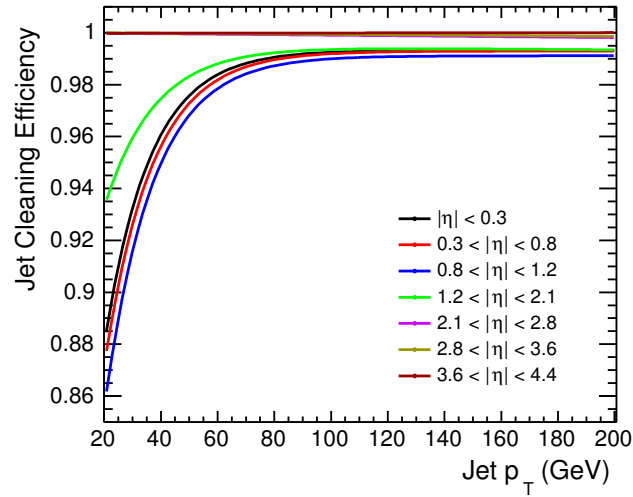


Figure 6.17: Jet cleaning efficiency correction factors for EM+JES calibrated jets. Values used in this plot taken from [44].

⁷Removes contribution from cosmic muons, detector noise, beam-background, crack region, etc.

⁸“Ugly” jets have most of their energy deposition in problematic calorimeter regions, where the energy measurement is not sufficiently accurate.

7. Rapidity gap measurement

Rapidity gaps, i.e. large pseudorapidity regions with no particle activity, represent a key diffractive signature. The interpretation of such events is straightforward: since large rapidity gaps are rare in non-diffractive interactions (fluctuations in hadronisation process causing rapidity gaps are exponentially suppressed), a simple cut on the size of the rapidity gap can be used to significantly enhance the diffractive contribution in the studied data sample. The measured rapidity gap distribution can be directly compared to various diffractive models, providing thus a useful feedback for theorists about their predictions.

In this chapter, various rapidity gap definitions, influence of the detector noise and detector level (uncorrected) data distributions (in comparison with MC models) are presented. The fully corrected distributions are shown and discussed in Chapter 12.

Throughout this chapter, all ratio plots are calculated as a colored histogram divided by a black histogram, with error bars representing the overall statistical uncertainty of the ratio.

7.1 The Forward Rapidity Gap

The Forward Rapidity Gap, denoted throughout this thesis as $\Delta\eta^F$, is specific for single diffractive events in which the rapidity gap is measured between the scattered proton (its typical ξ is so small that it remains in the beam pipe) and first stable (proper lifetime $\tau c > 10$ ps) final state particle (hereafter referred to as “truth” particles or the “particle level”¹) produced by the dissociation process of the other interacting proton.

The detector level definition of $\Delta\eta^F$ (detector level variables are also called “reco”) is based on the soft rapidity gap analysis [45] and takes advantage of the acceptance of the ATLAS calorimeter system ($|\eta| < 4.9$) and the Inner Detector ($|\eta| < 2.5$). The Forward Rapidity Gap is the largest empty area in the ATLAS detector ranging from the edge of the calorimeter system ($\eta = -4.9$ or $\eta = 4.9$) up to the first detector object (TopoCluster or track).

7.2 Noise removal

The rapidity gap measurement is very sensitive to the electronic noise of the calorimeter system and to fakes in charged-particles candidates (tracks). For this reason, sophisticated noise removal and cleaning cuts had to be adopted. They are based on the soft rapidity gap analysis [45].

¹In some plots, the term “hadron level” is also used.

7.2.1 Track cleaning

Good tracks are required to have $p_T > 200$ MeV and $|\eta| < 2.5$ (standard ATLAS selection). Additional quality selection criteria (ensuring, among others, that tracks originating from the hard primary interaction are used) are as follows:

- At least one hit in the Pixel layer
- At least one hit in the B-layer
- p_T -dependent number of hits in the SCT layer: $n_{p_T \geq 100 \text{ MeV}} \geq 2$, $n_{p_T \geq 200 \text{ MeV}} \geq 4$, $n_{p_T \geq 300 \text{ MeV}} \geq 6$
- $|d_0| < 1.5$ mm with respect to the primary vertex
- $|z_0 \sin \theta| < 1.5$ mm with respect to the primary vertex

The variable d_0 is the transverse component of the impact parameter (a displacement to the primary vertex) and $z_0 \sin \theta$ represents the longitudinal component of the impact parameter. If no primary vertex is reconstructed, the d_0 and z_0 selection cuts are calculated with respect to the beam spot.

7.2.2 Cluster noise

The electronic noise of ATLAS calorimeters presents the main challenge for the measurement of $\Delta\eta^F$. The calorimeter objects used for the gap finding algorithm are TopoClusters, for which a variable called *significance* can be defined as

$$S = \frac{E_{\text{cell}}}{\sigma_{\text{noise}}} \quad (7.1)$$

where E_{cell} is the energy of the most significant cell with $S > 4$ (the seed cell, see Section 6.3.2) in the cluster.

The variable S can be tuned to provide a very good noise suppression in the rapidity gap finding algorithm. This was studied into detail in the ATLAS soft rapidity gap analysis [45] and it is therefore adopted here as well. The summary of this approach is in next three paragraphs.

Shapes of the cell noise distributions were measured to be Gaussian with the standard deviation σ_{noise} . The only exception is the Tile calorimeter which has non-Gaussian tails [48] and was therefore not considered for the gap finding algorithm. For the Gaussian-shaped noise distribution, the probability of the energy of the noise exceeding significance S is given by

$$P_{\text{noise}}(S) = \sqrt{\frac{1}{2\pi}} \int_S^\infty e^{-s^2/2} ds \quad (7.2)$$

The default $S > 4$ cut used by the cluster reconstruction algorithm is too low for the rapidity gap analysis: on average, six clusters per an empty event are reconstructed due to noise fluctuations. That is enough to significantly influence the reconstructed $\Delta\eta^F$ distribution. For this reason, an additional noise suppression cut based on the η -dependent cell significance threshold (applied to the

most significant cell in the TopoCluster) was developed. The original gap reconstruction algorithm in the soft gap analysis used so-called “rings”, i.e. slices in pseudorapidity of the size 0.1. The probability P_{noise} was chosen to be 1.4×10^{-4} following the minimization of the resolution of reconstructed rapidity gap sizes with respect to gaps at the particle level in MC (this choice benefits from stability for small S_{th} changes in either direction, up or down). This implies an overall per-event noise fluctuation probability 1.4% (as there are 98 clusters η -rings). As the number of cells in η -rings varies from about 4000 in the central region to 10 in the very forward region, the thresholds S_{th} vary between 5.8 (central) and 4.8 (forward), see Figure 7.1.

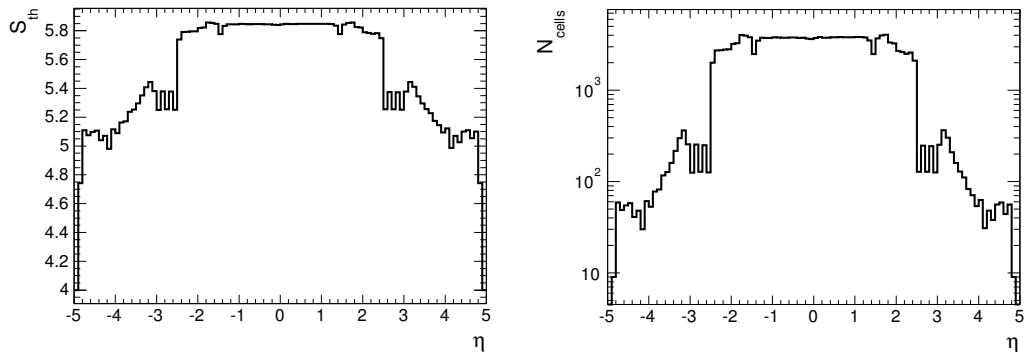


Figure 7.1: η -dependent cell significance thresholds for the noise removal for the $\Delta\eta^F$ reconstruction (left) and the number of cells in given η -ring (right).

The above discussed algorithm obviously relies on good modeling of the cell noise in the MC. The description was studied in detail for rapidity gap cross section measurement in minimum bias events, see Section 2.3 in [45]. As an example, Figure 7.2 displays the cell significance E/σ for EM and FCal calorimeters. Very good description was observed for E/σ going beyond the typical cut ($E/\sigma \sim 5.5$), giving us a confidence that the effect of the cut is the same in both data and MC. For the dijet analysis, the cell information is not stored in our ntuples. But since data and MC is used in the same configuration as for the minimum bias gap analysis, a good detector modeling of noise is assumed.

7.3 TopoClusters

Another ATLAS measurement useful for the analysis presented in this thesis is the measurement of the pseudorapidity dependence of the total transverse energy [49] (henceforth referred to as the “ E_T -flow” analysis). It provides a useful insight into the energy distributions as measured by the ATLAS calorimeter system and comparisons between data and Monte Carlos.

7.3.1 Cluster energy correction in MC

The E_T -flow analysis includes a study of the $\pi^0 \rightarrow \gamma\gamma$ decays. The comparisons between the MC and data of the reconstructed π^0 mass peak showed that the EM scale cluster energy response is not correctly simulated in the MC samples

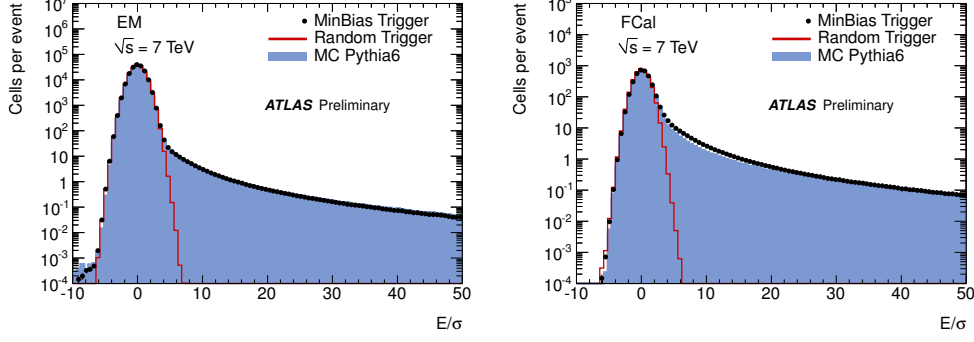


Figure 7.2: Cell significance E/σ for EM calorimeters (left) and FCal (right) obtained from MC, data and empty random events in data. Taken from Section 2.3 in [45].

and that scaling factors have to be applied (in MC only) to get a response to low-energy particles in accordance with the one observed in the data. The shifts, $1 + \alpha$, are listed in Table 7.1 along with their uncertainties. The uncertainties are presented separately for EM particles and hadrons, but combined uncertainty based on an assumption that around 27% of particles are EM. These energy corrections, ranging from about 1% to almost 11%, have impact on the ξ measurement only (see Chapter 8 as the $\Delta\eta^F$ definition does not use any energy-related cluster cut).

Cluster η	α	σ (EM-particles)	σ (Hadrons)	σ (Combined)
$-4.8 < \eta < -4.2$	0.04	-0.023, +0.023	-0.023, +0.093	-0.023, +0.074
$-4.2 < \eta < -3.5$	-0.017	-0.032, +0.034	-0.032, +0.096	-0.032, +0.079
$-3.5 < \eta < -3.2$	0.01	-0.098, +0.11	-0.098, +0.14	-0.098, +0.13
$-3.2 < \eta < -2.8$	-0.027	-0.023, +0.025	-0.023, +0.06	-0.023, +0.051
$-2.8 < \eta < -2.37$	-0.089	-0.025, +0.029	-0.025, +0.062	-0.025, +0.053
$-2.37 < \eta < -1.52$	-0.022	-0.021, +0.02	-0.05, +0.05	-0.042, +0.042
$-1.52 < \eta < -1.37$	-0.073	-0.17, +0.18	-0.05, +0.05	-0.084, +0.085
$-1.37 < \eta < -0.8$	-0.017	-0.031, +0.025	-0.05, +0.05	-0.045, +0.043
$-0.8 < \eta < 0.0$	-0.017	-0.031, +0.025	-0.035, +0.035	-0.034, +0.032
$0.0 < \eta < 0.8$	-0.013	-0.031, +0.025	-0.035, +0.035	-0.034, +0.032
$0.8 < \eta < 1.37$	-0.013	-0.031, +0.025	-0.05, +0.05	-0.045, +0.043
$1.37 < \eta < 1.52$	-0.013	-0.17, +0.18	-0.05, +0.05	-0.084, +0.085
$1.52 < \eta < 2.37$	-0.031	-0.021, +0.02	-0.05, +0.05	-0.042, +0.042
$2.37 < \eta < 2.8$	-0.107	-0.025, +0.029	-0.025, +0.062	-0.025, +0.053
$2.8 < \eta < 3.2$	-0.054	-0.023, +0.024	-0.023, +0.06	-0.023, +0.051
$3.2 < \eta < 3.5$	0.04	-0.092, +0.1	-0.092, +0.14	-0.092, +0.13
$3.5 < \eta < 4.2$	-0.042	-0.032, +0.034	-0.032, +0.096	-0.032, +0.079
$4.2 < \eta < 4.8$	0.01	-0.023, +0.023	-0.023, +0.093	-0.023, +0.074

Table 7.1: Cluster energy correction factors and their systematic uncertainties in η bins for EM and hadronic particles (applicable in MC only). The combined uncertainty assumes 27% of particles are EM with the remainder being hadronic. Taken from [49].

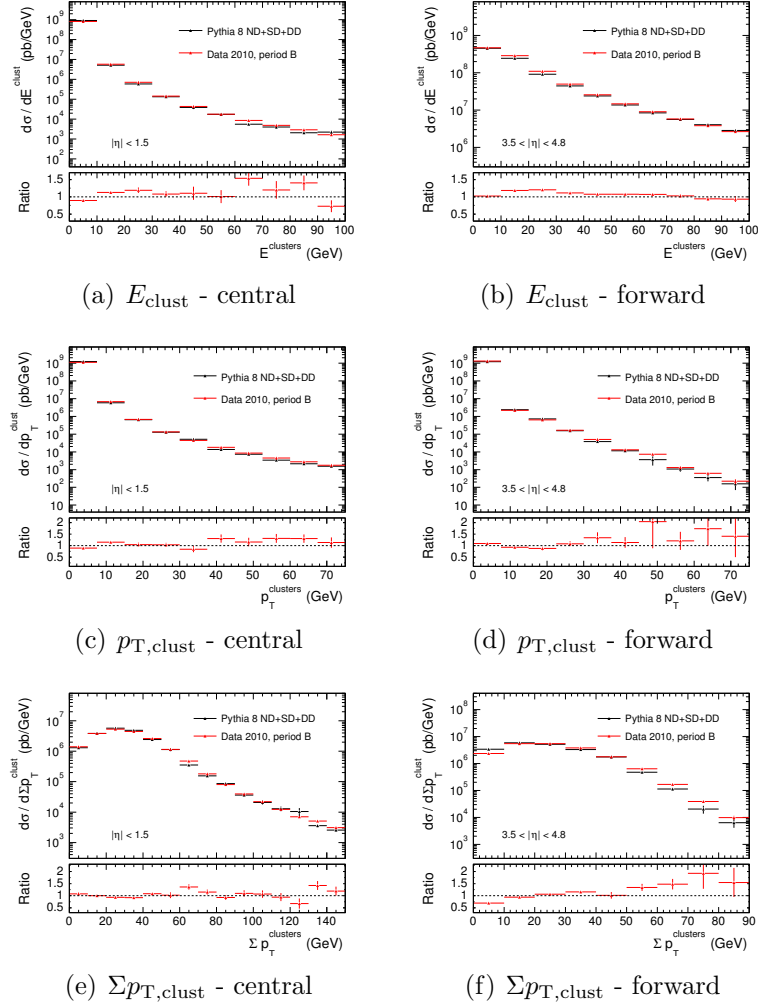


Figure 7.3: Basic cluster distributions at the EM-scale as seen in the data and compared to PYTHIA8 ND+SD+DD. Standard dijet selection cuts and cell significance cuts applied. PYTHIA8 ND is scaled to match the data in the first $\Delta\eta^F$ bin (see later on in this chapter). The error bars represent statistical uncertainties.

7.3.2 Basic kinematic properties

TopoClusters as basic calorimeter objects available by default for physics analysis were already briefly discussed in Section 6.3.2. Since they are the cornerstone of the rapidity gap analysis as well as the ξ measurement (see Chapter 8), it is appropriate to introduce their properties. Data to MC comparisons after standard dijet selection and cluster noise-removing cuts are presented in Figure 7.3 for three different distributions (E , p_T and sum p_T) and two different pseudorapidity ranges (central and forward clusters). Though not perfect, the description of the data by PYTHIA8 samples is reasonably good in the central as well as forward region. What is especially important for the sake of the diffractive dijet analysis presented in this thesis is the fact that shapes of distributions studied are approximately the same in the data and the MC, taking into account statistical uncertainties, so the simulation of the calorimeter response in MC can be trusted and used for

$\Delta\eta^F$ and ξ definitions.

7.4 Rapidity gap definition in the soft gap analysis (“ p_T -method”)

The ATLAS soft gap analysis defined the “empty detector” based on a presence of tracks passing cleaning cuts (see Section 7.2.1) and TopoClusters with the most significant cell above the significance thresholds (see Section 7.2.2). The forward rapidity gap was then defined as the larger pseudorapidity difference between one of the edges of the calorimeter ($\eta = \pm 4.9$) and the first good track or TopoCluster. An additional transverse momentum cut $p_T > 200$ MeV was applied to clusters (and matches the one used for good tracks selection). The particle level rapidity gap definition is based on all final state particles having $p_T > 200$ MeV and the same acceptance region as in the detector level definition ($|\eta| < 4.9$). This rapidity gap definition is henceforth denoted as the “ p_T -method”.

The p_T -method was examined in the diffractive dijet analysis. The detector level (uncorrected) distributions are presented in Figure 7.4, where the data is compared to PYTHIA8 and Herwig++ predictions. Comparisons between PYTHIA8 and the data show that the events with small $\Delta\eta^F$ are significantly dominated by the ND contribution. In the very first bin, $\Delta\eta^F = 0 - 0.5$, the SD and DD components are negligible and it can therefore be used to scale the PYTHIA8 ND $\Delta\eta^F$ cross section prediction by a constant factor 1/1.4 to match the data. With the increasing gap size, the ND dominance significantly decreases while the importance of diffractive components (SD and DD) steadily increase. Unlike in the soft diffraction, there is no diffractive plateau ($\Delta\eta^F$ cross section constant) observed due to requiring a presence of two relatively high- p_T jets. That is roughly equivalent to high particle multiplicities (or high invariant masses of the diffractive system).

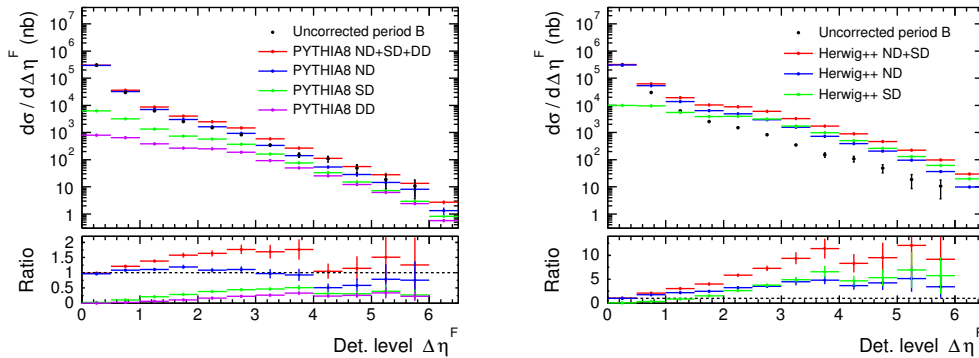


Figure 7.4: Detector level data to PYTHIA8 (left) and Herwig++ (right) comparisons. PYTHIA8 ND is scaled to match the data in the first $\Delta\eta^F$ bin. Jets reconstructed by the anti- k_T $R = 0.6$ algorithm. The error bars represent statistical uncertainties.

7.4.1 Herwig++ issues

Figure 7.4 reveals significant issues in the Herwig++ prediction of the shape of the $\Delta\eta^F$ spectrum. The lowest $\Delta\eta^F$ bin in the data is described very well without any additional scaling factor, contrary to the PYTHIA8 case. But the shape of the ND component is not falling away exponentially as expected (and observed in PYTHIA8 prediction). As a result, Herwig++ completely fails to describe the shape of the rapidity gap distribution.

The same effect was observed in the ATLAS soft gap analysis. As a consequence of unexpectedly large rapidity gaps being produced by Herwig++ model, the soft diffractive plateau was observed even in the non-diffractive Herwig++ events. The main difference between Herwig++ and PYTHIA8 lies in the hadronisation model: Herwig++ uses the cluster-based hadronisation (see Section 4.3). This model fails in the splitting procedure of the high-mass clusters, resulting in creation of large pseudorapidity regions without any particle activity. This has a significant impact on the rapidity gap spectrum, as can be seen from Figure 7.4.

The effect of these hadronisation fluctuations can be also assessed in the SD events by a comparison between the usual gap finding procedure (i.e. based on particles with $p_T > 200$ MeV within $|\eta| < 4.9$) and the position of the scattering proton. The real rapidity gap should be located between the scattered proton and the first particle from the dissociating proton. Table 7.2 presents percentages of events that have the particle level rapidity gap located at the same side of the ATLAS detector as the scattered proton. In PYTHIA8 there are 35% of events with mismatched gap start, an effect which is expected at such small rapidity gaps due to hadronisation fluctuations. At larger rapidity gaps, mismatches are almost non-existent. In contrast, the Herwig++ SD model produces around 40–45% of events with rapidity gaps on the opposite side than the scattered proton across full $\Delta\eta^F$ range.

$\Delta\eta^F$:	0–0.5	0.5–1	1–2	2–3	3–4	4–5	5–6	6–7
PYTHIA8 SD	65%	85%	93%	97%	98%	98%	99%	99%
Herwig++ SD	53%	56%	55%	53%	51%	51%	54%	57%

Table 7.2: Percentage of SD events with the particle level $\Delta\eta^F$ starting at the same side of the ATLAS detector as the true gap (based on the p_z sign of the scattered proton).

Originally, Herwig++ along with PYTHIA8 were supposed to be our default independent MC generators providing a possibility to asses model dependence influencing our measurement via the unfolding procedure (see Chapter 9). Due to these issues that couldn't be sorted out, Herwig++ MC production is considered unsuitable for the rapidity gap analysis.

7.5 Optimization of the Forward Rapidity Gap definition (“hybrid method”)

The correlation matrices between the particle level and detector level definitions for the p_T -method are shown in Figure 7.5. Rather weak correlations are observed at small gaps and hence suggest that the common p_T cut on clusters as well as particles is resulting in arbitrarily large detector level rapidity gaps. As we shall see, this has been also confirmed by qualitative studies of bin-by-bin purities.

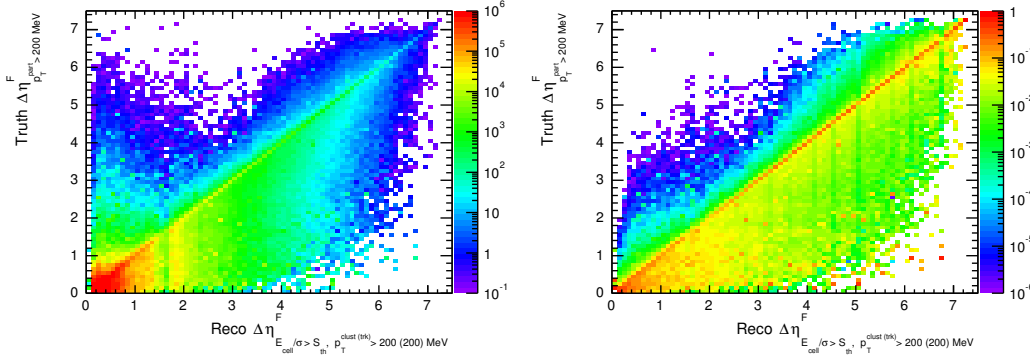


Figure 7.5: Left: Smearing matrix of the $\Delta\eta^F$ variable for the p_T -method, i.e. $p_T^{\text{particles}} > 200$ MeV, $p_T^{\text{tracks}} > 200$ MeV, $p_T^{\text{clusters}} > 200$ MeV, $E_{\text{cell}}/\sigma_{\text{noise}} > S_{\text{th}}$. Right: The same but columns normalized to unity. Pythia8 ND+SD+DD.

The obvious solution to this issue could be easing the p_T^{cluster} cut. Though this possibility has been also studied, as is shown in Figure 7.6, a different approach has been eventually chosen. The $p_T^{\text{clusters,particles}}$ requirement at $|\eta| < 4.9$ corresponds to a cluster or truth particle with $E > 13.4$ GeV², meaning that clusters and stable final state particles at the edge of the detector acceptance are required to be much more energetic than those in the barrel. The cluster rejection power of this selection significantly exceeds, in the forward region, the one coming from S_{th} cut. For this analysis, the cluster and truth particle selection were adapted to combine the method from the ATLAS soft rapidity gap analysis and the selection from the E_T -flow analysis [49] (so-called “ E_T -flow method”), to better reflect which particles can actually reach the active layers in the calorimeter, hereafter referred to as the “hybrid” selection or “hybrid method”.

The track selection cuts remain unchanged (E_T -flow analysis focused on studying the calorimeter response), but the cluster p_T requirement is removed and the calorimeter acceptance cut is changed to $|\eta| < 4.8$, as very few clusters are well reconstructed too close to the edge of the detector acceptance.

At the particle level, instead of the $p_T > 200$ MeV selection for final state particles up to $|\eta| < 4.9$, the selection is changed to $p_n > 200$ MeV for neutral particles. For charged particles, the choice is to have either $p_{\text{ch}} > 500$ MeV or

²The relation between η , p_T and p is given by $|p| = p_T \cosh \eta$.

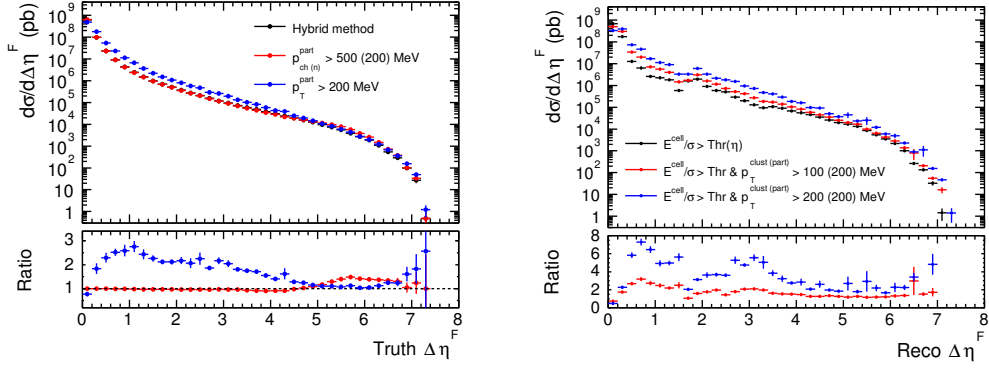


Figure 7.6: Gap-size distributions for different definitions at the particle level (left) and the detector level (right). The error bars represent statistical uncertainties. PYTHIA8 ND+SD+DD.

$p_{T, \text{ch}} > 200$ MeV, up to $|\eta| < 4.8$. For this choice, the value of $|\eta| = 1.57$ is important as $p > 500$ MeV is equivalent to $p_T > 200$ MeV and thus keeping the p_T cut (in logical OR with $p_{\text{ch}} > 500$ MeV) helps to exploit the sensitivity of the tracker. The difference in momentum cuts for neutral and charged particles matches the range over which the E_T -flow analysis indicates that the particles are likely to reach the tracker and calorimeters, accounting for the solenoidal magnetic field surrounding the Inner Detector.

Comparisons of the different gap definition methods are presented in Figure 7.6 and Table 7.3. Ratios with respect to the hybrid method are plotted as well. It is clear from the particle level figure that the original symmetrical (cluster-particle) p_T cuts cause significant event migrations from small gaps to larger $\Delta\eta^F$ compared to both the hybrid and E_T -flow method (particle cuts $p_{\text{ch}(n)} > 500$ (200) MeV and $|\eta| < 4.8$ only). The same conclusion can be drawn from the detector level plot. It is therefore obvious that the hybrid gap definition is more successful in exploiting the ATLAS detector sensitivity to low- p_T particles.

$\Delta\eta^F$ method	Particle level definition	Detector level definition
2010 minimum bias definition	$p_T^{\text{particles}} > 200$ MeV $ \eta < 4.9$	Clusters: $p_T > 200$ MeV, $ \eta < 4.9$ and $ E_{\text{cell}}/\sigma_{\text{noise}} > S_{\text{thr}}(\eta)$ Tracks: $p_T > 200$ MeV, $ \eta < 2.5$
E_T flow	Neutral particles: $p > 200$ MeV, $ \eta < 4.9$ Charged particles: $p > 500$ MeV, $ \eta < 4.9$	Clusters: $ E_{\text{cell}}/\sigma_{\text{noise}} > S_{\text{thr}}(\eta)$, $ \eta < 4.9$ Tracks: $p_T > 200$ MeV, $ \eta < 2.5$
Hybrid method	Neutral particles: $p > 200$ MeV Charged part.: $p > 500$ MeV or $p_T > 200$ MeV $ \eta < 4.8$	Clusters: $ E_{\text{cell}}/\sigma_{\text{noise}} > S_{\text{thr}}(\eta)$, $ \eta < 4.8$ Tracks: $p_T > 200$ MeV, $ \eta < 2.5$

Table 7.3: Summary of the rapidity gap definition methods studied in this paper.

Finally, very illustrative method comparisons are presented in Figure 7.7. Correlation matrices clearly indicate that the p_T -method tends to create, especially in the forward region (small rapidity gaps), a large portion of fakes (i.e. events with artificially increased gap size due to too strict gap defining cuts) while the hybrid vs. E_T -flow is rather a fine-tuning resulting in a slightly better truth-reco correspondence (as already discussed in the paragraph where the hybrid method was introduced).

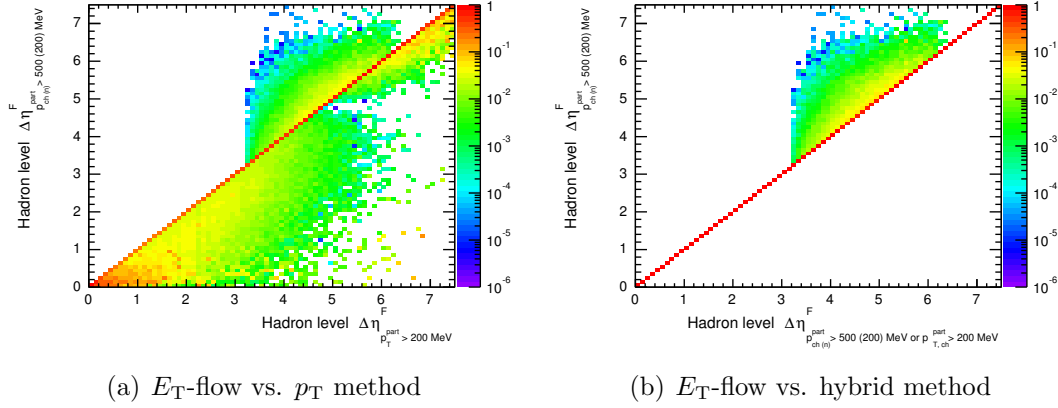


Figure 7.7: Correlation plots among different gap definition methods. (a) E_T -flow (y -axis) vs. p_T method (x -axis), (b) E_T -flow (y -axis) vs. hybrid method (x -axis). Columns normalized to unity. PYTHIA8 ND+SD+DD.

To get a qualitative picture of the different methods, it is advisable to study purities (how many of the detector level events in a chosen bin are in the same particle level bin) and resolutions (differences between particle and detector level values). The effect of purities is reflected in 2D correlation histograms, such as those in Figure 7.8, but can be also evaluated numerically. Results of such calculations are presented in Table 7.4. Our earlier observation of the arbitrarily large number of fakes in smearing matrices in Figure 7.5 is reflected in purities, which are around (or even below) 30%. Lowering of the clusters p_T cut results in significant purity increase - an effect which is seen for hybrid method as well.

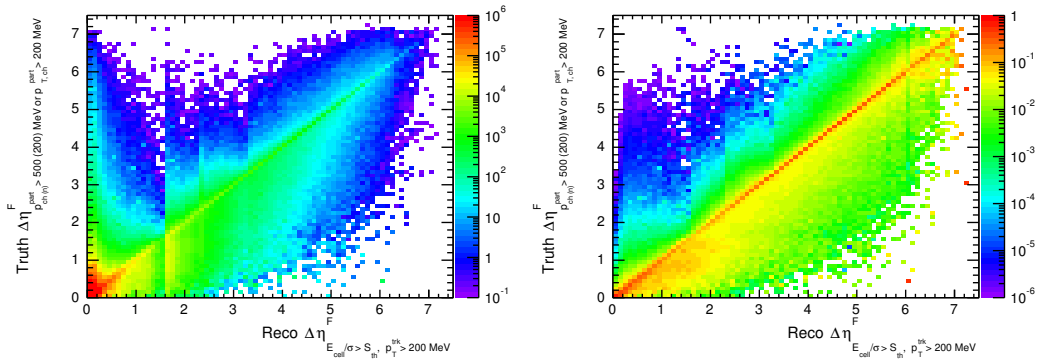


Figure 7.8: Smearing matrix of the $\Delta\eta^F$ variable for the hybrid method normalized to the cross section (left) and the same with columns normalized to unity (right). PYTHIA8 ND+SD+DD.

The resolutions plots in steps of one unit of $\Delta\eta^F$ are shown in Figure 7.9. They reveal an exponential-like decrease with respect to the maximum (being close to zero) as well as a second distribution - though significantly suppressed - with

Reco $\Delta\eta^F$	0 - 1	1 - 2	2 - 3	3 - 4	4 - 5	5 - 6
$p_T^{\text{clust(part)}} > 200$ (200) MeV	99.7%	34%	23%	28%	33%	30%
$p_T^{\text{clust(part)}} > 100$ (200) MeV	99%	58%	46%	56%	54%	46%
no clusters p, p_T cut $p_{\text{ch(n)}}^{\text{part}} > 500$ (200) MeV	99.8%	49%	38%	48%	49%	58%
Hybrid method	99.8%	49%	38%	50%	52%	56%

Table 7.4: Purities for different $\Delta\eta^F$ definitions. Pythia 8 ND+SD+DD

detector level gaps significantly larger than particle level gaps. The latter effect can be understood by studying the Figure 7.8, which shows a distinctive region of small detector level gaps but large particle level gaps. This atypical behaviour can be explained as a consequence of a limited ATLAS calorimeter acceptance ($|\eta| < 4.8$) and a presence of material even outside this acceptance region. This in turn means that a particle moving just outside the $|\eta| < 4.8$ region can cause a shower which can partly hit the edge of the calorimeter. This is confirmed by Figure 7.10, where the reco-truth correlation matrix is shown with the condition that the particle level gaps are required to range from the position of the diffractive proton instead of the calorimeter edge (in case of ND or DD events, the particle level gap edge is defined as $|\eta| = 7$).

Finally, the qualitative view at the resolutions is summarized in Table 7.5. Each bin is characterized by three numbers: the mean value (calculated across the whole range), root-mean-squared (RMS) of the part of the resolution plot that is to the left from the mean value and RMS to the right-side of the mean. This calculation method is not optimal (the shape of resolutions does not allow to perform a good Gaussian fit) but it gives a clearer insight into the resolution performance of different gap definition methods. One should bear in mind, however, that the RMS to the right side of the mean is compromised by the presence of the second distribution due to the calorimeter-edge effect described above.

Truth $\Delta\eta^F$	0 - 1	1 - 2	2 - 3	3 - 4	4 - 5	5 - 6
$p_T^{\text{clusters}} > 200$ MeV	-0.13	-0.28	-0.18	-0.11	-0.09	0.07
$p_T^{\text{particles}} > 200$ MeV	0.51; 0.15	0.77; 0.51	0.70; 0.59	0.63; 0.54	0.55; 0.69	0.33; 1.20
$p_T^{\text{clusters}} > 100$ MeV	-0.05	0.15	0.19	0.15	0.05	0.25
$p_T^{\text{particles}} > 200$ MeV	0.20; 0.21	0.58; 0.72	0.52; 1.34	0.47; 1.82	0.47; 1.84	0.37; 2.12
no clusters p, p_T cut	-0.07	-0.002	0.05	0.10	0.28	0.60
$p_{\text{ch(n)}}^{\text{part}} > 500$ (200) MeV	0.14; 0.22	0.71; 0.77	0.64; 1.19	0.53; 1.72	0.48; 2.14	0.61; 2.30
Hybrid method	-0.07	-0.002	0.05	0.10	0.20	0.43
$p_{T,\text{part}}^{\text{central}} > 200$ MeV	0.14; 0.22	0.71; 0.77	0.64; 1.19	0.63; 1.56	0.44; 2.54	0.51; 3.00

Table 7.5: Resolutions: mean values and the RMS calculated to the left and right side from the mean. In each cell, the mean value is located at the top, the “left RMS” at the bottom left and “right RMS” at the bottom right. PYTHIA8 ND+SD+DD

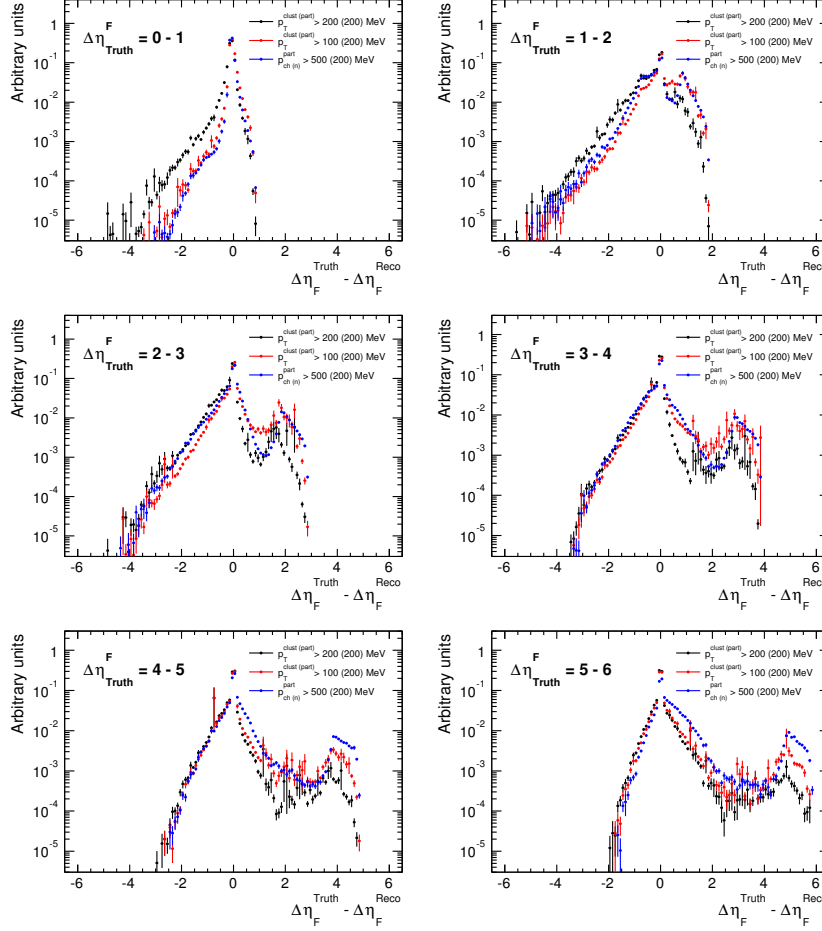


Figure 7.9: Resolutions of $\Delta\eta^F$ for different gap definition methods. The error bars represent statistical uncertainties. PYTHIA 8 ND+SD+DD.

7.6 Rapidity gap acceptance

By definition, the rapidity gaps sizes can be observed in the range $0 < \Delta\eta^F < 9.6$ (TopoClusters up to $|\eta| < 4.8$ are used). There are, however, certain limitations that decrease this default range. One of them was already discussed in Section 7.4: the requirement on a presence of two high- p_T jets. A very similar effect on the gap size distribution has the primary vertex cut, as can be seen from Figure 7.11. The detector level comparison among two different PV0 cuts (with five and two associated tracks) and no explicit PV0 cut is shown. The PV0 cut is so effective in rejecting events with very large $\Delta\eta^F$ since it requires several sufficiently energetic charged particles seen in the Inner Detector.

A comparison of the detector level $\Delta\eta^F$ to the particle level distribution, where no PV0 quantity is defined, reveals an actual acceptance range in the ATLAS detector, see Figure 7.11 (standard dijet selection cuts applied). A comparison to the particle level with a requirement simulating the effect of the PV0 cut (requiring a presence of two charged particles with $p_T > 150$ MeV and $|\eta| < 2.5$) is also shown. There should be a reasonable correspondence between the particle level and the detector level distributions to avoid too large corrections that would have

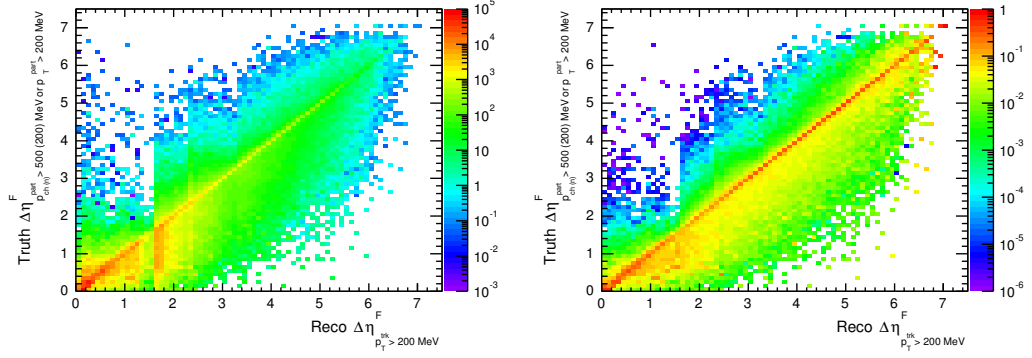


Figure 7.10: Smearing matrix of the $\Delta\eta^F$ variable for the hybrid method with the particle level gap definition starting at the η of the diffractive proton (SD events) or at the $\eta = \pm 7$ (ND and DD events). The smearing matrix is normalized to the cross section (left) or has columns normalized to unity (right). PYTHIA8 ND+SD+DD.

to be done by the unfolding procedure (corrections of the measured distribution for detector effects, see Chapter 9). These truth-reco discrepancies are caused either by “fake events” (detector level selection is passed but the particle level is not) or “missing events” (particle level selection passed but detector level is not). Fake and missing events can be caused by the jet energy resolution (truth jet p_T below 20 GeV but reconstructed as $p_T > 20$ GeV or vice versa) or the non-perfect understanding of the detector sensitivity to low-energy particles (gap definition using too low- p_T particles or too strict noise-removal cuts on clusters and tracks). From the ratio plot it is obvious that the appropriate measurement range is $0 < \Delta\eta^F < 6.5$ as beyond that, the gap reconstruction efficiency is suppressed by a factor more than two.

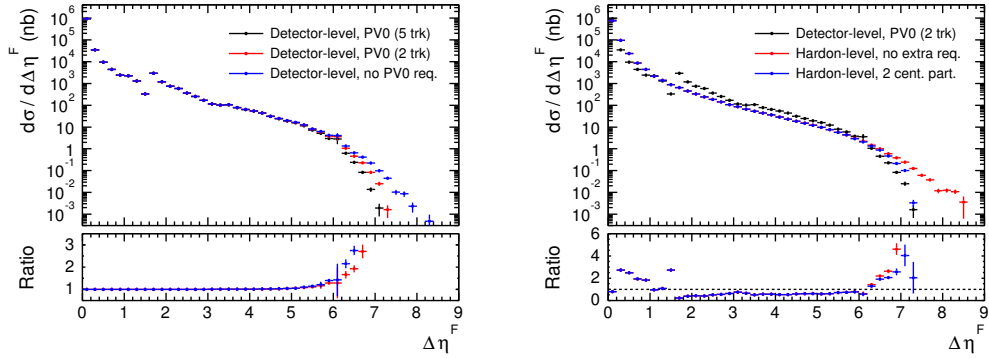


Figure 7.11: Influence of the different versions of the primary vertex cut at the detector level rapidity gap distribution (left) and reco-truth comparisons for the primary vertex cut with at least two associated (denoted as PV0(2 trk)) tracks requirement (right). The particle level approximation of the PV0(2 trk) cut (“2 cent. part.”) was done by requiring a presence of at least two charged particles with $|\eta| < 2.5$ and $p_T > 150$ MeV. PYTHIA8 ND+SD+DD. Standard dijet selection cuts.

7.7 Irregularities in the rapidity gap spectrum

Figure 7.11 reveals certain detector-related irregularities in the $\Delta\eta^F$ spectrum. They are located around $\Delta\eta^F \sim 1.5$ and $\Delta\eta^F \sim 3.4$.

Noisy FCal Rapidity gap size 1.5 corresponds to the $|\eta_{\text{cluster}}| = 3.3$, that is at the start of the Forward Calorimeter. The TopoCluster noise in this region is larger than in surrounding parts of the calorimeter system and it takes therefore a larger energy deposition to pass the implicit noise suppression cut ($|S_{\text{th}}| > 4$). As a consequence, the original particle needs larger energy to be reconstructed and events thus migrate from smaller to larger $\Delta\eta^F$.

Barel-endcap “crack” region Between the calorimeter barrel and end-cap there is a “crack” region ($1.3 \leq |\eta| \leq 1.6$) where the jet triggers never become fully efficient due to calorimeter inhomogeneities. This crack region also manifests itself in the rapidity gap spectrum and corresponds to the small effect observed at $\Delta\eta^F \sim 3.4$.

Since both of these effects are correctly simulated in our Monte Carlo PYTHIA8 sample, they will be successfully corrected for by the unfolding procedure is discussed in Chapter 9.

7.8 Influence of the Inner Detector

The ID acceptance ($|\eta| < 2.5$) in terms of rapidity gap size is $2.3 < \Delta\eta^F < 7.3$. While the hybrid rapidity gap definition method utilizes TopoClusters above η -dependent significance threshold, tracks are required to comply with specific cleaning cuts and, moreover, by the $p_T > 200$ MeV cut. As already discussed, the E_T -flow study suggests that only those charged particles that have $p > 500$ MeV can reach the calorimeters and be detected. The point where $p_T > 200$ MeV and $p > 500$ MeV become equivalent is $|\eta| < 1.57$. The largest ID influence on the rapidity gap definition is thus expected around $\Delta\eta^F \sim 3.2 - 6.4$. This is confirmed not only by Figure 7.7(b), but also by Table 7.6 where percentages of events with rapidity gap edge defined by track are shown.

Reco $\Delta\eta^F$	0 - 1	1 - 2	2 - 3	3 - 4	4 - 5	5 - 6	6 - 7
PYTHIA8	0%	0%	5%	42%	50%	45%	23%
Data (period B)	0%	0%	5%	40%	50%	44%	—

Table 7.6: The influence of the Inner Detector on the rapidity gap definition evaluated by checking whether it was the TopoCluster or the track that defined the gap-edge.

7.9 The detector level data to MC comparisons

Comparisons between the uncorrected dijet differential cross section as a function of $\Delta\eta^F$ (hybrid method) to the PYTHIA8 MC is shown in Figure 7.12. Small

rapidity gaps are obviously dominated by the ND component, but somewhere around $\Delta\eta^F \sim 2 - 3$ the diffractive cross section component (SD+DD) becomes the major contribution. The same conclusion can be reached from fully corrected distributions (particle level) in Chapter 12. It is therefore obvious that in order to select a diffractive enhanced event sample, a new cut $\Delta\eta^F > 2 - 3$ can be introduced (will be useful for the ξ distribution, for example; see Chapter 8).

The combination of all processes with the ND scaled to match the data in the first bin and SD and DD left unchanged does not provide a sufficient description of the data. The cross sections of these components (ND, SD, DD) can be, however, rescaled to achieve a better description, as will be discussed in Chapter 9.

For the final goal of this analysis, that is the gap survival probability measurement, a Region of Interest (RoI) can be selected by requiring a strong ND suppression (such that the ND is negligible, ideally). Taking into account the detector acceptance for the $\Delta\eta^F$ measurement (discussed above), the RoI is defined as $3 < \Delta\eta^F < 6.5$.

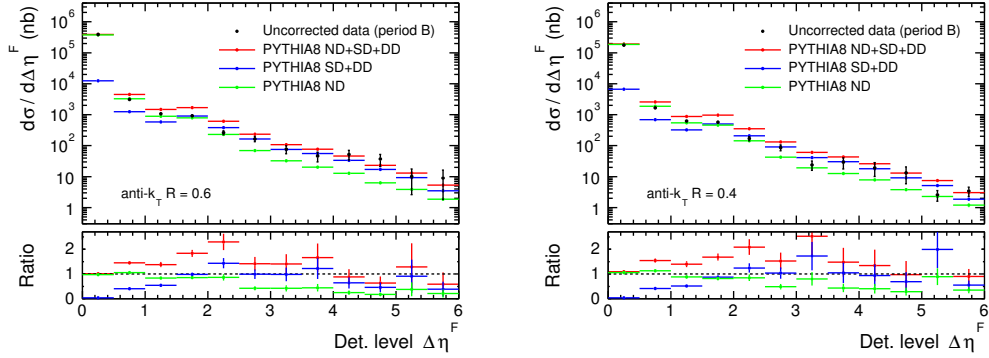


Figure 7.12: Detector level data to PYTHIA8 comparisons for jets reconstructed by the anti- k_T $R = 0.6$ (left) and $R = 0.4$ (right) algorithm. PYTHIA8 ND is scaled to match the data in the first $\Delta\eta^F$ bin. The error bars represent statistical uncertainties.

8. Measurement of ξ

The fractional momentum loss of the scattered proton, denoted generally as ξ (see Equation 1.15), is another variable characteristic for single diffractive events. Though it is not directly observable by the ATLAS experiment as there are no forward detectors with active layers as close to the beam as the typical η of the outgoing proton is, there are ways to approximate it with sufficient precision by detecting particles in the available ATLAS acceptance range. The rapidity gap size and ξ are correlated, as proposed by Equation 1.16 and demonstrated by Figure 8.1, in such a way that large rapidity gaps correspond typically to small ξ values. To enhance the diffractive contribution in the fractional momentum loss spectrum, it is useful to introduce $\Delta\eta^F$ cut, as discussed in Section 7.9. Such ξ measurement is then compared to various SD, DD and ND Monte Carlo models and an attempt to extract S^2 is made (see Chapter 12).

In this chapter, two possible ξ definitions, an effect of the detector noise and detector level data to MC comparisons are presented. Just as in case of $\Delta\eta^F$ measurement, fully corrected differential cross sections are thoroughly discussed in Chapter 12.

Throughout this chapter, all ratio plots are calculated as a colored histogram divided by a black histogram, with error bars representing the overall statistical uncertainty of the ratio.

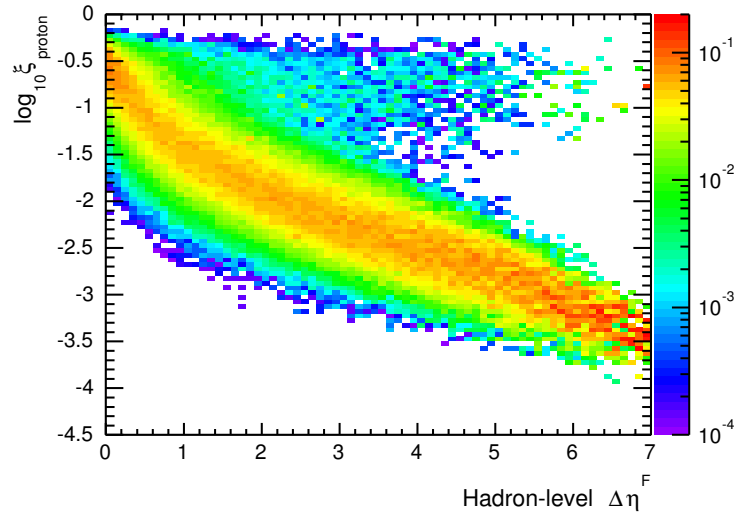


Figure 8.1: Correlation of the ξ value as calculated from momentum of the scattered proton with particle level $\Delta\eta^F$ for PYTHIA8 single diffractive events. Columns normalized to unity.

8.1 Approximation of ξ

While the ATLAS detector system has a very good acceptance in the pseudorapidity region $|\eta| < 4.8$, the very forward region essential for the diffractive events is covered poorly. Not only that the current ATLAS set-up does not allow the direct measurement of scattered diffractive protons, but it can also happen that a significant portion of particles from system X of the $pp \rightarrow Xp$ process escapes detection completely. A direct credible reconstruction of the invariant mass M_X useful for the ξ measurement ($\xi = M_X^2/s$) is thus not possible.

A possible way around this problem with limited detector acceptance is by using an alternative approach for the usual M_X calculation. Such method is not valid in full ξ range, but suppresses the importance of very forward particles for the calculation. Assuming the low Q^2 and t limit and that the emitted pomeron has negligible transverse momentum relative to its longitudinal momentum (travels down the beam pipe), the invariant mass can be approximated as $M_X^2 \simeq 2E_p \cdot \sum E \pm p_z$, where E_p is the energy of the original interacting proton. The sum runs over all final state particles with energy E and longitudinal momentum p_z . Taking the $2E_p$ to be equal to \sqrt{s} , we get

$$\tilde{\xi}^\pm = \frac{M_X^2}{s} \simeq \frac{\sum E \pm p_z}{\sqrt{s}}, \quad (8.1)$$

where $\tilde{\xi}^+$ is used for final state particles with $-\infty < \eta < 4.8$ and $\tilde{\xi}^-$ for final state particles with $-4.8 < \eta < \infty$. If the forward rapidity gap starts at $\eta = -4.8$, the $\tilde{\xi}^-$ is taken as the best approximation of the real ξ while in case of the gap start at $\eta = +4.8$, the $\tilde{\xi}^+$ is used. With this set-up, contributions to $\tilde{\xi}^\pm$ from very forward particles (i.e. p_z carries larger portion of the overall particle energy than p_T) is suppressed. The final $\tilde{\xi}^\pm$ value is thus preferentially influenced by centrally located particles rather than the forward ones.

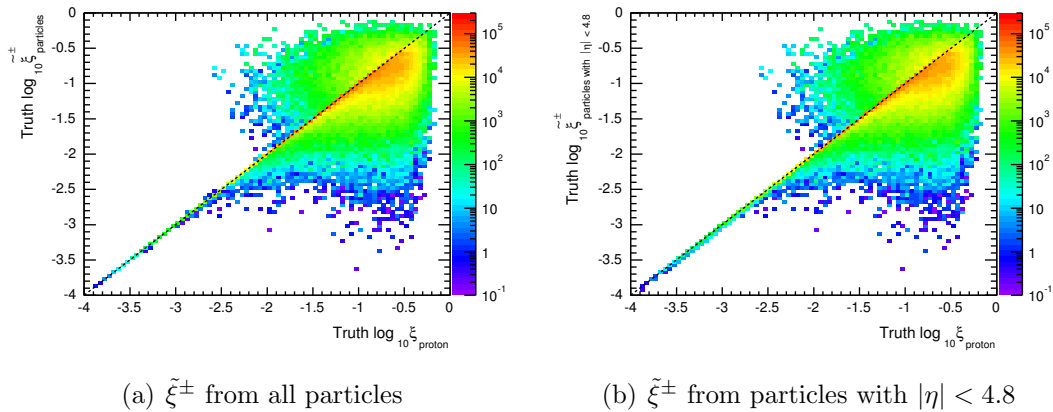


Figure 8.2: Validation of the $\tilde{\xi}^\pm$ calculation method (input: all final state particles) against ξ_{proton} (fractional momentum loss of the scattering proton) for PYTHIA8 SD. (a) $\tilde{\xi}^\pm$ from all particles vs. (b) particles in the calorimeter acceptance vs. ξ as extracted from diffractive proton).

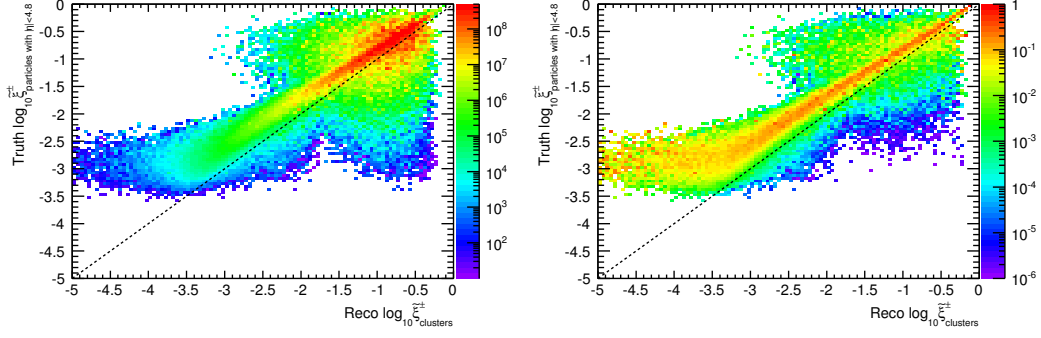


Figure 8.3: Smearing matrix of the $\tilde{\xi}^{\pm}$ variable constructed at reco (truth) level from all clusters (particles) in the calorimeter acceptance region $|\eta| < 4.8$. The right-hand side plot has columns normalized to unity. PYTHIA8 ND+SD+DD.

In the region of low ξ , the $\tilde{\xi}^{\pm}$ variable defined by Equation 8.1 is a good approximation of the actual ξ for SD events, as demonstrated in Figure 8.2(a), for $\log_{10}\xi < -1.5$ ($\xi < 0.032$). As there is a non-perfect detector acceptance, we can actually define detector level $\tilde{\xi}^{\pm}$ only for TopoClusters in the region $|\eta| < 4.8$. The matching particle level definition, i.e. all final state particles with $|\eta| < 4.8$, is validated in Figure 8.2(b). Even with this limitation given by the detector acceptance, the particle level $\tilde{\xi}^{\pm}$ is within 2% from the actual ξ , confirming thus that very forward particles do not play a significant role for the low- ξ region approximation by Equation 8.1.

The correlation plot (smearing matrix) between the detector and particle level $\tilde{\xi}^{\pm}$ is presented in Figure 8.3, in which the reco $\tilde{\xi}^{\pm}$ is calculated from all reconstructed TopoClusters within $|\eta| < 4.8$ with the assumption that every negative energy noise cluster used in the calculation will statistically cancel similar positive noise contributions. In the right-hand side plot, columns are normalized to unity, which means that each bin of the smearing matrix gives a probability that the measured $\tilde{\xi}^{\pm}$ value corresponds to the given particle level value. This plotting style also allows to observe the clear correlation across the full range, which is impossible from the left-hand side plot due to the steeply falling cross section. A strong reco-truth correlation is observed through most of the $\tilde{\xi}^{\pm}$ range with the exception of very low $\tilde{\xi}^{\pm}$, where events with truth $\log_{10}\tilde{\xi}^{\pm} \sim -3$ are reconstructed as having $\log_{10}\tilde{\xi}^{\pm}$ down to -5. This loss of correlation is disturbing and, as we shall see later on, it is a consequence of the remaining cluster noise.

There is one distinctive difference between the smearing matrix of the $\Delta\eta^F$ distribution and the one of ξ , and it is the non-diagonality. The fact that detector level $\tilde{\xi}^{\pm}$ tends to be systematically smaller than the particle level one is caused by energy losses from particles falling out of the detector acceptance, not reaching the calorimeters (or ending up in dead regions) or losing most of their energy traversing the inner detector. Based on the truth-reco comparison, it would be possible to correct for these detection inefficiencies by ξ -dependent factors. They can be, however, omitted as the unfolding procedure (see Chapter 9) will correct for this effect.

There is an alternative ξ approximation definition, which is mathematically similar to Equation 8.1 but equivalent only in case of zero-mass objects (TopoClusters, particles):

$$\tilde{\xi}^{\pm} = \sum_{i_{\text{objects}}} \frac{p_{T,i} \cdot e^{\pm y_i}}{\sqrt{s}}. \quad (8.2)$$

The sum runs over all objects and adds together the transverse momenta multiplied by the exponential of the rapidity. This $\tilde{\xi}^{\pm}$ definition is henceforth known as the “ p_T -method”. If the forward rapidity gap starts at $\eta = -4.8$ then the sum takes the negative sign in the exponential function, while the positive sign is chosen for gaps starting at $\eta = +4.8$. The benefit of this calculation is, similarly as in case of the $E \pm p_Z$ method, that the significance of particles in the X system traveling in the very forward directions (large rapidities) is exponentially suppressed in the $\tilde{\xi}^{\pm}$ calculation.

It is assumed again that a cluster noise-cancellation takes place due to the noise being Gaussian symmetric around zero. A validation plot is at the left-hand side of the Figure 8.4. It manifests, just as in case of the $E \pm p_Z$ method, a very good diagonal behavior in the range of $\log_{10} \xi < -1.5$. The particle level correlation between the two methods is depicted at the right-hand side of the same figure, showing that they are indeed consistent.

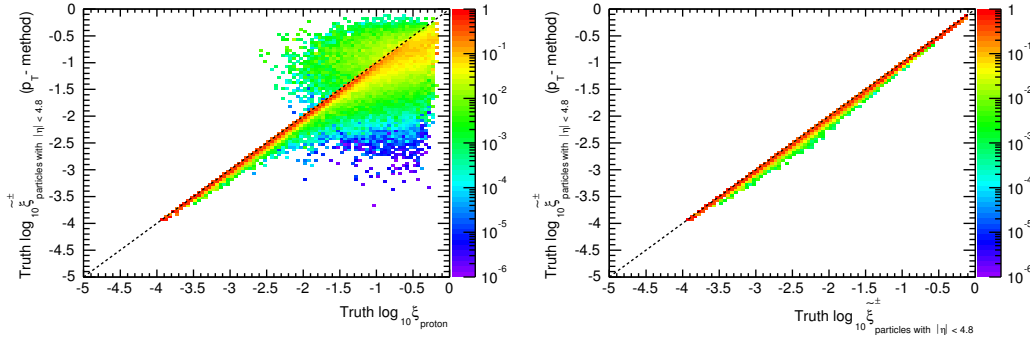


Figure 8.4: Validation of $\tilde{\xi}^{\pm}$ (p_T method) as calculated from particles in the ATLAS acceptance ($|\eta| < 4.8$) (left) and p_T vs. $E \pm p_Z$ method comparison (right). Columns normalized to unity, PYTHIA8 SD.

An important observation can be made from the smearing matrix for the p_T method in Figure 8.5(a). The large non-correlated tail in the small- $\tilde{\xi}^{\pm}$ region as seen in Figure 8.3 disappeared. Another way to see this is through the correlation plot between both detector level $\tilde{\xi}^{\pm}$ definitions in Figure 8.5(b). While both definitions give, in the region of larger reco- $\tilde{\xi}^{\pm}$, the same results, the smearing matrix at small $\tilde{\xi}^{\pm}$ is significantly improved. Figure 8.6(a) demonstrates the effect of the cell significance cut of the $E \pm p_Z$ method. It is obvious that the problematic small $\tilde{\xi}^{\pm}$ region is strongly affected by calorimeter noise and therefore the noise-cancellation assumption (when summing over all clusters in the event) does not

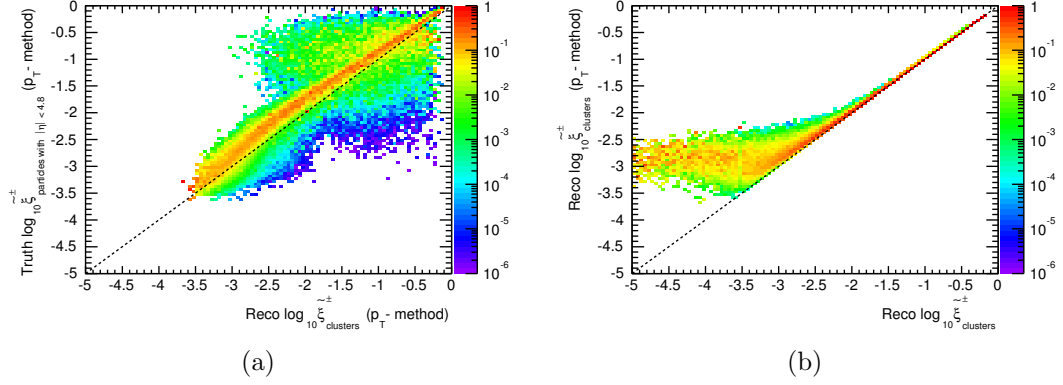


Figure 8.5: (a) Smearing matrix of the ξ^\pm variable (p_T method) constructed at reco (truth) level from all clusters (particles) in the calorimeter acceptance region $|\eta| < 4.8$. (b) Detector level correlation plot between the p_T method (y axis) and $E \pm p_z$ method (x axis). PYTHIA8 ND+SD+DD.

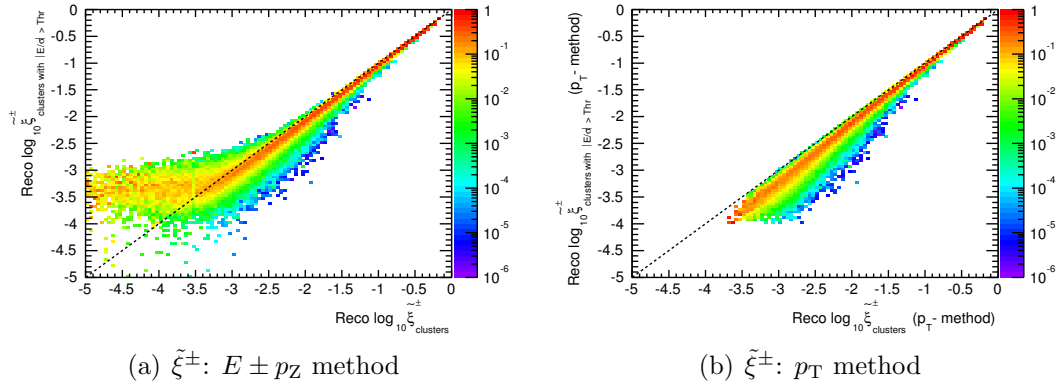


Figure 8.6: Influence of an employment of the cell significance cut: (a) $E \pm p_z$ method (clusters complying with the cell significance cut vs. all clusters), (b) the same for the p_T method. Columns normalized to unity. PYTHIA8 SD.

hold. It can be explained by the way the cluster momentum vector is calculated. In case of a noisy cluster, the part of the Equation 8.1 corresponding to energy can flip a sign from positive to negative and vice versa. However, the sign of the p_z is never changed which in turn results in a failure of the noise-cancellation assumption. Therefore, the $E \pm p_z$ method can be used only after well tuned noise removal procedure.

As discussed in previous paragraph, the p_T method of ξ^\pm calculation in the large- ξ^\pm region behaves similarly to the $E \pm p_z$ method, while the low- ξ^\pm tail does not manifest a sensitivity to the noise anymore. This is given by the fact that when the noisy cluster has a negative energy, even the p_T is provided as a negative value and so the noise-cancellation assumption (summing over all clusters across the calorimeter) can hold. A correlation plot between ξ^\pm calculated from all clusters and ξ^\pm calculated from clusters above cell significance threshold cuts (introduced

in Chapter 7) is shown in Figure 8.6(b). The only result is that $\tilde{\xi}^\pm$ gets lower but the shape is unchanged. The p_T method can thus be used without additional noise-suppression cuts.

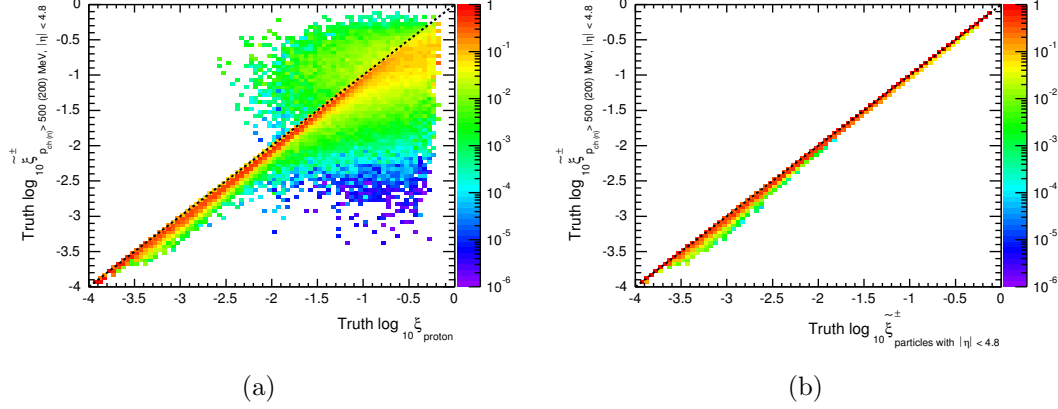


Figure 8.7: (a) Validation of the $\tilde{\xi}^\pm$ calculation method (particles with $p_{\text{charged (neutral)}} > 500 \text{ (200) MeV}$ vs. ξ as extracted from diffractive proton). (b) A particle level difference between the $\tilde{\xi}^\pm$ as calculated from all particles within $|\eta| < 4.8$ (horizontal axis) and particles with additional $p_{\text{charged (neutral)}} > 500 \text{ (200) MeV}$ cuts. PYTHIA8 SD, columns normalized to unity.

The final adjustment of the $\tilde{\xi}^\pm$ calculation follows the one made for the $\Delta\eta^F$ definition as well. It reflects findings of the E_T -flow analysis, that is requiring particles with $p_{\text{charged (neutral)}} > 500 \text{ (200) MeV}$ (particles with lower momenta cannot be detected). This particle level difference is validated in Figure 8.7, the truth $\tilde{\xi}^\pm$ correlation between all particles in acceptance and particles above momentum cuts is also shown. The biggest change is observed at low $\tilde{\xi}^\pm$ while for larger values the difference is minimal. The detector sensitivity to low-energy particles is thus crucial for low- $\tilde{\xi}^\pm$ region.

However, the $\tilde{\xi}^\pm$ validation plot in Figure 8.7(a) is far from the almost perfectly diagonal plot as in Figure 8.2. This effect can be better evaluated by plotting the ratio of $\tilde{\xi}^\pm$ and ξ_{proton} in different $\tilde{\xi}^\pm$ bins, as is presented in Figure 8.8. It is clear that in the region of interest ($\log_{10}\tilde{\xi}^\pm < -2.5$, as is discussed in Chapter 12) the effect or non-diagonality is well within 4-5%.

Final smearing matrices for $\tilde{\xi}^\pm$ measurement are depicted in Figure 8.9. The detector level reconstruction is done by the p_T method from all TopoClusters within $|\eta| < 4.8$, while the particle level definition takes advantage of final state particles with momentum cuts $p_{\text{ch (n)}} > 500 \text{ (200) MeV}$ and within $|\eta| < 4.8$. These are the final definitions used for the $\tilde{\xi}^\pm$ measurement.

Finally, Figure 8.10 presents $\tilde{\xi}^\pm$ resolutions (p_T method) fitted by Gaussian function in different $\log_{10}\tilde{\xi}^\pm$ ranges. Contrary to the $\Delta\eta^F$ resolutions, the $\tilde{\xi}^\pm$ variable reveals an expected Gaussian shape. One can also notice a clear evolution of

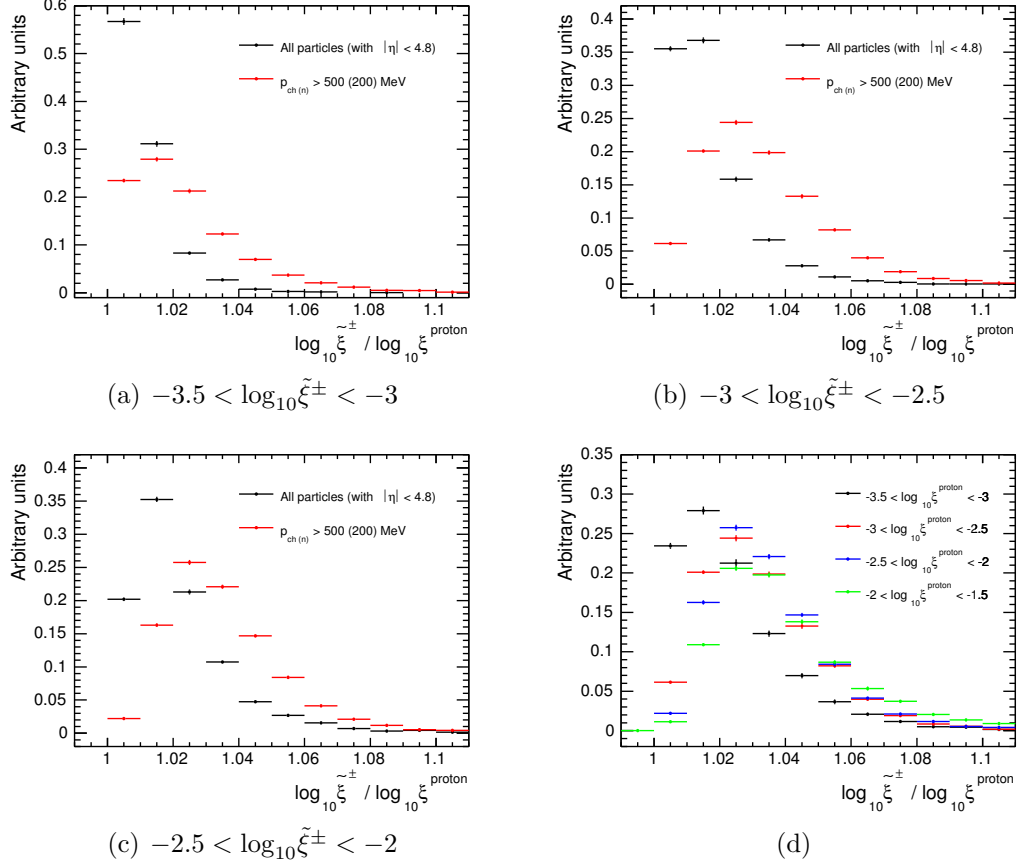


Figure 8.8: (a-c) Ratios of particle level $\tilde{\xi}^{\pm}$ (p_T method) and ξ_{proton} in different $\tilde{\xi}^{\pm}$ bins and with or without $p_{\text{charged (neutral)}} > 500$ (200) MeV cuts. (d) Different $\tilde{\xi}^{\pm}$ bins for p_T approximation method and with $p_{\text{charged (neutral)}} > 500$ (200) MeV cuts. Distributions normalized to unity. PYTHIA8 SD. The error bars represent statistical uncertainties.

standard deviations from small values at the large ξ region (typically around 7 %) up to 14% at the small $\tilde{\xi}^{\pm}$ tail. The worse resolution for small $\tilde{\xi}^{\pm}$ is to be expected due to the bigger influence of low energy particles (many of them undetectable due to the limited calorimeter sensitivity).

8.2 ξ acceptance

Just as in case of $\Delta\eta^F$, the detector acceptance for $\tilde{\xi}^{\pm}$ measurement can be studied by truth-reco comparisons as plotted in Figure 8.11. The detector level $\tilde{\xi}^{\pm}$ spectrum is, again, dependent on the PV0 cut only in the very tail ($\tilde{\xi}^{\pm} < 0.003$), but contrary to $\Delta\eta^F$ this dependence is smaller. The truth-reco comparison reveals that the acceptance is in the range $-3.4 < \log_{10}\tilde{\xi}^{\pm} < -0.3$. Outside this range, the reco $\tilde{\xi}^{\pm}$ gets significantly suppressed with respect to the particle level distribution (by more than factor two), i.e. the measurement would not be reliable as the unfolding procedure would have to introduce very large Monte Carlo

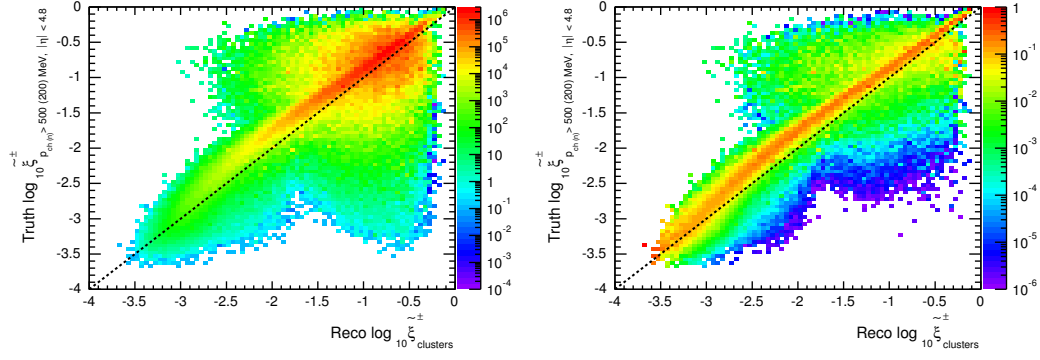


Figure 8.9: Smearing matrix of the ξ^\pm variable (p_T method) constructed at reco (truth) level from all clusters (particles with p_{charged} (neutral) > 500 (200)) in the calorimeter acceptance region $|\eta| < 4.8$. The right-hand side plot has columns normalized to unity. PYTHIA8 ND+SD+DD.

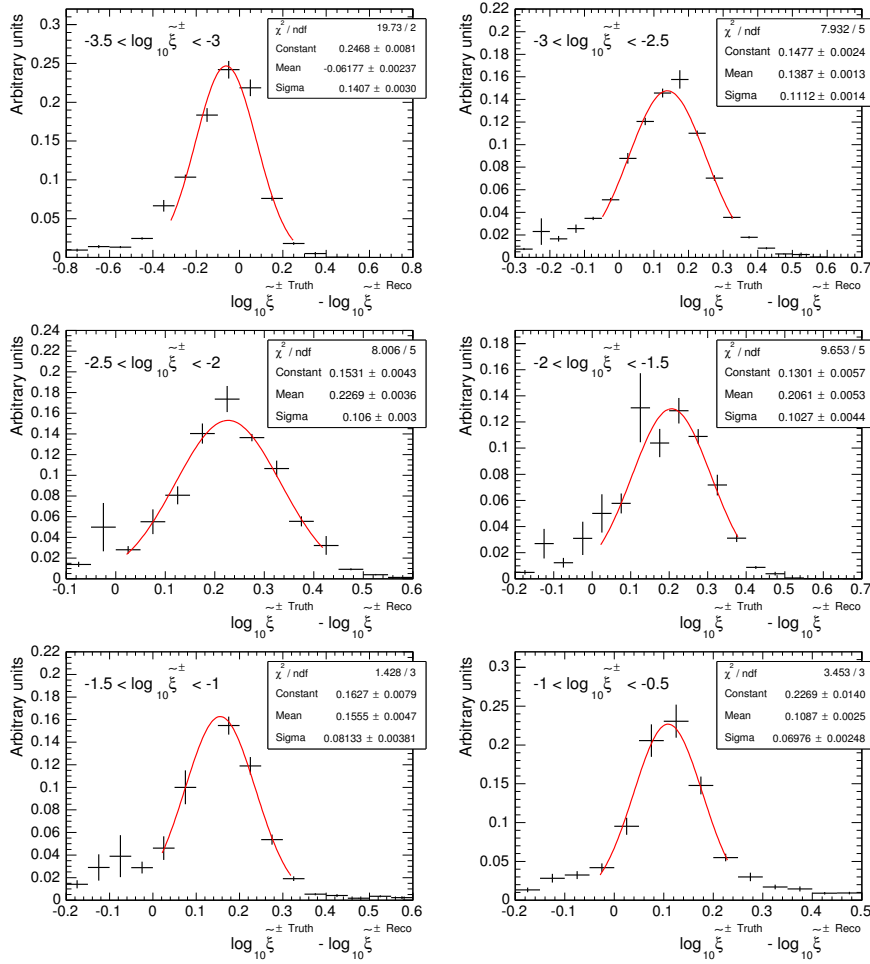


Figure 8.10: Resolutions of the ξ^\pm variable (p_T method). PYTHIA8 ND+SD+DD. The error bars represent statistical uncertainties. The error bars represent statistical uncertainties.

derived correction factors.

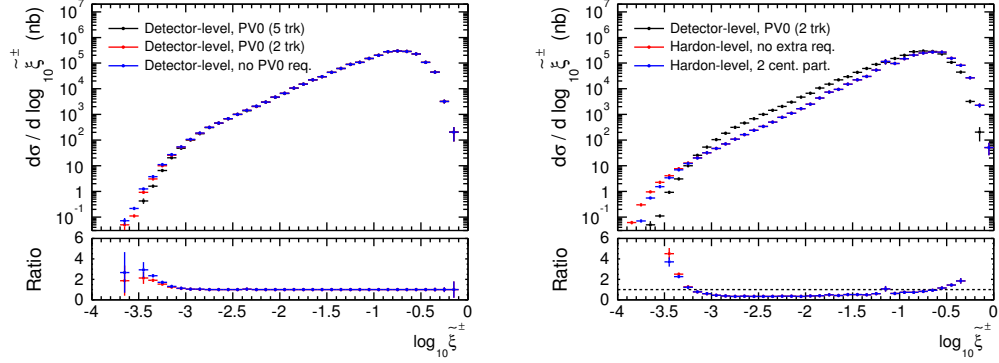


Figure 8.11: Influence of the different versions of the primary vertex cut on the detector level ξ^\pm distribution (left) and reco-truth comparisons for the primary vertex cut with at least two associated (denoted as PV0(2 trk)) tracks requirement (right). The particle level approximation of the PV0(2 trk) cut (“2 cent. part.”) was done by requiring a presence of at least two charged particles with $|\eta| < 2.5$ and $p_T > 150$ MeV. The error bars represent statistical uncertainties.

8.3 The detector level Data vs. Monte Carlo comparisons

The detector level data to MC comparisons are presented in Figure 8.12 for events with jets reconstructed using the anti- k_T $R = 0.6$ and $R = 0.4$ algorithms. The region of large ξ^\pm is dominated by the ND contribution while events with $\log_{10} \xi^\pm < -2.5$ mostly diffractive events with ND suppressed by factor three or more. Even stronger suppression can be gained by adding the $\Delta\eta^F > 3$ requirement, as discussed in Section 7.9. Such ξ^\pm distribution is shown in Figure 8.13. While the effect on the lowest $\log_{10} \xi^\pm$ data bin is minimal, the ND Monte Carlo component gets suppressed to the level of $\sim 10\%$ compared to the data. Moreover - as expected from the anti-correlation between ξ and rapidity gap size - the ξ^\pm distribution with the $\Delta\eta^F > 3$ cut is steeply falling off with increasing ξ^\pm . The ND becomes again the major contribution in the range $\xi^\pm > 0.01$.

For the purpose of retrieving the soft survival probability S^2 , a Region of Interest (RoI) can be selected by requiring a strong ND suppression. From the discussion above (and taking into account the detection acceptance for the ξ^\pm measurement) it is obvious that the RoI in terms of the fractional momentum loss of the scattered proton is $-3.4 < \log_{10} \xi^\pm < -2.5$.

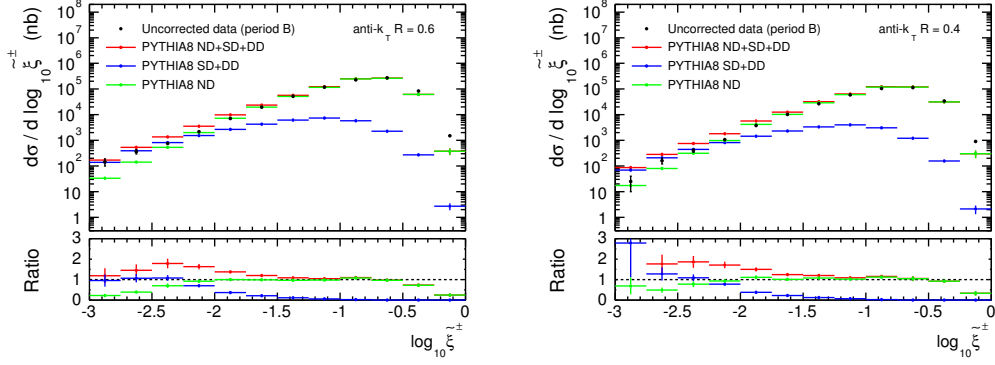


Figure 8.12: Detector level data to PYTHIA8 comparisons for jets reconstructed by the anti- k_T $R = 0.6$ (left) and $R = 0.4$ (right) algorithm. PYTHIA8 ND is scaled to match the data in the first $\Delta\eta^F$ bin. The error bars represent statistical uncertainties.

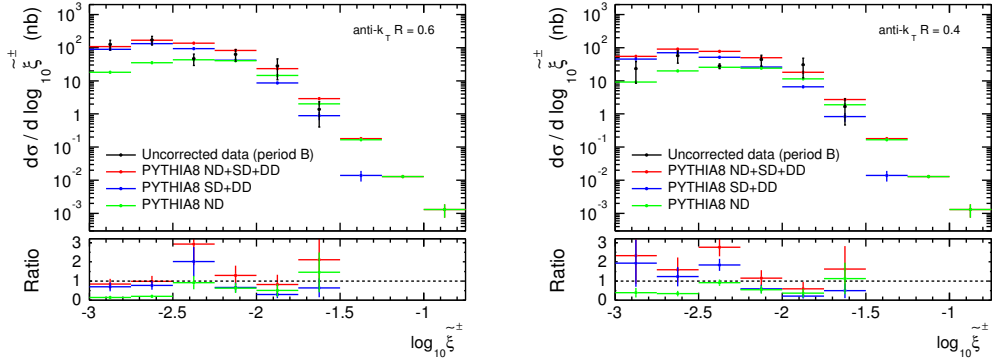


Figure 8.13: Detector level data to PYTHIA8 comparisons with $\Delta\eta^F > 3$ cut for jets reconstructed by the anti- k_T $R = 0.6$ (left) and $R = 0.4$ (right) algorithm. PYTHIA8 ND is scaled to match the data in the first $\Delta\eta^F$ bin. The error bars represent statistical uncertainties.

9. Unfolding

Each experimental measurement of a physics quantity such as jet p_T , η or diffractive variables $\Delta\eta^F$ and ξ^\pm is influenced by various detector effects. They can significantly affect the measured cross section via introducing systematic biases and smearings of the measured distributions, arising primarily from reconstruction inefficiencies and limited resolutions. Various techniques, generally called “unfolding”, have been developed to correct for these effects: from simple ones such as the bin-by-bin method (correcting data by $N_{\text{Truth}}/N_{\text{Reco}}$ factors, where N_{Truth} is the number of generated and N_{Reco} the number of reconstructed events in a given bin) up to complex ones such as the Iterative, Dynamically Stabilized (IDS) method [50].

The unfolding method adopted in this analysis is the IDS. It requires as an input a so-called response matrix (known also as a smearing matrix) constructed from Monte Carlo with full ATLAS detector simulation, which is in fact a correlation matrix between hadron and detector level definition of given measured quantity. Unlike in the simple bin-by-bin method, the IDS unfolding is able to take into account migrations between bins, fakes (events passing reco level cuts only) and misses (events passing truth level cuts only).

Throughout this chapter, all ratio plots are calculated as a colored histogram divided by a black histogram, with error bars representing the overall statistical uncertainty of the ratio.

9.1 1D unfolding

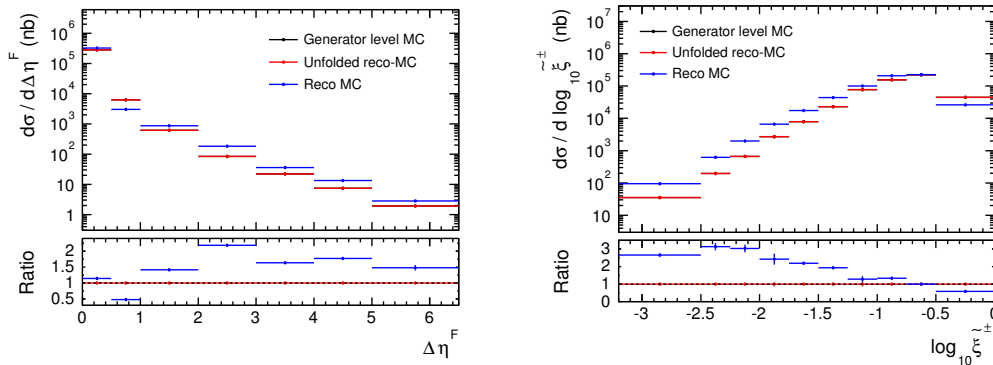


Figure 9.1: Closure test (unfolding the detector level PYTHIA8) of the 1D unfolding procedure (1 iteration). Jets reconstructed with the anti- $k_T R = 0.6$ algorithm.

The 1D IDS unfolding method takes as an input two independent Monte Carlo histograms: the truth distribution made of events passing particle level selection cuts and the reco distributions made of events passing detector level selection cuts. The truth distribution thus contains misses (events complying with truth

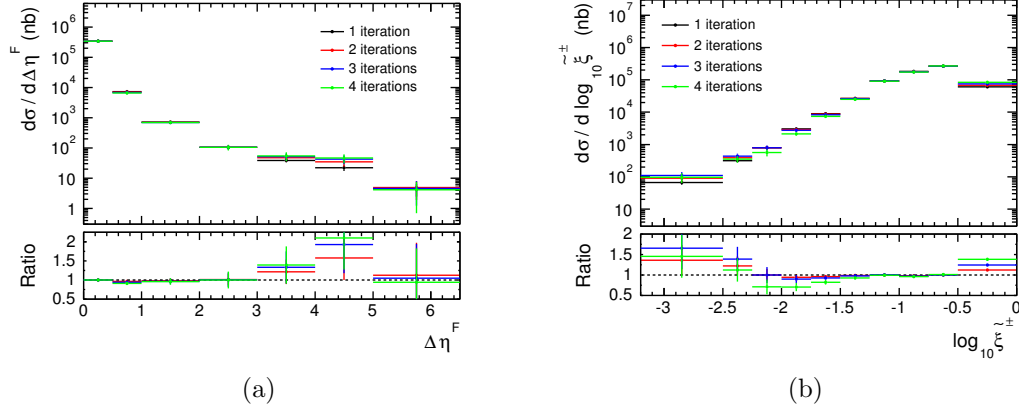


Figure 9.2: The influence of number of iterations on $\Delta\eta^F$ and $\tilde{\xi}^\pm$ distributions. The ratios are calculated with respect to the first iteration and jets are reconstructed with the anti- $k_T R = 0.6$ algorithm.

but not the reco selection) and the reco distributions contains fakes (events complying with reco but not truth selection). The response matrix is a 2D histogram with a correlation of the particle level and detector level quantity ($\Delta\eta^F$, $\tilde{\xi}^\pm$) made of events passing both hadron and detector level selection cuts (i.e. fakes and misses are not included), see Figures 7.8 and 8.9. The measured distribution is provided as a simple 1D histogram.

A way to test that the unfolding works well is via supplying it with the detector level MC in place of the measured data distribution (so-called “closure test”). The result of the unfolding should perfectly match the particle level MC already after one iteration, as demonstrated in Figure 9.1 for both $\Delta\eta^F$ and $\tilde{\xi}^\pm$ distributions. We can also notice that the correction factors that had to be applied to make the reco MC match the truth MC (blue ratio plots) are between 0.5 - 3, which are actually the inversed correction factors of the bin-by-bin unfolding method.

Figure 9.2 presents unfolded distributions for different number of iterations. It should be noted that the choice of this unfolding parameter is important, but it seems that the change in final cross section is small from around 3-4 iterations. The decision about the number of iterations is carefully studied in next section where the 2D unfolding is discussed.

9.2 2D unfolding

For the final results, i.e. the dijet cross section as a function of $\Delta\eta^F$ and $\tilde{\xi}^\pm$, a two-dimensional iterative IDS unfolding procedure was adopted. It is necessary to account for migrations with both the exponential fall of the jet p_T spectrum and with the exponential fall at larger $\Delta\eta^F$ (smaller $\tilde{\xi}^\pm$). The effect of p_T migrations is investigated in Figure 9.3 via plotting the particle level p_T of the leading

and sub-leading jet for events passing detector level cut selection (i.e. at least two jets are required at both particle and detector level). For the right-hand side figure (reco $p_T^{\text{jet1 (jet2)}} > 30$ (20) GeV), the migration effect is evaluated to 5.9 % by comparing the contribution of the area with truth $p_T^{\text{jet1 (jet2)}} < 30$ (20) GeV to the overall cross-section. Similarly, the symmetrical $p_T^{\text{jet1 (jet2)}} > 20$ (20) GeV cuts lead to 5.8 % of migrations from low- p_T ranges.

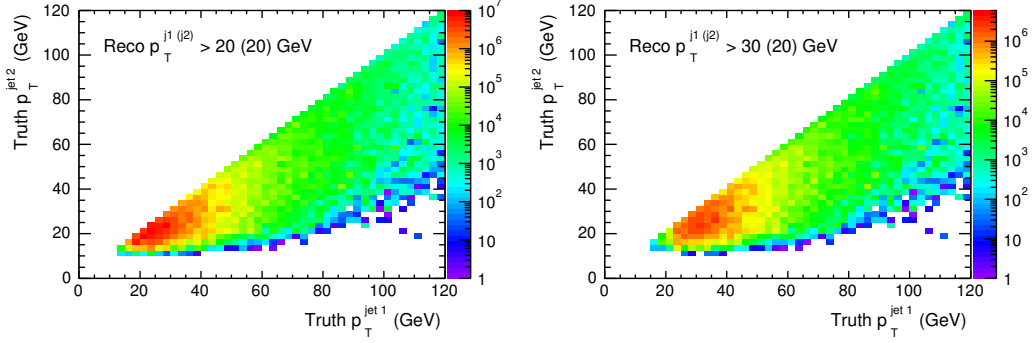


Figure 9.3: The effect of migrations from low- p_T particle level range to the whole detector level range. Particle level p_T of the sub-leading vs. leading jet after passing detector level selection cuts are plotted. Left: Detector level cuts $p_T^{\text{j1(j2)}} > 20$ (20) GeV. Right: Detector level cuts $p_T^{\text{j1(j2)}} > 30$ (20) GeV. PYTHIA8 ND+SD+DD.

Figure 9.4 demonstrates the need for 2D unfolding by plotting the detector level $\Delta\eta^F$ for different ranges of the particle level leading jet p_T . The most important observation is that the gap distribution shape is dependent on the jet p_T , as expected from the relation between the size of the rapidity gap and the invariant mass of the diffractive system X. Smaller jet p_T tends to contribute more to the large $\Delta\eta^F$ than to the small $\Delta\eta^F$. We can see that the 20-25 GeV range accounts for about 45 % of the total $\Delta\eta^F$ distribution at gap sizes 6 - 7 while for 25 % only at $\Delta\eta^F = 0 - 1$. The 2D unfolding thus provides an important tool to account for the p_T migrations and the p_T dependence of the $\Delta\eta^F$ (or $\tilde{\xi}^\pm$ alternatively).

The 2D unfolding procedure is very similar to the 1D unfolding, except that instead of 1D input histograms, 2D distributions have to be provided. Distributions of interest ($\Delta\eta^F$ and $\tilde{\xi}^\pm$) are plotted as 2D histograms with respect to the leading jet p_T . Just in case of one dimension, inputs are the particle level and detector level distributions (i.e. including fakes and misses) and the response matrix, which contains events that pass both particle and detector level selection. All these spectra are provided in such a way the axes have the chosen p_T and $\Delta\eta^F$ ($\tilde{\xi}^\pm$ alternatively) bins merged together by chaining $n_{\text{meas.}}$ bins in $\Delta\eta^F$ ($\tilde{\xi}^\pm$) in different p_T ranges, so there are $n_{\text{meas.}}$ bins for lowest p_T bin followed by another $n_{\text{meas.}}$ bins for second-lowest p_T bin etc. The unfolded spectrum has, naturally, the same binning. To obtain final fully-corrected spectra, the $\Delta\eta^F$ ($\tilde{\xi}^\pm$) distributions in different p_T ranges are summed together. The example is provided in Figure 9.5 for transfer matrices of both $\Delta\eta^F$ and $\tilde{\xi}^\pm$, along with their

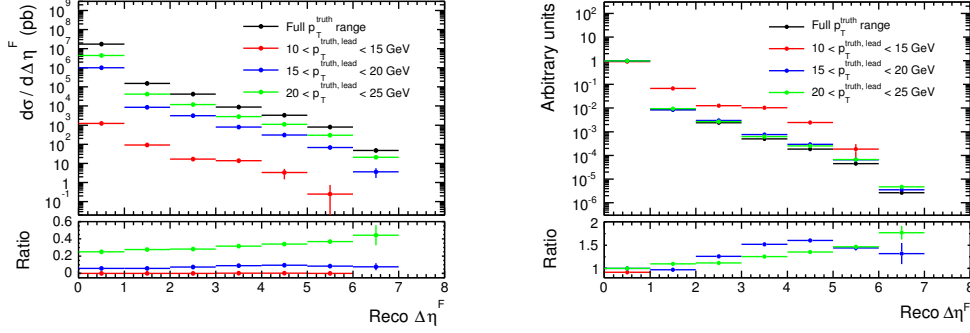


Figure 9.4: Detector level $\Delta\eta^F$ distribution for different ranges of generator level leading jet p_T scaled to cross section (left) and to unity (right). Detector level $p_T^{\text{jet1 (jet2)}} > 20$ (20) GeV cuts applied. PYTHIA8 ND+SD+DD.

1D projections to the x and y axis.

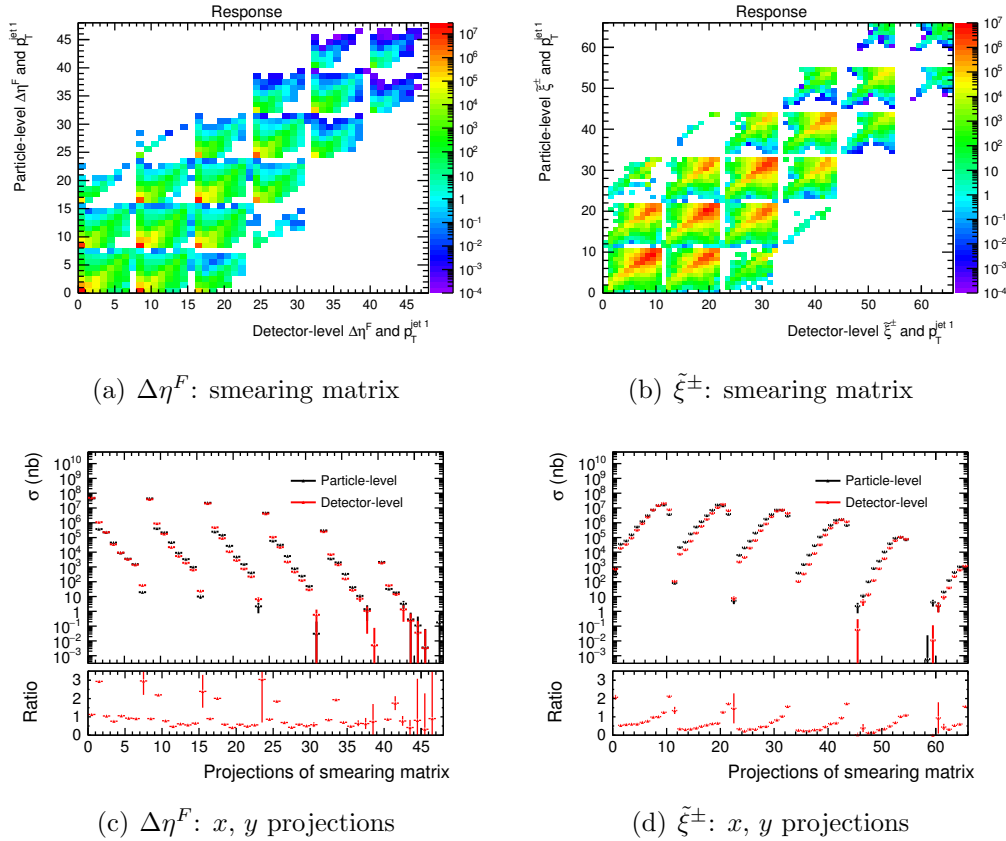


Figure 9.5: Monte Carlo inputs to the unfolding procedure. Smearing matrices are in figure a) and b), their projections to x and y axes are in c) and d). Binning in these plots corresponds to merged bins in jet p_T and $\Delta\eta^F$ ($\tilde{\xi}^\pm$). PYTHIA8 ND+SD+DD, anti- $k_T R = 0.6$ jets.

Figure 9.6 presents graphically four possible classes of events entering the unfolding procedure via Pythia8 samples: true events passed (passed both reco

and truth level cuts), true events failed (neither reco nor truth level cuts passed), fakes and misses. The share of fakes (misses) in reconstructed (truth) events is found to be 20% (29% respectively).

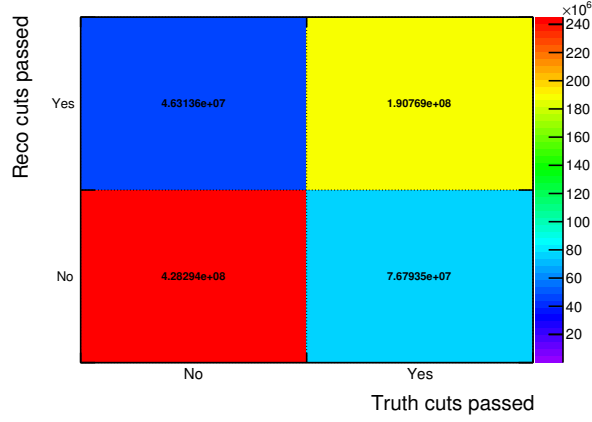


Figure 9.6: Graphical representation of the amount of fakes and misses entering the unfolding procedure. PYTHIA8 ND+SD+DD samples scaled to cross section.

9.2.1 Choice of bins

The appropriate choice of bins for the unfolding procedure relies on two factors. First, the resolution in given variable should be respected (bin-widths should not be much smaller). Second, a sufficient statistics in bins of interest has to be ensured to avoid statistical fluctuations influencing the resulting unfolded spectrum in a negative way. The combination of these two factors provides a key guideline for an appropriate choice of the binning.

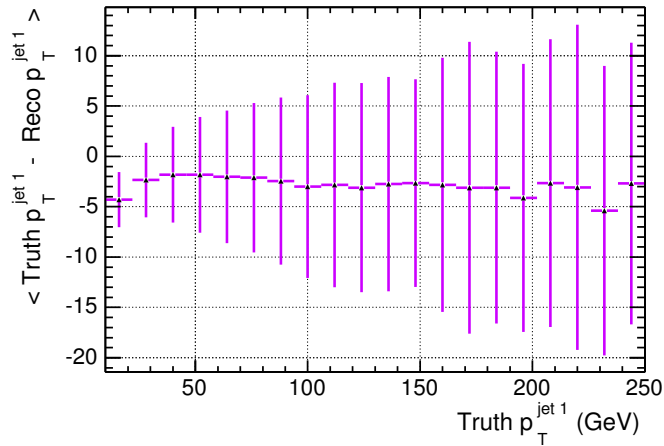


Figure 9.7: Mean truth - reco values of the leading jet p_T with error bars set to the standard deviation divided by the square-root of the number of events in the bin (resolution).

Resolutions of the variables of interest, $\Delta\eta^F$ and $\tilde{\xi}^\pm$, have been presented in chapters 7 and 8, namely in Figures 7.9 and 8.10. The resolution in leading jet p_T is shown in Figure 9.7. Combining this information with the requirement on the adequate statistics (which is, in the end, the major limitation) results in the choice of bins as presented in the Table 9.1. Overview of the raw number of events for these bins is shown in Figure 9.8.

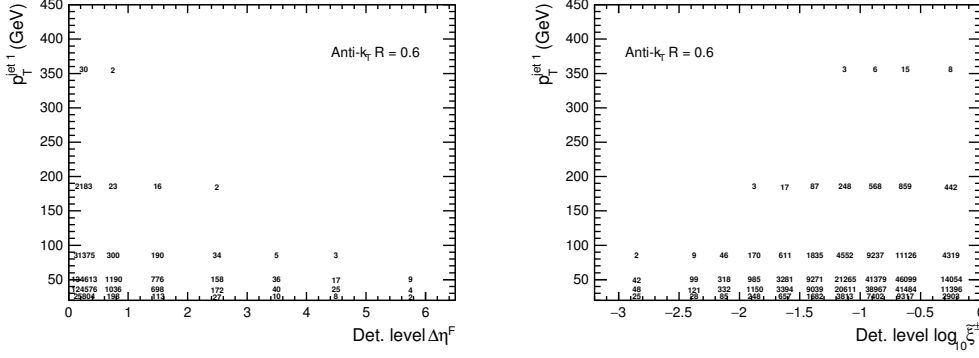


Figure 9.8: Numbers of raw events in the detector level histograms for the period B data sample. Jet reconstructed by the anti- k_T $R = 0.6$ algorithm.

Variable	Number of bins	Bins
$\Delta\eta^F$	8	0, 0.5, 1, 2, 3, 4, 5, 6.5, 10
$\log_{10} \tilde{\xi}^\pm$	11	-5, -3.2, -2.5, -2.25, -2, -1.75, -1.5, -1.25, -1, -0.75, -0.5, 0
$^1)p_T$ (GeV)	6	20, 30, 40, 60, 110, 260, 450
$^2)p_T$ (GeV)	6	20, 30, 40, 50, 60, 120, 450

Table 9.1: Bins in different variables used for unfolding. $^1)$ refers to binning used for inclusive $\tilde{\xi}^\pm$ and $\Delta\eta^F$ spectra while $^2)$ is used for $\tilde{\xi}^\pm$ with $\Delta\eta^F > 2$ cut.

9.2.2 Monte Carlo scaling for the use in the unfolding

The Monte Carlo used for the unfolding procedure should be successful in describing the shape of the detector level distribution in data. This can be achieved by a proper combination of the non-diffractive, single diffractive and double diffractive components of our PYTHIA8 samples. The best combination was found by minimizing the difference between the spectrum of interest ($\Delta\eta^F$ or $\tilde{\xi}^\pm$) in data and in the Monte Carlo.

- $\Delta\eta^F$ distribution: $\text{ND} \cdot 0.623 + (\text{SD} + \text{DD}) \cdot 0.206$
- $\tilde{\xi}^\pm$ distribution: $\text{ND} \cdot 0.577 + (\text{SD} + \text{DD}) \cdot 0.283$

The effect of these fits is shown in Figure 9.9.

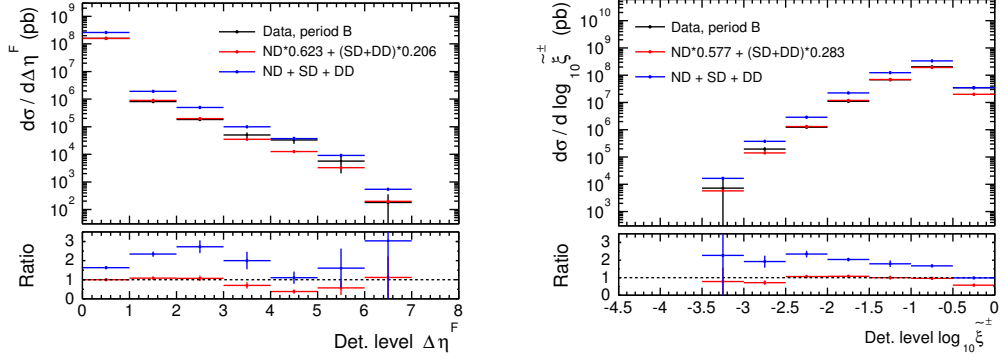


Figure 9.9: The detector level comparisons between data and PYTHIA8. The effect of the Monte Carlo scaling to the data shapes is demonstrated.

9.2.3 Unfolding tests

The unfolding, especially its 2D version, is a complex procedure which has to be thoroughly tested before it can be relied upon. These tests are also important for answering question what is the optimal value of the regularisation parameter (specifying the number of iterations). They are summarized in next paragraphs and are as follows:

- Closure test: reproducing the particle level Monte Carlo by unfolding the detector level distribution
- Convergence test of higher iterations
- Stability checks against the choice of binnings

Closure test The simplest test of the unfolding performance is to substitute the data-to-unfold distribution by the detector level Monte Carlo. If the unfolding is implemented correctly, the result should be the exact particle level MC distribution already after the first iteration. This is confirmed by Figure 9.10.

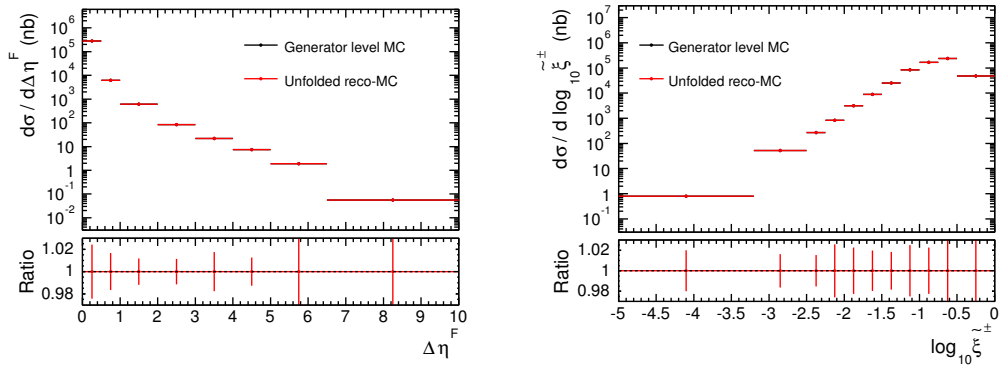


Figure 9.10: Closure test (unfolding the detector level PYTHIA8) of the 2D unfolding procedure (1 iteration).

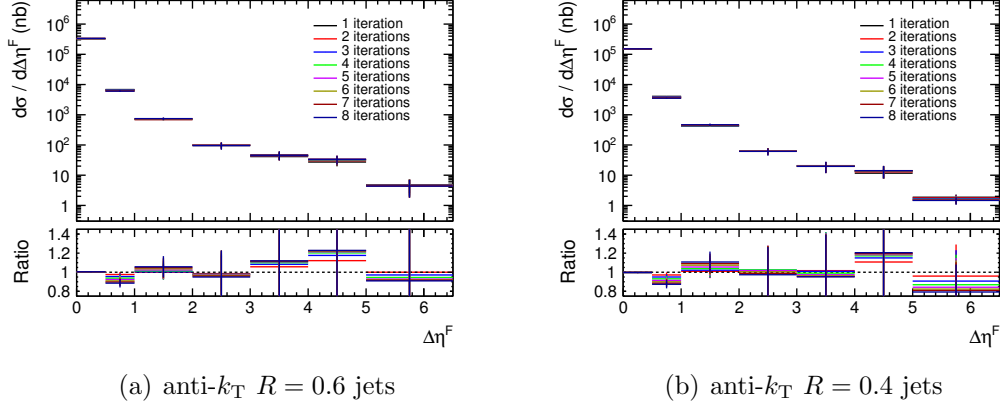


Figure 9.11: The influence of number of iterations on the $\Delta\eta^F$ distribution. The ratios are calculated with respect to the first iteration.

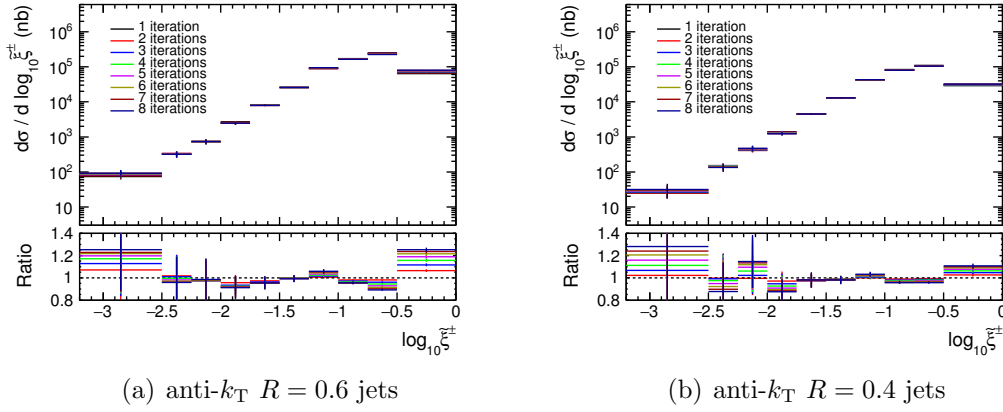


Figure 9.12: The influence of number of iterations on the $\tilde{\xi}^\pm$ distribution. The ratios are calculated with respect to the first iteration.

Convergence of higher iterations The important parameter of the unfolding procedure is the number of iterations. Figure 9.11 demonstrates the influence of higher iterations for unfolding of the rapidity gap distribution, while Figure 9.12 presents the same for $\tilde{\xi}^\pm$ variable (ratios calculated with respect to the first iteration). Both these distributions are obviously sensitive to the choice of this parameter in bins with lower statistics, that is the small $\tilde{\xi}^\pm$ (large gap) region, and demonstrate a clear convergence behaviour. That can be also quantified by calculating the χ^2 of neighboring iterations as

$$\chi^2(i^{\text{th}} \text{ iter.}) = \sum_j^{N_{\text{bins}}} \frac{(y_{i,j} - y_{i-1,j})^2}{\epsilon_{i,j}^2 + \epsilon_{i-1,j}^2} \quad (9.1)$$

where y is the variable under investigation and ϵ is its statistical error. As the χ^2 is sensitive to the number of events occupying the investigated bins as well as the absolute values of the investigated variable, its value is dependent on the choice of bins of interest. Therefore, tables 9.2 and 9.3 present χ^2 in different

ranges.

Iterations	χ^2 (full range)	χ^2 ($2 < \Delta\eta^F < 6.5$)	r_{dist}
1 - 2	0.99	0.115	12 %
2 - 3	0.42	0.021	5 %
3 - 4	0.23	0.005	3 %
4 - 5	0.14	0.0014	2 %
5 - 6	0.10	0.0008	1 %

Table 9.2: χ^2 values calculated for cross sections corresponding to two consecutive iterations for the $\Delta\eta^F$ distribution. r_{dist} is the maximal relative distance (calculated bin-by-bin) of the corrected cross section between two consecutive iterations. Jets reconstructed by the anti- k_T $R = 0.6$ algorithm.

Iterations	χ^2 (full range)	χ^2 ($-3.5 < \log_{10} \tilde{\xi}^\pm < -1$)	r_{dist}
1 - 2	45	0.91	7 %
2 - 3	20	0.15	5 %
3 - 4	11	0.037	4 %
4 - 5	6	0.012	2 %
5 - 6	4	0.006	2 %

Table 9.3: χ^2 values calculated for cross sections corresponding to two consecutive iterations for the $\tilde{\xi}^\pm$ distribution. r_{dist} is the maximal relative distance (calculated bin-by-bin) of the corrected cross section between two consecutive iterations. Jets reconstructed by the anti- k_T $R = 0.6$ algorithm.

Another variable defined to provide a quantitative insight into the unfolding method is a maximum relative distance (calculated bin-by-bin) of the corrected cross section between two iterations:

$$r_{\text{dist}}(i^{\text{th}} \text{ iter.}) = \text{Max}_{j_{\text{bins}}} \frac{|y_{i,j} - y_{i-1,j}|}{y_{i-1,j}} \quad (9.2)$$

Combining all this information, we will be able to decide on an appropriate choice of the number of iterations.

Stability against binnings Testing the unfolding stability with respect to the choice of bins is presented in Figure 9.13. The "Coarse" binning is defined in Table 9.1. The "Fine" bins, reflecting more the actual resolutions of the jet p_T , are as follows:

- p_T "fine" bins (23) - 12, 16, 20, 30, 40, 50, 60, 70, 80, 90, 100, 110, 120, 130, 140, 150, 160, 170, 180, 200, 220, 240, 260, 450 GeV

The unfolding proves to be stable against the choice of p_T bins well within 1% for both the $\Delta\eta^F$ and $\tilde{\xi}^\pm$ distributions.

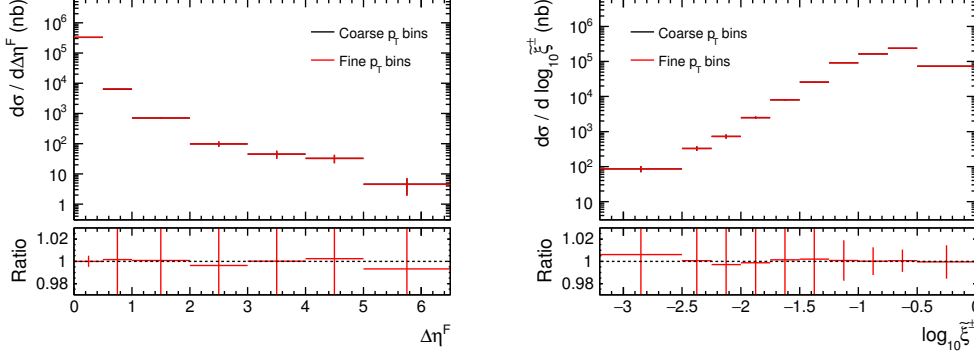


Figure 9.13: Comparisons of unfolded data (1 iteration) for different p_T binnings. Jets reconstructed by the anti- k_T $R = 0.6$ algorithm.

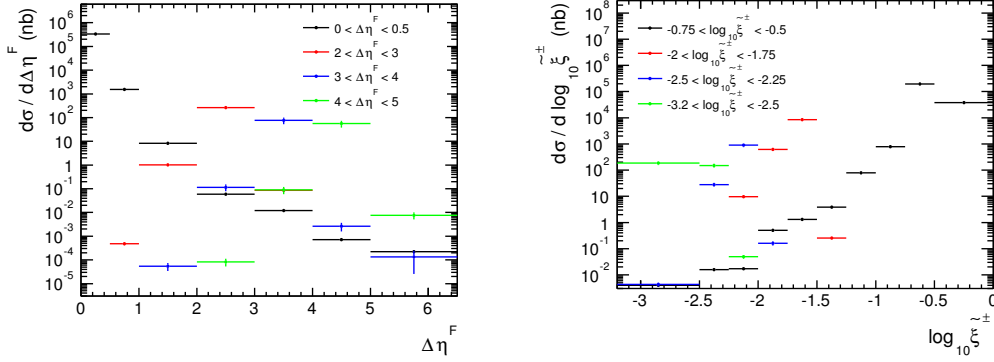


Figure 9.14: Migrations of events in selected reco-level bins due to the unfolding procedure (4 iterations). On x -axes, quantities after applying unfolding to selected reco-level bins in data (see legends) are plotted. Jets reconstructed by the anti- k_T $R = 0.6$ algorithm.

Migrations into neighbouring bins The IDS unfolding procedure adopted in this analysis takes into account not only bin-by-bin corrections between the detector level and particle level MC distributions, but also the influence of misses and fakes. As a result, events can migrate to neighbouring bins. This effect can be studied by unfolding a single bin only, instead of the full spectrum. This test is presented in Figure 9.14. As expected from the smearing matrix, the $\Delta\eta^F$ distribution in the large binning that we have selected has negligible migrations (suppressed at least by two orders of magnitude). What is also important to note is that the number of missing events caused by showering on the edge of the calorimeter (migrations from the detector level $\Delta\eta^F = 0 - 0.5$ to the unfolded $\Delta\eta^F > 3$) has no impact on the measurement - it is suppressed by five orders of magnitude. As for the $\tilde{\xi}^\pm$ distribution, a significant systematic shift from small to large $\tilde{\xi}^\pm$ values is observed. This is caused by the non-diagonality of the smearing matrix - due to the limited detector acceptance to low-energy particles, the reconstructed $\tilde{\xi}^\pm$ is systematically smaller than the particle level value.

9.2.4 Choice of the number of iterations

The regularization parameter within the unfolding method specifies the number of iterations. Usually, a reasonable performance can be achieved already with a small number of iterations. The price to pay for higher regularization parameter is usually a significant growth of statistical uncertainties. To decide on the optimal number of iterations, we can combine the information received from previous unfolding tests, notably the convergence of distributions corresponding to increasing number of iterations.

Figures 9.11 and 9.12 demonstrate that the number of iterations has minimal impact across most of the ranges. The biggest sensitivity to the choice of this parameter is in bins with lower statistics available, that is in bins of our interest (low $\tilde{\xi}^\pm$, large $\Delta\eta^F$). For making a decision, it is useful to take into consideration the χ^2 values in tables 9.2 and 9.3, especially those that are in our region of interest to avoid χ^2 domination by low $\Delta\eta^F$ (high $\tilde{\xi}^\pm$) bins which have majority of the statistics (therefore low statistical uncertainties entering the χ^2 calculation). The χ^2 values rapidly decrease with increasing number of iterations and have typically very small values, that is smaller than 1 in all cases except the ξ in full range. However, the χ^2 values should be moreover divided by the number of degrees of freedom (number of bins), so we get well below 1 even in this case starting from fourth iteration.

To support this observation, we can inspect the r_{dist} values in tables 9.2 and 9.3. This distance between two consecutive iterations starts to be negligible (around or less than 2%) when going from 4th to 5th iteration.

Therefore, putting both these observation together, we come to the decision that four iterations is the appropriate choice for both the $\Delta\eta^F$ and $\tilde{\xi}^\pm$ distributions.

9.2.5 Statistical uncertainties

Statistical uncertainties of unfolded (fully corrected) spectra can be evaluated by smearing the input 2D histograms with raw events by the Poisson distribution with mean value of the number of entries in given bin. Histograms are then normalized to the cross-section and unfolding is being run. This procedure is repeated 1000 times (so called “pseudo-experiments”). The result is presented in Figure 9.15. The total statistical uncertainty comprises of the data and Monte Carlo components. Statistical fluctuations in data are evaluated by smearing the input detector level data distribution, keeping the Monte Carlo inputs unchanged, while the Monte Carlo component is evaluated by Poisson smearing of the input smearing matrix (correlation of the particle level and detector level measurable quantity), keeping the data detector level histogram unchanged. The result of this test proves that the dominant contribution to the overall statistical error is coming from a limited statistics in the data (error up to 50%) and a good available statistics of Monte Carlo events across full range of interest in both $\tilde{\xi}^\pm$ and $\Delta\eta^F$ (below 0.1%).

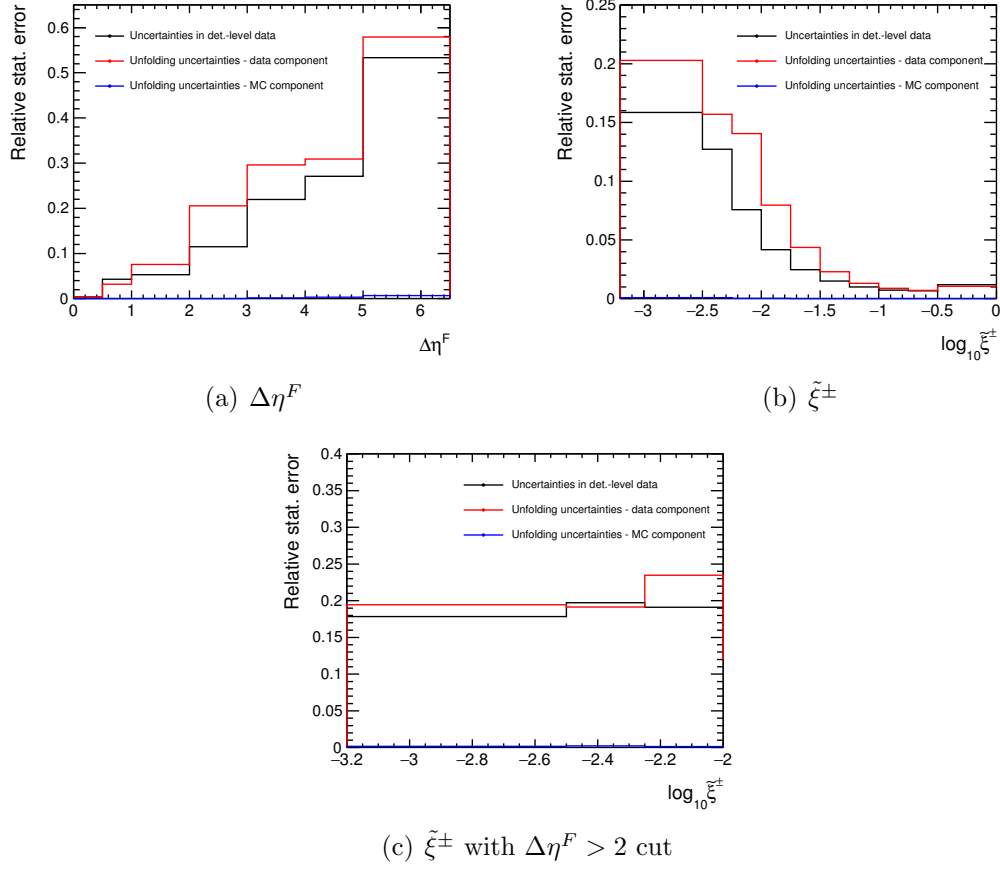


Figure 9.15: Statistical uncertainties of the unfolded distributions as coming from the Monte Carlo and data. The detector level statistical errors in data are also depicted.

9.3 Comparison of 1D and 2D unfolding techniques

For $\Delta\eta^F$ and $\tilde{\xi}^\pm$, it is possible to use the 1D approach but this does not take into account having multiple exponentially falling distributions. A comparison of the 2D and 1D unfolding methods is shown in Figure 9.16. Different approaches lead to similar results with the exception of bins with very limited statistics.

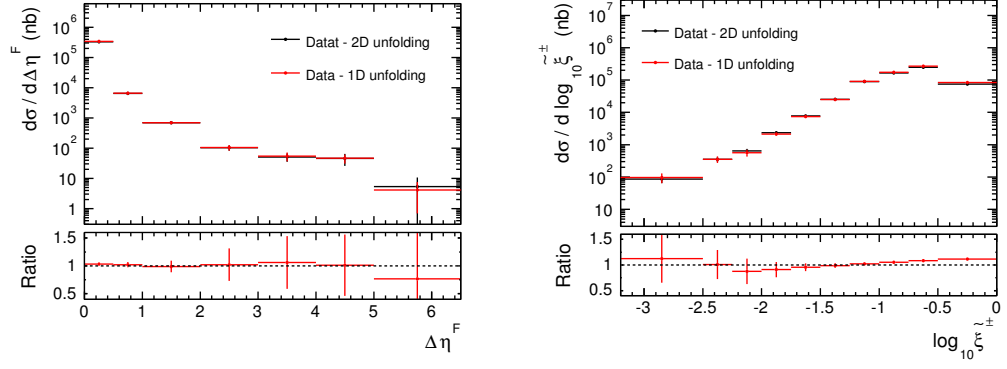


Figure 9.16: Comparison of the unfolded data distributions between the 1D and 2D unfolding methods for $\Delta\eta^F$ and ξ^{\pm} selected with anti- k_T $R = 0.6$ jets.

10. Evaluation of systematic uncertainties

Each experimental measurement made by a complex detection system such as the ATLAS detector is influenced by systematic uncertainties arising from the reconstruction of detector objects such as jets, tracks etc. There is usually a wide range of sources of uncertainties which have, sometimes significant, impact on the final result of the measurement. As we shall see later on in this chapter (systematic uncertainties will turn out to be large), their careful evaluation can be as essential for the interpretation of the final result as the measurement itself.

The goal of this chapter is to calculate asymmetric bin-by-bin systematic uncertainties for both $\Delta\eta^F$ and $\tilde{\xi}^\pm$ distributions. Generally, the uncertainty is evaluated by running the uncertainty-adjusted analysis (i.e. with shifts, smearings, different weights etc.) on Monte Carlo (used for unfolding) samples. This way, new response matrices and detector level distributions are obtained and used for unfolding the nominal (unchanged) detector level data. The particular uncertainty is obtained by comparing the newly unfolded data to the nominal unfolded data distribution. Since systematic uncertainties from different sources are uncorrelated, they are eventually added together in quadrature to obtain the total systematic uncertainty of the measurement.

10.1 Jet-related systematic uncertainties

Uncertainties related to the reconstruction of jets, which is based on TopoClusters at the EM scale, is systematically influenced by factors such as dead material, energy leakage, jet triggering, non-compensation of calorimeter for hadrons and generally inefficiencies in the calorimeter clustering and jet reconstruction. The evaluation of jet-related systematics is mostly based on the 2010 inclusive dijet measurement [44].

10.1.1 Uncertainty of the L1_J5 Trigger Efficiency Fits

The trigger strategy adopted in this analysis is such that the events are collected below the 99% efficiency region. Fits of the trigger efficiency curves in five different η -ranges have been made. The trigger uncertainty can be evaluated by varying three fit parameters by their uncertainty, one at a time in all five η -ranges. The procedure is not, however, that straightforward as the fit parameters are correlated. The correlation matrix can be retrieved from the fitting procedure in ROOT and subsequently diagonalized. Fit parameters in the diagonal basis are not correlated anymore and their uncertainty is the square-root of the eigenvalues of the diagonal matrix. Their values can thus be adjusted up or down and propagated back to the non-diagonal basis. The overall effect of the trigger fit uncertainty is then retrieved as the sum of squares of relative differences of thirty measurements ($30 = 5_{\eta\text{-ranges}} \cdot 3_{\text{Parameters}} \cdot 2_{\text{Up\&Down}}$) with respect to the nominal

data distribution. This systematic uncertainty is below 0.7% across full $\Delta\eta^F$ and $\tilde{\xi}^\pm$ range with the exception of the bin with the largest $\Delta\eta^F$ where the statistical fluctuations influence the result (1.3%).

10.1.2 Trigger uncertainty

The trigger systematics can be evaluated by the use of Monte Carlo events. Our default MC selection does not contain triggers, though they are well modeled. We can therefore measure L1_J5 efficiencies in the same η -ranges as in data, fit them and use these fits to obtain additional event weights. The uncertainty is then obtained by comparing these MC distributions with our nominal Monte Carlo distributions (i.e. without the use of triggers). As the prescale of the L1_MBTS.1 trigger is not simulated in the MC (PS=1), it had to be incorporated by hand by the use of the random number generator. Thirty-nine events out of fourty (PS was, in period B, around 40-50) were removed and the remaining events appropriately scaled. The resulting uncertainty is within 3.5%.

10.1.3 Jet Energy Scale uncertainty (JES)

The EM+JES jet energy scale determination is based on comparing energies of reconstructed (EM scale energy) and truth isolated jets in MC and providing a correction as a function of η and p_T (for details see [51]). The uncertainty on the jet energy scale accounts for uncertainties in a number of factors including the absolute EM scale (e.g. dead material, electronic noise, different responses of the LAr and Tile calorimeters), the simulation of particle showers in calorimeters, pile-up and the models of fragmentation used by different MC generators.

There are various components of the jet energy scale uncertainty:

- JES 1 (CALORIMETER) - calorimeter uncertainty from single particle propagation
- JES 2 (NOISETHRESHOLDS) - use TopoCluster noise thresholds from data
- JES 3 (PERUGIATUNE) - Perugia 2010 Pythia tune
- JES 4 (ALPGENHERWIGJIMMY) - Alpgen+Herwig+Jimmy
- JES 5 (ETAINTERCALIBRATION) - uncertainty due to intercalibration (end-cap with respect to the central region)
- JES 6 (CLOSURE) - non-closure of numerical inversion constants
- JES 7 (PILEUP) - uncertainty due to in-time pile-up

Each component is evaluated by single p_T and η dependent shifts of the jet p_T up and down in the MC, whilst keeping the data fixed. The combined uncertainty for EM+JES jets reconstructed from topological clusters, in zero pile-up conditions, is taken from [44] and its effect on the p_T distribution of the leading jet is shown

in Figure 10.1. It is largest at low p_T and in the forward region. The effect of the JES uncertainty on both the $\Delta\eta^F$ and $\tilde{\xi}^\pm$ per JES component is shown in Figure 10.2. The major contribution is from the eta intercalibration component, while, as expected from practically non pile-up environment in the 2010 period B data, the pile-up component has a zero effect.

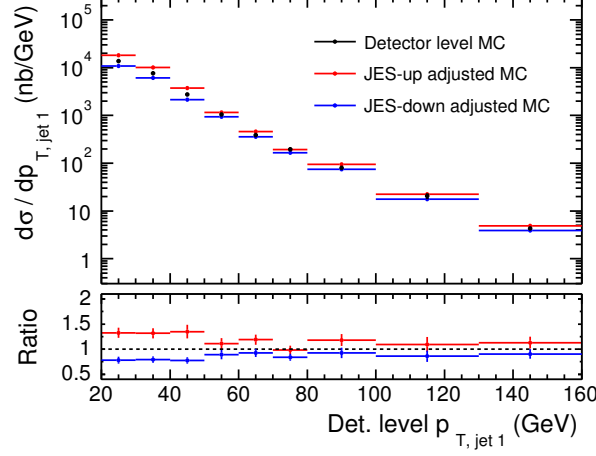


Figure 10.1: The impact of the combined Jet Energy Scale uncertainty for p_T of EM+JES jets reconstructed from topological clusters using the anti- k_T with $R = 0.6$ algorithm.

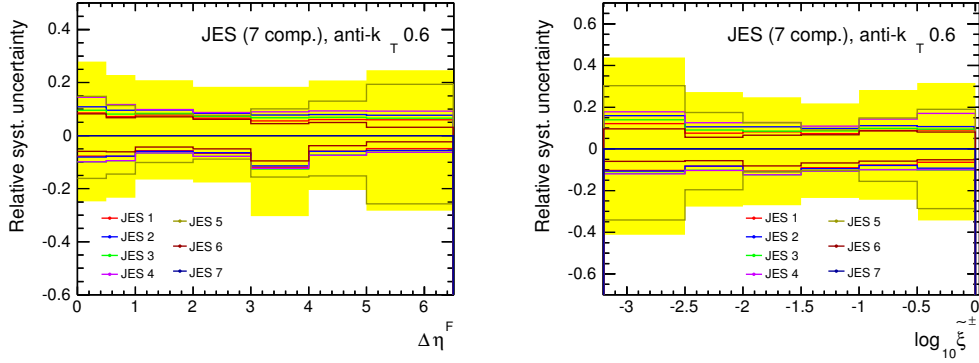


Figure 10.2: Jet Energy Scale uncertainty of its seven components for EM+JES jets reconstructed from topological clusters using the anti- k_T algorithm $R = 0.6$. The yellow band is the combined uncertainty calculated by adding all seven components in quadrature.

Diffraction dijets with very large gaps are constrained to be forward-going and are mostly found at the low p_T limit where the JES uncertainty is largest. As in the 2010 inclusive dijet analysis, this is the dominant contribution to the systematic uncertainty and the resulting change in the differential cross section is typically between 20-40%.

10.1.4 Jet Energy Resolution (JER)

The jet energy resolution is obtained along with the jet energy response measurement. The distribution of the ratio of p_T of the calorimeter jets and matched truth jets is fitted with a Gaussian function. While the mean value is the average jet energy response, the width of the Gaussian fit relative to the mean value is the jet energy resolution. For details, see [52].

The uncertainty on the measurement due to the energy resolution is evaluated by smearing the p_T of the reconstructed jets in the MC with a Gaussian defined by σ_{smear} , using the formula

$$\sigma_{\text{smear}}^2 = (\sigma_{\text{nominal}} + \Delta\sigma)^2 - \sigma_{\text{nominal}}^2, \quad (10.1)$$

where $\Delta\sigma$ is the uncertainty of the nominal σ_{nominal} jet energy resolution. The left-hand side plot of Figure 10.3 demonstrates the effect of such smearing across a full p_T and η range.

To obtain a statistically relevant result, 1000 pseudo-experiments was run on each MC event. The resulting change in the differential cross section is within 6%.

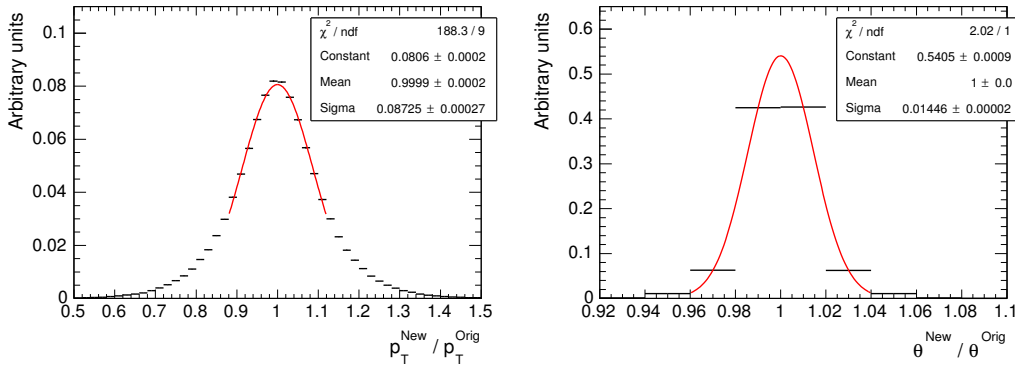


Figure 10.3: Relative shifts applied to jets for the evaluation of the Jet Energy Resolution (left) and the Jet Angular Resolution (right) uncertainty. Both distributions are integrated over full phase space (p_T and η for JER and E and η for JAR). Superscripts “New” (“Orig”) refer to the uncertainty-corrected (original) jet variable.

10.1.5 Jet Angular Resolution (JAR)

Another uncertainty related to the jet reconstruction comes from the resolution in the jet ϕ and η . It is measured using a similar technique as the one for the jet energy response and resolution. The resolution is largest for low- p_T jets (up to 0.05 for jets with $p_T = 20$ GeV), becoming smaller than 0.01 for jets with $p_T > 100$ GeV.

Details about this systematic uncertainty for dijet events can be again found

in the 2010 inclusive dijet analysis documentation. As the uncertainty $\Delta\sigma$ on the nominal resolution σ_{nominal} is very small, $\Delta\sigma$ is fixed at 0.1 for all jets (based on recommendations of the inclusive dijet analysis). The right-hand side plot of Figure 10.3 demonstrates the effect of such smearing across a full E and η range. The systematic uncertainty is evaluated in a similar way as the JER (1000 pseudo-experiments on each event are done) and the resulting change in the differential cross section is typically around 1-2%, a value practically negligible compared to the JES uncertainty.

10.1.6 Jet Reconstruction Efficiency (JRE)

The efficiency of the reconstruction of calorimeter jets can be assessed by using track jets acting as a proxy for truth jets. It is measured in both the data and Monte Carlo, which provides a possibility to study a possible mis-modelling of the calorimeter jet reconstruction efficiency. The difference, determined for the 2010 inclusive dijet analysis, was found to be 2% for jets with $p_T < 20$ GeV, becoming less than 1% for $p_T > 30$ GeV, and is applied as an event weight. The resulting change in the differential cross section is at most 2%.

10.1.7 Jet Cleaning Efficiency (JCE)

The standard medium quality jet cleaning cuts have an η and p_T dependent efficiency, as was already discussed in Section 6.3.3 and as is demonstrated by Figure 6.17. Many of the jet cleaning variables are not modelled well in the MC and so the jet cleaning efficiency, defined as the number of jets remaining after cleaning compared to the total number of jets, has been studied in ATLAS in-situ using a tag-and-probe technique (the measured “probe” jet is required to balance in p_T and ϕ the central “tag” jet with $|\eta| < 2$). A detailed description is provided in the 2010 inclusive dijet measurement documentation.

The jet cleaning efficiency for jets with $p_T > 100$ GeV is above 99% in all η regions, but can decrease down to $\sim 86\%$ for jet $p_T \sim 20$ GeV. Systematic uncertainties on the jet cleaning efficiency were derived by applying looser and tighter selection criteria to the tag jet, and were found to be less than 2% across p_T and η . The effect on the differential cross section as a function of $\Delta\eta^F$ and $\tilde{\xi}^\pm$ is typically $\sim 8\%$, well below the one from the jet energy scale uncertainty.

10.2 Diffractive systematic uncertainties

The systematic uncertainty sources related to specifics of the diffractive measurement are inspired by the ATLAS soft rapidity gap analysis [45] and the E_T -flow analysis [49]. In the end, they are added together in quadrature with other systematic uncertainty sources to provide overall uncertainty for the $\Delta\eta^F$ and $\tilde{\xi}^\pm$ measurement.

10.2.1 Left-right asymmetry of the rapidity gap start

Given the ATLAS detector symmetry around $\eta = 0$, the $\Delta\eta^F$ distributions should be the same when retrieved separately for the rapidity gap start from the left ($\eta_{\text{start}} = -4.8$) and right ($\eta_{\text{start}} = +4.8$) side. There could be certain detector effects causing asymmetry of such independent measurements, in which case, however, the distributions should get symmetrized after performing the unfolding procedure.

In Figure 10.4, the result of this test is presented. Given large statistical uncertainties at larger $\Delta\eta^F$ values, the left-right comparison can be considered compatible and this possible source of systematic uncertainty is therefore considered to be negligible in comparison to the JES uncertainty.

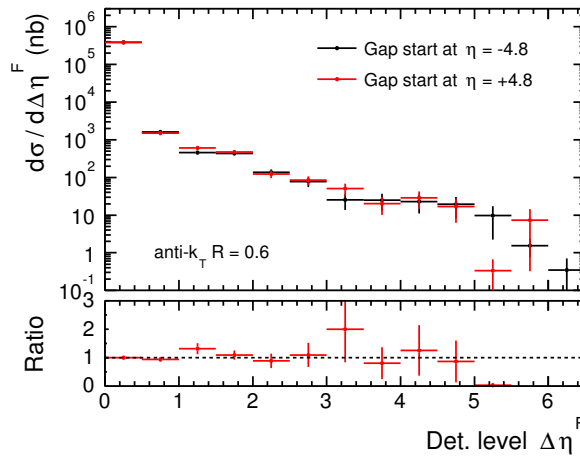


Figure 10.4: Uncorrected cross section as a function of the $\Delta\eta^F$, constructed starting from the left edge ($\eta = -4.8$) or from the right edge ($\eta = +4.8$) of the calorimeter. For events found using the anti- k_T $R = 0.6$ algorithm. Statistical uncertainties only.

10.2.2 Cluster energy scale uncertainty (CES)

The uncertainty of the cluster energy scale is tested by adjusting the cluster energy correction factor, $1 + \alpha$, for combined EM and hadronic uncertainty (refer to the “combined uncertainty” column in Table 7.1 and Figure 10.5). This uncertainty affects only the ξ^\pm measurement as the $\Delta\eta^F$ definition does not use any energy or transverse momentum cut applied to TopoClusters. The resulting change in the differential cross section is typically 10% and is depicted in summary plots in Section 10.4.

10.2.3 Cell Significance Threshold Uncertainty (CST)

Following the 2010 minimum bias rapidity gaps analysis, the η ring significance thresholds (S_{th}) for clusters to exceed the noise fluctuation requirement were shifted up and down by 10% to observe the effect on the forward gap size distribution.

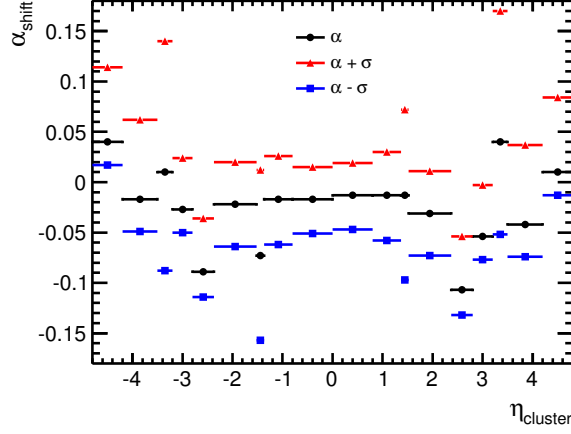


Figure 10.5: Cluster energy shift using the central α values and after applying the “combined uncertainty”. Plot created based on values in Table 7.1.

The systematic effect on the final result in the rapidity gaps cross section measurement was less than 5%, due to the fact that the clusters at $\eta = \pm 4.9$ had an energy cut of 12 GeV resulting from the p_T cut of 200 MeV. For the diffractive dijets analysis, the requirement of clusters with $p > 0$ across the whole of the detector is more sensitive to this shift, particularly in the forward regions, and the resulting change in the differential cross section is typically 10-20% and is depicted in summary plots in Section 10.4.

10.2.4 Tracking uncertainty

The main tracking uncertainty (specific for the $\Delta\eta^F$ measurement) arises from reconstruction inefficiencies of charged particle tracks due to possible mis-modelling of the detector material through which the particles have to pass. It is taken from the 2010 minimum bias rapidity gaps analysis, where the effect of track reconstruction efficiency was taken into account by studying the influence of the additional material (new MC sample with 10% material enhancement was produced) in the inner detector through which charged particles pass. The resulting uncertainty was found to be smaller than 3.5% throughout the measured distribution and was applied globally in all bins of measured quantities.

10.3 Other sources

10.3.1 Luminosity uncertainty

The uncertainty on the luminosity is taken from the final 2010 luminosity determination [53] to be $\pm 3.5\%$ and is applied in all bins of $\Delta\eta^F$ and $\tilde{\xi}^\pm$ quantities.

10.3.2 Primary vertex requirement

One of the basic event selection cuts requires a presence of a primary vertex with two or more associated tracks. This can lead to an inefficiency, which can be assessed by by loosening the requirement in data to allow events without a primary vertex but still not allow pile-up vertices. The increase of the number of events results in a change of the differential cross section of 1%. The fact that it is such a small effect can be understood as a result of the requirement on a presence of two high p_T jets, i.e. a system with a lot of hadronic activity.

10.3.3 Additional material

The effect of dead material requires an understanding of the detector geometry. Properly evaluating the corresponding uncertainties requires special samples to be generated in which the material budget of the inner detector, services and calorimeters are modified. The uncertainty was not directly evaluated but instead taken from the minimum bias rapidity gaps analysis as a symmetric shift of $\pm 3.0\%$ to be applied to the total systematic uncertainty in each bin of the $\Delta\eta^F$ measurement. This systematic shift cannot be applied to $\tilde{\xi}^\pm$ measurement as this is a completely different variable, which was not studied in the soft gap analysis. However, we can exploit the E_T flow analysis [49] which studied the influence of an extra material (geometry tag ATLAS-GEO-16-19-00) on the cluster energy density, see Section 6.2 in the E_T flow paper. A downward shift by 5% (conservative estimate) was found and it can be applied to the cluster p_T , which is used for the $\tilde{\xi}^\pm$ calculation. The resulting uncertainty is found to be $\pm 10\%$ (symmetrized around zero just as in the E_T flow analysis), as demonstrated in Figure 10.6.

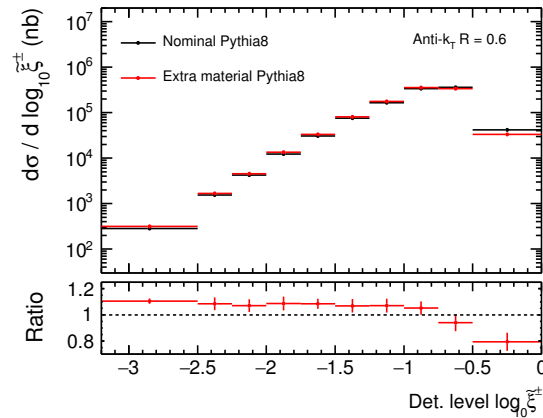


Figure 10.6: Systematic uncertainty due to the dead material: nominal $\tilde{\xi}^\pm$ spectrum of Pythia8 ND+SD+DD vs $\tilde{\xi}^\pm$ calculated from clusters with 5% downward shift in p_T .

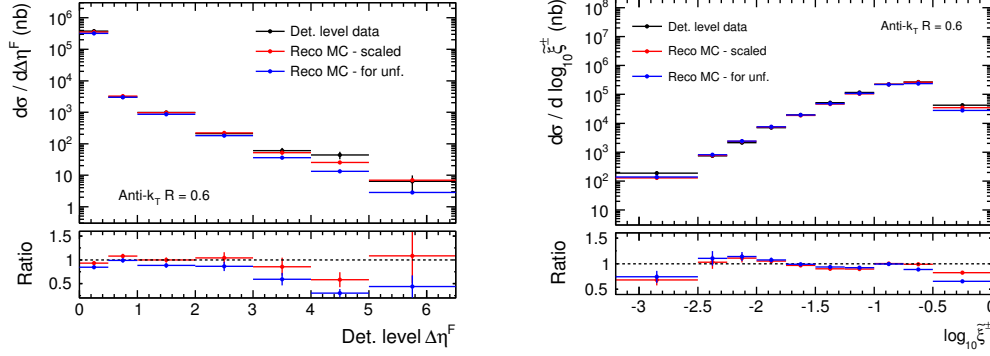


Figure 10.7: Unfolding systematics control plots for $\Delta\eta^F$ and $\tilde{\xi}^\pm$ distributions using the anti- k_T algorithm with $R = 0.6$ algorithm. Detector level data (black) is compared to Pythia8 scaled by the continuous polynomial function (red) to better describe the data. Comparison to detector level MC used for unfolding (blue) is also presented.

10.3.4 Unfolding uncertainty

The uncertainty introduced by the unfolding procedure can be evaluated by a data-driven test based on the detector level MC and data comparison. The ratio of the MC and data distribution is fitted by a smooth function, which is then used as a reweighting function of the smearing matrix. The reweighting is applied on particle level quantity ($\Delta\eta^F$ or $\tilde{\xi}^\pm$) extracted by doing 1D projection of the smearing matrix to the y -axis. The reweighted smearing matrix can then be projected to x -axis to obtain detector level spectrum, which now describes data significantly better (it does not need to be perfect, though), as demonstrated in Figure 10.7. The reweighting functions used are polynomials of the fourth order with parameters

- $\Delta\eta^F$ spectrum: $0.705 - 0.264x + 0.05x^2 + 6.63 \cdot 10^{-3}x^3 - 8.12 \cdot 10^{-4}x^4$
- $\tilde{\xi}^\pm$ spectrum: $1.66 + 2.98x + 3.06x^2 + 1.33x^3 + 0.2x^4$

The reweighted detector level MC is then unfolded by the standard procedure used on data and the systematic uncertainty is then evaluated as the difference between the unfolded reweighted MC and the reweighted particle level MC. In order to test the sensitivity of the unfolding method to statistical fluctuations in Monte Carlo, this test should be made statistically independent. This goal is achieved by assigning each event an additional weight coming from a random number generator with the Poisson distribution of the mean value $\mu = 1$. The resulting unfolding uncertainty is typically around 10%, only in some bins going up to $\sim 15\%$.

10.4 Summary: combined systematic uncertainties

The systematic uncertainties discussed above are depicted in Figure 10.8 as a function of the $\Delta\eta^F$, in Figure 10.9 as a function of the $\tilde{\xi}^\pm$ (inclusive) and in Figure

10.10 as a function of the $\tilde{\xi}^\pm$ with $\Delta\eta^F > 2$ cut. Numerically, they are summarized in tables in Appendix B. The yellow band represents the overall uncertainty calculated as the square-root of the sum of the individual uncertainties squared. The dominant contribution is coming from the jet energy scale followed by the cell significance threshold in case of rapidity gaps and the cluster energy scale in case of $\tilde{\xi}^\pm$. The overall uncertainty is within 20-50%.

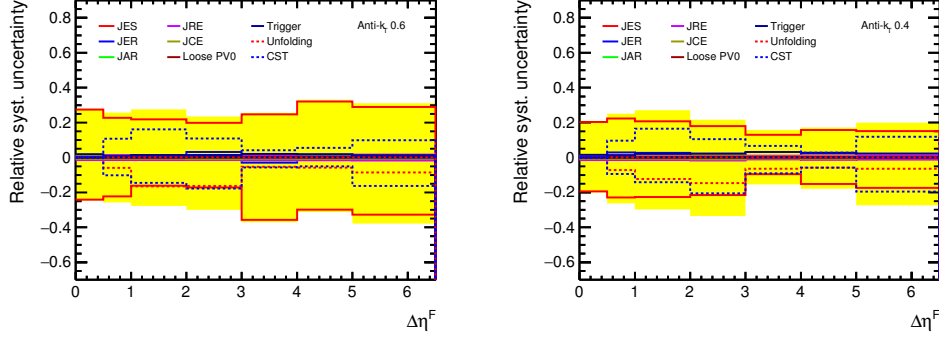


Figure 10.8: Systematic uncertainties for EM+JES jets reconstructed from topological clusters using the anti- k_T algorithm with $R = 0.6$ (left) and $R = 0.4$ (right). The yellow band presents the combined uncertainty.

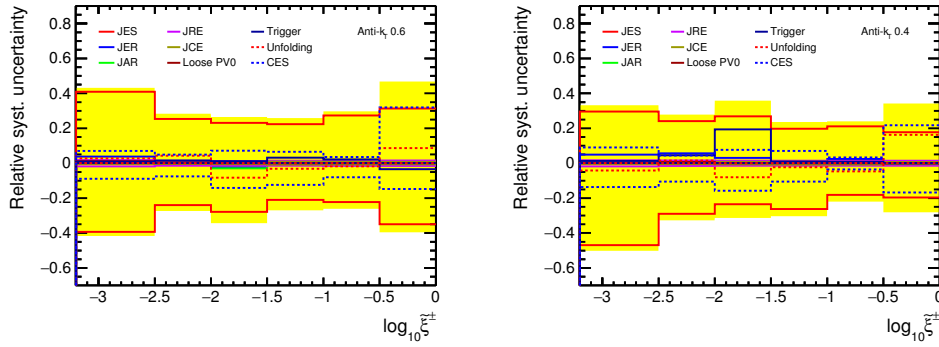


Figure 10.9: Systematic uncertainties for EM+JES jets reconstructed from topological clusters using the anti- k_T algorithm with $R = 0.6$ (left) and $R = 0.4$ (right). The yellow band presents the combined uncertainty.

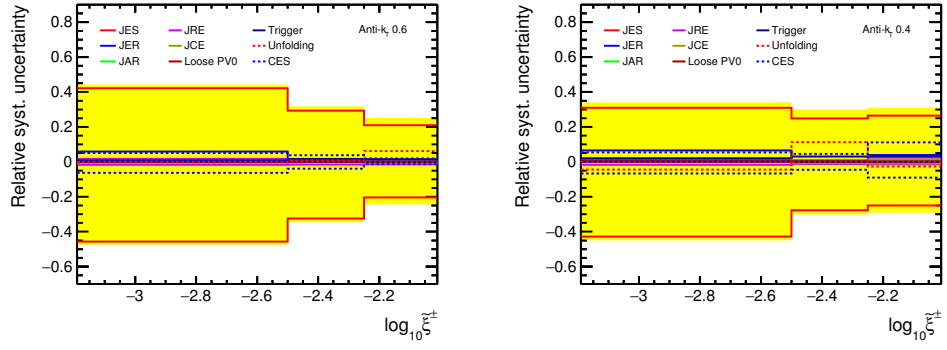


Figure 10.10: Systematic uncertainties for $\tilde{\xi}^{\pm}$ with $\Delta\eta^F > 2$ cut for EM+JES jets reconstructed from topological clusters using the anti- k_T algorithm with $R = 0.6$ (left) and $R = 0.4$ (right). The yellow band presents the combined uncertainty.

11. Background influence

As one of the main goals of this analysis is an enhancement of the single diffractive contribution, obvious physical backgrounds are the non-diffractive and double diffractive processes, as well as the Double Pomeron Exchange. They are thoroughly discussed in Chapter 12.

Besides physical processes, significant sources of background come from the collision environment and can be classified into three categories:

- In-time pile-up
- Out-of-time pile-up
- Beam induced background

11.1 In-time pile-up

The multiple interactions in one bunch crossing form a background contribution called the *in-time pile-up*. This contribution takes place in this analysis despite the pile-up suppression cut (only one vertex with at least two associated tracks per event) due to the limited position resolution of the vertex reconstruction procedure. This effect leads to the merging of vertices closer than $\Delta z = 10$ mm into one. As a result, certain fraction f of dijet events are contaminated by an additional interaction in the same bunch crossing. The fraction f can be estimated by plotting the $\Delta z(\text{PV0}, \text{vtx}_{\text{PU}})$ distribution between the primary vertex and the closest pile-up vertex, as shown in Figure 11.2. To estimate the fraction of merging vertices in two-vertex events f' , a gaussian fit of the distribution needs to be done. Since the Δz has a non-gaussian shape, the fit was done in the central region only and the result is $f' = 0.039$. To obtain the fraction f , the f' has to be multiplied by the probability of a multiple interactions occurrence in the given data-sample, which was found to be 6% (from the distribution of the number of two-track vertices). The result is $f = 0.0023$, meaning that the expected effect of the in-time pile-up is very small. To evaluate it, a “toy” sample made of minimum bias events has been created (by running on period B data with L1_MBTS.1 trigger) and overlayed with the nominal data sample with probability f . If the toy rapidity gap is smaller than the nominal one, then $\Delta\eta_{\text{nominal}}^F$ is set to the value $\Delta\eta_{\text{toy}}^F$. The ξ^\pm distribution is influenced by the extra energy deposition and since it is calculated by summing over all clusters in a given event, the resulting value is $\tilde{\xi}_{\text{Final}}^\pm = \tilde{\xi}_{\text{Toy}}^\pm + \tilde{\xi}_{\text{Nominal}}^\pm$. Two hundred pseudo-experiments have been done in order to remove statistical fluctuations. The resulting distributions presented in Figure ?? demonstrate that the effect of the in-time pile-up is within 0.5%.

11.2 Out-of-time pile-up

The out-of-time pile-up is caused by overlapping signals in the detector from neighboring bunch crossings. Typically, the observed energy in calorimeters is

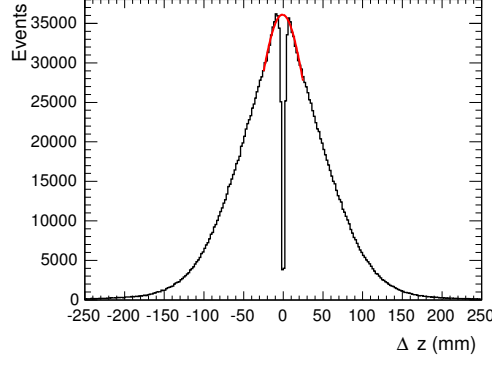


Figure 11.1: Δz distribution between the primary vertex and the closest pile-up vertex as seen in the period B of the 2010 data taking.

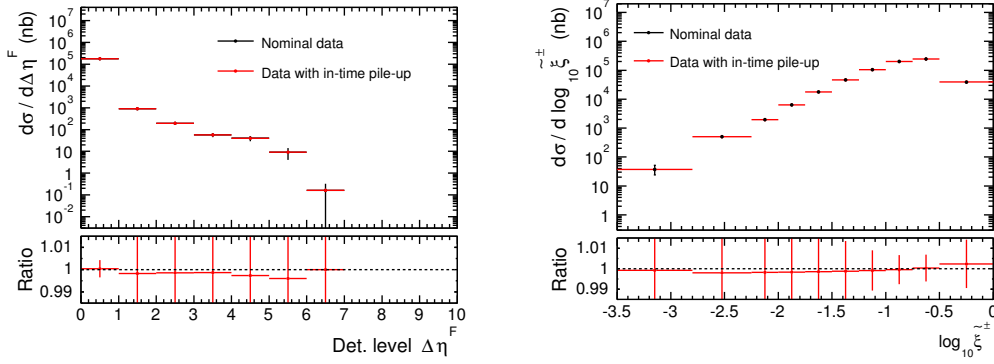


Figure 11.2: The effect of the in-time pile-up in comparison with the nominal data distributions.

decreased due to this effect. Run conditions in period B of the 2010 data taking are summarized in Table 6.1. The important characteristics is the bunch distance, Δt , which is not smaller than 5000 ns in the examined data sample. Since the out-of-time pile-up plays a role for $\Delta t < 400$ ns, it has no significance for the analysis presented in this paper.

11.3 Beam induced background

The beam induced background is caused by the so-called “beam-gas” or “beam-halo”, which is made of muons or pions traveling as a halo around the proton beam due to interactions of protons having been produced well upstream. To study this background, the analysis is repeated using so-called unpaired bunches, which are events with only one bunch of protons passing through the ATLAS detector. These events can be triggered by the L1_MBTS_1_UNPAIRED or L1_RD0_UNPAIRED (random trigger) and they allow, given their nature, to study separately the effect of the beam-halo only. This background is expected to have a negligible effect, just as was found out by the soft gap ATLAS analysis.

12. Results

The purpose of this chapter is to summarize results of the diffractive dijet measurement introduced in detail in previous chapters. The differential cross section is defined in Section 6.2.3 and is measured as a function of the rapidity gap size ($\Delta\eta^F$; introduced in Chapter 7) and the fractional momentum loss of the diffractive proton ($\tilde{\xi}^\pm$; introduced in Chapter 8). Additional distribution discussed here is the $\tilde{\xi}^\pm$ with a $\Delta\eta^F > 2$ cut whose purpose is to enhance the diffractive contribution. All distributions, measured for two distance parameters of the anti- k_T jet algorithm, are corrected for detector effects using the IDS unfolding technique (see Chapter 9). Various systematic uncertainties that influence this measurement are evaluated in Chapter 10 and are presented as yellow bands around data points. The error bars associated with data points represent statistical uncertainties only.

The event selection at the detector level is described in detail in Chapter 6. Two jets within $|\eta| < 4.4$ and with $p_T > 20$ GeV are required. A non pile-up collision environment is ensured by requiring that there is not more than one vertex with at least two associated tracks in the event.

The level to which the cross sections are corrected is described in Sections 7.5 and 8.1. The final state (stable) particles are required to be within the ATLAS detector acceptance range, $|\eta| < 4.8$, with the minimal momentum $p > 500$ MeV for charged particles and $p > 200$ MeV for neutral particles. This is valid for both $\Delta\eta^F$ and $\tilde{\xi}^\pm$ measurements; the only exception are charged particles in rapidity gap definition: they are required to have either $p > 500$ MeV or $p_T > 200$ MeV.

12.1 Measurement of $\Delta\eta^F$ and $\tilde{\xi}^\pm$

12.1.1 Process decomposition

In Figures 12.1 and 12.2, comparisons of data to PYTHIA8 ND, SD and DD processes for the $\Delta\eta^F$ and $\tilde{\xi}^\pm$ distributions are presented. The diffractive MC predictions are generated using the Donnachie-Landshoff (D-L) pomeron flux, which is currently the most commonly used (e.g. [45]) as the best option for describing the SD and DD events (other fluxes are going to be discussed in Section 12.1.4).

In contrast to the ATLAS soft rapidity gap analysis, no diffractive plateau is observed in the $\Delta\eta^F$ distribution in the region of large rapidity gaps. Instead, the cross section falls off with increasing rapidity gap size. This behaviour is explained by different event topology: while the previous soft gap analysis studied the diffractive events at soft scale (no jet requirement was introduced), our analysis is focused on harder scale (dijet production) which implies larger particle multiplicities (or, equivalently, larger invariant mass of the diffractive system X) to be observed in the detector with the same acceptance in the (p_T, η) space.

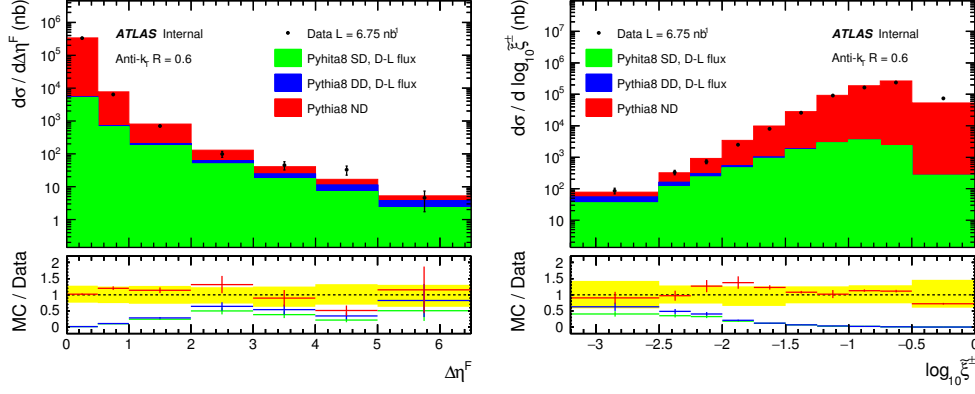


Figure 12.1: Comparison of the corrected data to the particle-level Monte Carlo ND, SD and DD components plotted as a stack. In the MC/Data ratio plots, SD/Data is represented by green, (SD+DD)/Data by blue and (ND+SD+DD)/Data by the red line. The jets were found the anti- k_T algorithm with $R = 0.6$. The yellow band presents the combined systematic uncertainty and the PYTHIA 8 ND contribution is normalized to match data in the first $\Delta\eta^F$ bin (by factor $1/1.35$).

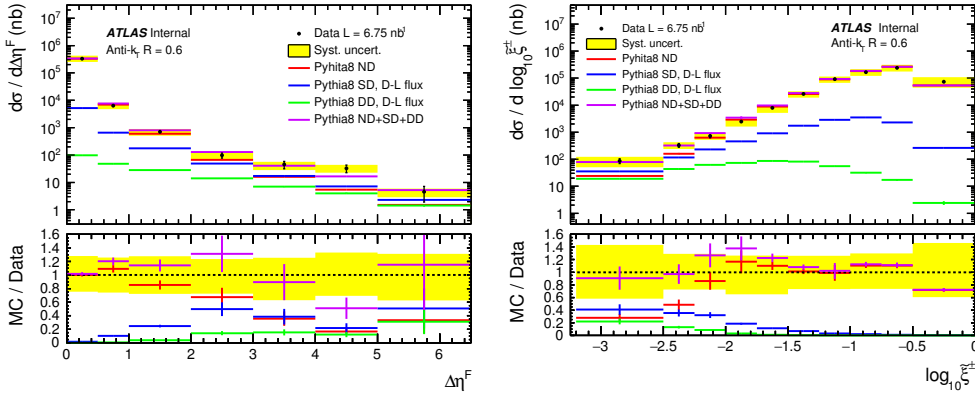


Figure 12.2: Comparison of the corrected data to the particle-level Monte Carlo ND, SD and DD components separately. The jets were found by the anti- k_T algorithm with $R = 0.6$. The yellow band presents the combined systematic uncertainty and the PYTHIA 8 ND contribution is normalized to match data in the first $\Delta\eta^F$ bin (by factor $1/1.35$).

By plotting comparisons of the data and various PYTHIA8 components, it is possible to study how the relative importance of ND, SD and DD processes as a function of both variables, $\Delta\eta^F$ and $\tilde{\xi}^\pm$. One of the important observations is that the lowest $\Delta\eta^F$ bin is dominated by ND events (the total cross section comprises of less than 2% of SD+DD processes). It is therefore possible to use this measurement to derive a multiplicative factor applicable to ND in order to make the Monte Carlo ND prediction match the data in the first $\Delta\eta^F$ bin. The factor is found to be $1/1.35$ for ND, while the SD and DD cross sections are left unchanged. Such a straightforward prescription is not possible to adopt in the case of the $\tilde{\xi}^\pm$ distribution which is observed to be flatter than that of the $\Delta\eta^F$,

nevertheless there is a region where the ND contribution is dominant as well: at high $\tilde{\xi}^\pm$, which corresponds to low $\Delta\eta^F$ values (see Figure 8.1). The chosen mixture of ND, SD and DD processes is therefore applied to the $\tilde{\xi}^\pm$ distribution as well.

As can be seen from Figure 12.2, the ND component dominates over the SD and DD ones by at least a factor of 10 in regions of very small gaps ($\Delta\eta^F \lesssim 1$) and very large $\tilde{\xi}^\pm$ ($\log \tilde{\xi}^\pm \gtrsim -1.5$). The ND and SD+DD components are then seen to equalize around $\Delta\eta^F \sim 3$ and $\log \tilde{\xi}^\pm \sim -2.25$ and finally, at very large gaps $\Delta\eta^F \gtrsim 4$ and very small $\tilde{\xi}^\pm$ ($\log \tilde{\xi}^\pm \lesssim -2.5$), the SD and DD components are dominant over the ND at least by a factor of 2 (see also Figures 12.5 and 12.6). Qualitatively, the situation is similar to that in the ATLAS soft rapidity gap analysis [45]: ND contribution makes up the majority of the cross section at low $\Delta\eta^F$. However, differences are seen in the region of large gaps where the ND processes are still present in the dijet analysis, whereas they are negligible in the ATLAS soft rapidity gap measurement.

Finally, it should be noted (see e.g. Figure 12.1) that not just the overall shape of both distributions is described reasonably well by PYTHIA8 ND+SD+DD, but also the total cross section is. This conclusion would be surprising for any model aspiring to provide good prediction of diffractive processes since the gap survival probability (S^2) is not simulated in any currently available MC model. This discrepancy is attributed to the fact that PYTHIA8 is not a straightforward implementation of a factorizable pomeron model. More appropriate choice for diffractive predictions (POMWIG) is going to be discussed later on in this chapter.

12.1.2 Comparisons to non-diffractive models

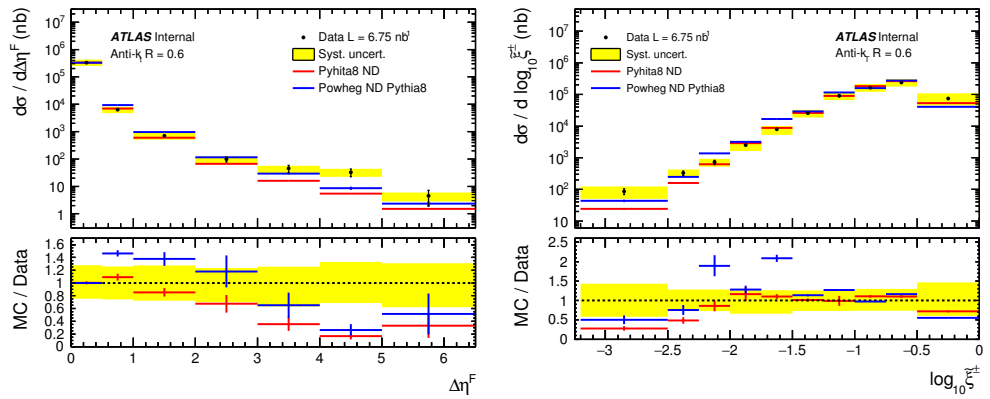


Figure 12.3: The differential cross sections (corrected data) for both $\Delta\eta^F$ (left) and $\tilde{\xi}^\pm$ (right) for jets found by the anti- k_T algorithm with $R = 0.6$. Data compared to two ND models all of them normalized to match data in the first $\Delta\eta^F$ bin (factors $f_{\text{Generator}}$): LO PYTHIA8 ($f_{\text{Pythia8}} = 1/1.35$) and NLO POWHEG with PYTHIA8 ($f_{\text{Powheg Py8}} = 0.93$) hadronisations.

To make reliable conclusions about the diffractive contribution in measured spectra, it is advisable to investigate more of ND predictions. In Figure 12.3, the dijet cross sections differential in $\Delta\eta^F$ and $\tilde{\xi}^\pm$ are compared with the PYTHIA8 ND contribution (at the leading order) and also with NLO calculation of non-diffractive dijet production in the POWHEG framework with hadronisation done by PYTHIA8. Both of the ND predictions are normalised to match the data in the first bin of the $\Delta\eta^F$ distribution. The two different ND predictions show a large uncertainty in the probability of producing gaps through hadronisation fluctuations, such that for $\Delta\eta^F < 4$ ($\log_{10} \tilde{\xi}^\pm > -2$), it is not possible to draw conclusions on the presence or absence of an additional diffractive contribution. However, the ND predictions fall significantly short of the data (by a factor of ~ 2 for NLO and even ~ 3 for LO) for $\Delta\eta^F > 4$ and for $\log_{10} \tilde{\xi}^\pm < -2.5$. These regions are therefore investigated in more detail in the following.

A presence of a significant ND contribution throughout the measured range also matches observations by the CMS Collaboration [13]. The requirement of dijets with p_T above 20 GeV inside the system X, even at larger gap sizes, increases the ND component relative to the total cross section. This contribution is, however, very sensitive to the modelling of rapidity gap fluctuations in the hadronisation, which are not well constrained.

12.1.3 Double Pomeron Exchange irreducible background

In Double Pomeron Exchange events, pomeron is emitted from each of the interacting protons. As a consequence, both of them remain intact and two forward rapidity gaps are thus produced. This kind of processes is usually called an irreducible background since they cannot be distinguished experimentally from the main signal events. To evaluate this contribution to the total cross section, DPE events were generated by the use of the Pomwig generator (50 million events for five p_T samples: 8-17 GeV, 17-35 GeV, 35-70 GeV, 70-140 GeV, 140-280 GeV). The particle level spectra compared to fully corrected data are presented in Figure 12.4. Depending on the chosen $\Delta\eta^F$ or $\tilde{\xi}^\pm$ bin, the suppression factor of DPE with respect to data is around 50 – 100 and these processes can thus be neglected.

12.1.4 Comparisons to various diffractive models

In order to enhance the final message coming from the dijet rapidity gap analysis, fully corrected data are compared to various diffractive MC models. Such comparisons are presented in Figure 12.5 for rapidity gap distributions and in Figure 12.6 for the fractional momentum loss of the scattered proton. It is important to note here that the $\tilde{\xi}^\pm$ variable (calculated by summing over energy depositions in the ATLAS calorimeter system, see Equation 8.2) can be considered a good estimate of the real ξ of the diffractive proton for $\log_{10} \tilde{\xi}^\pm < -1$ region only. This important conclusion follows from Figure 8.7(a) discussed in Section 8.1, in which is the $\tilde{\xi}^\pm$ calculation method validated. Larger $\tilde{\xi}^\pm$ must be interpreted as an energy flow measurement rather than the fractional momentum loss of the diffractive proton, as we can conclude from figures presented in this chapter as

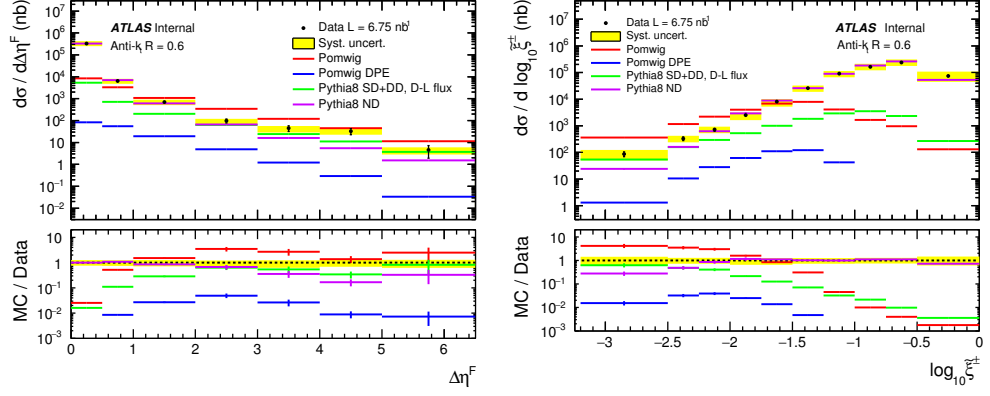


Figure 12.4: Particle level Double Pomeron Exchange $\Delta\eta^F$ (left) and $\tilde{\xi}^\pm$ (right) spectra in comparison with fully corrected data and other selected MC models. PYTHIA8 ND is normalized to match data in the first $\Delta\eta^F$ bin (by factor 1/1.35).

well (diffractive contribution is ~ 0 for larger $\tilde{\xi}^\pm$).

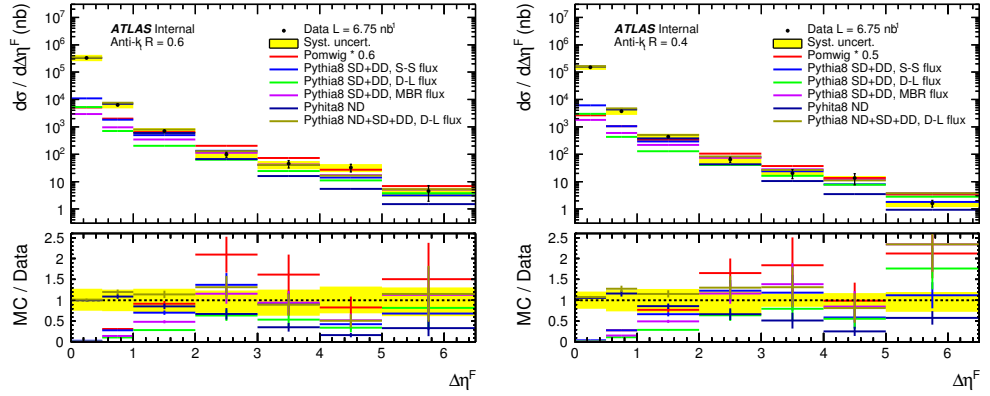


Figure 12.5: The differential cross section (corrected data) as a function of the $\Delta\eta^F$ for jets found by the anti- k_T algorithm with $R = 0.6$ (left) and $R = 0.4$ (right). The yellow band presents the combined systematic uncertainty. The Pomwig model is normalized by factors indicated in the legend and PYTHIA8 ND contribution is normalized to match data in the first $\Delta\eta^F$ bin (by factor 1/1.35).

Despite the fact that the $\Delta\eta^F$ distributions in Figure 12.5 reveal sizable differences observed among predictions of PYTHIA8 for the three different pomeron fluxes, the sum of SD and DD contributions for any option is roughly 3–4 times lower than that of the POMWIG SD model. Another interesting feature of the comparison between these samples is that the POMWIG SD distribution falls away less steeply with $\Delta\eta^F$ than PYTHIA8 SD+DD. Relative to the data, the POMWIG SD prediction in the $\Delta\eta^F$ distribution is approximately two times larger starting from $\Delta\eta^F = 2$ for both jet cone sizes.

In Figure 12.6, the measured cross section as a function of $\tilde{\xi}^\pm$ is presented. Comparisons to various diffractive models in the region of interest, i.e. at low $\tilde{\xi}^\pm$,

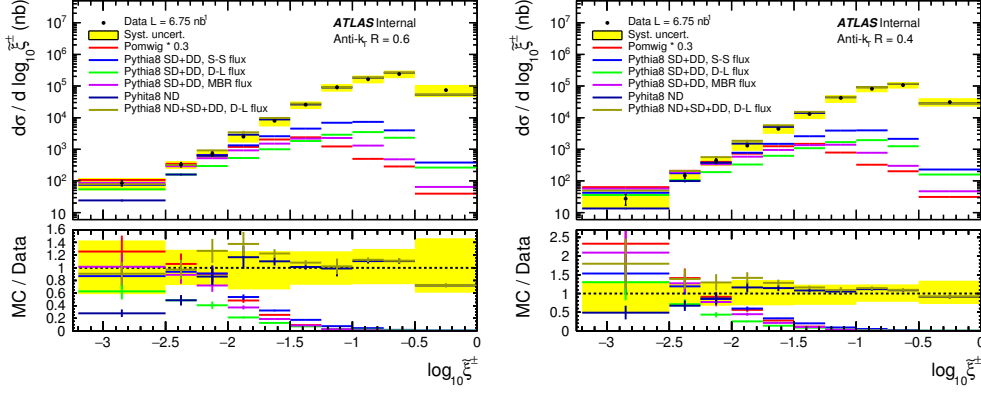


Figure 12.6: The differential cross section (corrected data) as a function of the $\tilde{\xi}^\pm$ for jets found by the anti- k_T algorithm with $R = 0.6$ (left) and $R = 0.4$ (right). The yellow band presents the combined systematic uncertainty. The Pomwig model is normalized by factors indicated in the legend and PYTHIA8 ND contribution is normalized to match data in the first $\Delta\eta^F$ bin (by factor $1/1.35$).

reveal a large overestimate by the POMWIG SD model (by factor ~ 4 in the lowest $\tilde{\xi}^\pm$ bin), while PYTHIA8 (SD+DD) predictions are not that far from the data - regardless the pomeron flux used. Another interesting comparison is between low and high $\tilde{\xi}^\pm$ region: while the $\tilde{\xi}^\pm$ predictions differ up to factor ~ 7 at large $\tilde{\xi}^\pm$, they get significantly closer at the low $\tilde{\xi}^\pm$ tail (differences within $\sim 40\%$).

This analysis was performed for two values of the distance parameter of the anti- k_T jet algorithm: $R = 0.4$ and $R = 0.6$. The larger distance parameter roughly doubles the cross section for the data but in overall, it keeps the ratio between the data and PYTHIA8 or POMWIG approximately the same. Differences are observed in the region of gaps larger than 3 where, however, the available statistics in the data is limited. It is not therefore possible to conclude whether a non-negligible dependence on the jet algorithm is observed in this region.

To further increase the ND suppression is lowest $\tilde{\xi}^\pm$ bins and thus enhance the diffractive contribution to the cross section in this region, it is possible to introduce an additional selection cut: events are required to have large rapidity gaps, $\Delta\eta^F > 2$. Such $\tilde{\xi}^\pm$ distributions are presented in Figure 12.7. This measurement is done for three lowest $\tilde{\xi}^\pm$ bins only due to the fact that the additional cut significantly limits statistics in all other bins (see Figure 8.1 for correlation between $\Delta\eta^F$ and ξ).

The $\tilde{\xi}^\pm$ distribution has also been measured by the CMS Collaboration [13]. It is not possible to do a direct comparison as the cross section definitions (at the particle level) are different. The CMS definition corrects the data to all final state particles in the range $-4.9 < \eta < +\infty$ ($-\infty < \eta < +4.9$) to include more of the system X, and the forward rapidity gap cut is 1.9 units in pseudorapidity. In this analysis, the forward rapidity gap range is $\Delta\eta^F > 2$ and the cross section is defined by $p > 200$ MeV for neutral particles and $p > 500$ MeV for charged

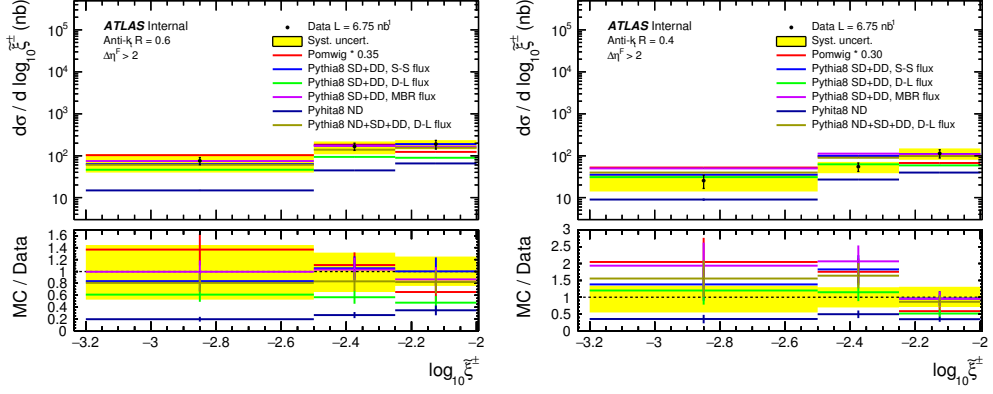


Figure 12.7: The differential cross section (corrected data) as a function of the ξ^\pm after the $\Delta\eta^F > 2$ cut for jets found by the anti- k_T algorithm with $R = 0.6$ (left) and $R = 0.4$ (right). The yellow band presents the combined systematic uncertainty. The Pomwig model is normalized by factors indicated in the legend and PYTHIA 8 ND contribution is normalized to match data in the first $\Delta\eta^F$ bin (by factor 1/1.35).

particles with the aim to better reflect what can be observed experimentally in ATLAS. Although the cross section definitions are different, the final fully corrected results are similar in magnitude.

12.2 Estimate of the gap survival probability

An explanation for the excess of the POMWIG prediction over data in the small ξ^\pm (large forward rapidity gap) region is the fact that a rapidity gap destruction mechanism is present in the data but not modelled in POMWIG. Indeed, as explained in Section 1.3.6, a similar excess had been first observed at the Tevatron and since then confirmed by other analyses. It is successfully explained by absorptive processes which depend on a number of variables and are quantified by the gap survival probability, S^2 . Although not expected to be a constant, S^2 is often expressed for a given process under examination as a constant number which is estimated for a range of ξ^\pm where diffractive processes dominate. Based on the discussions earlier in this chapter, the estimate of S^2 for diffraction in di-jet events is performed in the lowest ξ^\pm bin, where the ND contribution is small according to all available non-diffractive models. Moreover, for the first time for this type of analysis, an attempt to estimate S^2 from the measurement of the rapidity gap size in the region $3 < \Delta\eta^F < 4$ is also performed (larger $\Delta\eta^F$ values could provide better ND suppression, but it would be significantly influenced by larger statistical uncertainties).

As indicated previously, this analysis is specific in the sense that MC predictions are not yet tuned to describe the data well. One of the key aims is, therefore, to provide measurements of fully corrected data which can help to tune these imperfect models. It must be noted that the S^2 estimate presented in this section

is expected to have large theory uncertainties when trying to extract the relevant information from data using yet untuned MC models.

The gap survival probability S^2 is estimated from the ratio of the data and the SD contribution (predicted by POMWIG) in a given $\Delta\eta^F$ and $\tilde{\xi}^\pm$ region. Moreover, the ND contribution is removed from the data based on the leading order prediction by PYTHIA8. The influence of ND in selected bins is summarized in Table 12.1: the ND is suppressed by factors $\gtrsim 3$ for all bins, with the only exception of the rapidity gap bin for the $R = 0.4$ parameter of the jet anti- k_T algorithm (in such case, the factor is ~ 2). Finally, the DD contamination in the data is subtracted based on the DD/SD ratio as obtained from the PYTHIA8 generator with the Donnachie-Landshoff pomeron flux¹. The diffractive contribution in the $\tilde{\xi}^\pm$ spectrum is enhanced by the $\Delta\eta^F > 2$ requirement.

Data / MC	$3 < \Delta\eta^F < 4$	$-3.2 < \log \tilde{\xi}^\pm < -2.5$
Data/ND _{PYTHIA8} , Anti- k_T $R = 0.6$	2.8 ± 1.0	5.1 ± 1.0
Data/ND _{PYTHIA8} , Anti- k_T $R = 0.4$	1.9 ± 0.7	2.8 ± 1.0

Table 12.1: Data to PYTHIA8 ND ratios along with the statistical uncertainties for selected bins in $\Delta\eta^F$ and $\tilde{\xi}^\pm$. The $\tilde{\xi}^\pm$ result is retrieved after the $\Delta\eta^F > 2$ cut.

Like the ATLAS soft rapidity gap measurement, the H1 ‘SD’ measurements were not able to completely suppress cases where the proton dissociates to low mass states disappearing into the beam pipe. Rather than attempting to subtract this DD contribution, H1 defined their measured cross section as including DD with proton dissociation masses $M_Y < 1.6$ GeV. The DD contribution was estimated to increase the measured cross section by a factor 1.23 ± 0.10 based on comparisons with later Roman pot proton-tagged SD measurements. The 23% enhancement was propagated through the QCD fits used to extract the DPDFs and further, into the POMWIG model. We therefore remove it from POMWIG here by dividing the POMWIG prediction by 1.23 to get it to a pure SD prediction.

The procedure for the S^2 estimate can be schematically expressed by equation

$$S^2 = \frac{(\text{Data} - \text{ND}_{\text{Py8}}) \cdot \frac{\text{SD}_{\text{Py8}}}{\text{SD}_{\text{Py8}} + \text{DD}_{\text{Py8}}}}{\text{Pomwig}/1.23}, \quad (12.1)$$

where ‘Py8’ stands for PYTHIA8 Monte Carlo (Donnachie-Landshoff pomeron flux is used for SD and DD). The gap survival probability estimates are summarized in Table 12.2. The S^2 value is found to be 21% in the $\Delta\eta^F$ variable and 16% in the $\tilde{\xi}^\pm$ variable, for $R = 0.6$. For $R = 0.4$, the numbers are 12% and 7% respectively. It needs to be emphasized that all these S^2 estimates suffer from sizable statistical uncertainties, so the $S^2_{\Delta\eta^F} \sim 21\%$ value is actually in a good

¹This method is preferred over a direct DD subtraction (based on the prediction by PYTHIA8 DD only), because it is not possible to fix the DD cross section in a similar fashion as was done for ND models (normalized to match the data in the first $\Delta\eta^F$ bin).

agreement with $S_{\xi^\pm}^2 \sim 16\%$ (and vice versa for $R = 0.4$ jets). Moreover, it can be concluded that even the highest obtained value, 21% (found for the jet cone radius of 0.6), is in a rough agreement (within total uncertainties) with the value of $12\% \pm 5\%$ found by the CMS Collaboration in the bin $0.0003 < \tilde{\xi} < 0.002$. The CMS analysis used the jet cone radius of 0.5 and the LO POMWIG SD from which the DD contribution has been subtracted in the same way as in our analysis. This value then decreased to S^2 of $8\% \pm 4\%$ when the LO POMWIG SD has been replaced by the NLO MC POWHEG SD.

Data / MC	$3 < \Delta\eta^F < 4$	$-3.2 < \log \tilde{\xi}^\pm < -2.5$
$S_{\text{Data}/\text{SD}_{\text{Pomwig}}}^2$, Anti- k_T $R = 0.6$	0.21 ± 0.10	0.16 ± 0.04
$S_{\text{Data}/\text{SD}_{\text{Pomwig}}}^2$, Anti- k_T $R = 0.4$	0.12 ± 0.09	0.07 ± 0.04

Table 12.2: S^2 as the data to the POMWIG Monte Carlo ratios along with the statistical uncertainties for selected bins in $\Delta\eta^F$ and $\tilde{\xi}^\pm$. The $\tilde{\xi}^\pm$ result is retrieved after the $\Delta\eta^F > 2$ cut. ND component as predicted by PYTHIA8 is subtracted from the data. The DD component is subtracted based on Pythia8 (D-L flux) DD/SD ratio. A DD component $23\% \pm 10\%$ is subtracted from Pomwig SD.

As we saw, the gap survival probability is dependent on the choice of jet cone size and the particular distribution ($\Delta\eta^F$ or $\tilde{\xi}^\pm$). Since the S^2 estimate from the $3 < \Delta\eta^F < 4$ bin has larger statistical uncertainties and worse ND suppression (see Table 12.1), the value extracted from the measurement of $\tilde{\xi}^\pm$ with the $\Delta\eta^F > 2$ cut is preferred. Similar argument is valid for the difference between jet algorithms: due to smaller statistical uncertainties and better ND suppression, the result for $R = 0.6$ is favored. No attempt has been made to assess the model dependence of the S^2 estimate as only one reliable diffractive model is available (Pomwig). However, changing the ND contribution in the extraction procedure from PYTHIA8 LO to POWHEG + PYTHIA8 NLO results in the gap survival probability of 15%.

13. Conclusions

The physics analysis discussed in this thesis is the first cross section measurement of this kind performed at the ATLAS Experiment. It provides a significant extension of the previous ATLAS soft rapidity gap analysis as it is done at the hard scale (two relatively high p_T jets are required) and it introduces, in addition to the rapidity gap measurement, the measurement of the fractional momentum loss of the diffractive proton. Compared to the similar measurement by the CMS Collaboration, substantial improvements are achieved as well: the rapidity gap size distribution in diffractive dijet events is provided in addition to the proton fractional momentum loss (on which the CMS analysis focused) and the measurements are done for two distance parameters ($R = 0.4$ and $R = 0.6$) of the anti- k_T jet reconstruction algorithm (CMS provided results for $R = 0.5$ only).

Forward rapidity gaps, denoted as $\Delta\eta^F$, constitute a characteristic attribute of diffractive interactions. Though it is found that even non-diffractive interactions can produce large rapidity gaps, they are exponentially falling off with increasing $\Delta\eta^F$. Rapidity gaps thus provide an illustrative mean for distinguishing between diffraction and non-diffraction. The relationship between $\Delta\eta^F$ and the mass of the diffractive system leads to a direct relationship between $\Delta\eta^F$ and $\tilde{\xi}^\pm$, which approximates, for single diffractive events, fractional momentum loss of the scattered proton based on the information available within the acceptance of the calorimeter system of the ATLAS Experiment.

Comparisons of the data corrected for experimental effects to various Monte Carlo models lead to the conclusion that though the non-diffractive models alone are able to describe a significant portion of the data via fluctuations in the hadronisation process, a diffractive component is also needed for a more complete description of the data, especially for large rapidity gaps and small $\tilde{\xi}^\pm$. Finally, it was found that the requirement of the hard scale changes the topology of diffractive interactions. Consequently, the rapidity gap distribution, instead of reaching a plateau at large $\Delta\eta^F$ as observed by the ATLAS soft rapidity gap analysis, falls off exponentially with increasing $\Delta\eta^F$.

Besides measurements of the differential cross sections as a function of $\Delta\eta^F$ and $\tilde{\xi}^\pm$, the estimate of the gap survival probability is provided. It is found to be significantly model dependent as the data, from which the non-diffractive and double diffractive contributions to the cross section have to be subtracted, are compared to POWMIG model of single diffraction. At the leading order, the gap survival probability is found to be $0.16 \pm 0.04(\text{exp.}) \pm 0.08(\text{syst.})$ based on the $-3.2 < \log_{10} \tilde{\xi}^\pm < -2.5$ region of the $\tilde{\xi}^\pm$ distribution with the $\Delta\eta^F > 2$ requirement and for the $R = 0.6$ distance parameter of the anti- k_T jet reconstruction algorithm.

A. Reproduction of the 2010 inclusive dijet measurement

Period	All events	GRL/PV/LAr	N_{cuts}	N_{cuts} cleaned+acc.	Events 30, 20	Trigger	Gap>3	Gap>4
A.L1Calo	2020106	1007969	4188400	255368	26146	692	0	0
A.MinBias	43121748	16764375	10071200	288602	26297	25601	26	8
A	45141854	17772344	14259600	543970	52443	26293	26	8
B.L1Calo	17438115	13163864	49691315	4532219	532358	94635	48	9
B.MinBias	57535304	26566896	20065838	612853	56449	22961	11	1
B	74973419	39730760	69757153	5145072	588807	117596	59	9
C.L1Calo	14045676	12315002	47353712	4933512	617271	111447	55	5
C	10258512	5742390	4256471	131876	11988	4362	5	1
C.MinBias	24304188	18057392	51610183	5065388	629259	115809	60	6
D.L1Calo	94588164	76027167	404311265	72077339	14194472	812232	151	28
D.MinBias	21242996	6966725	11705216	387575	34008	2978	0	0
D	115831160	82993892	416016481	72464914	14228480	815210	151	28
E.JetTauEtmis	45600509	41315691	283439238	76829229	22256961	544945	178	48
E.MinBias	11358962	5591610	6648141	208840	18289	2589	2	0
E	56959471	46907301	290087379	77038069	22275250	547534	180	48
F.JetTauEtmis	34947676	31119819	279421436	70450548	19675392	1218175	308	58
F	5372962	2625810	3589308	113776	9741	3696	1	58
F.MinBias	40320638	3745629	283010744	70564324	19685133	1221871	309	58
G.JetTauEtmis	35030429	27715495	255905541	69498990	19193626	834534	201	39
G.MinBias	10319234	2885218	4151951	136370	11381	3634	0	0
G	45349663	30600713	260057492	69635360	19205007	838168	201	39
H.JetTauEtmis	11466379	8949575	75170361	25359480	7287428	187659	37	2
H.MinBias	2944302	2017756	12015787	598204	50336	1405	0	0
H	14410681	10967331	87186148	25957684	7337764	189064	37	2
I.JetTauEtmis	23104942	20970707	207477390	67684411	17682042	424752	68	6
I.MinBias	3291259	2478748	7107102	314926	25352	2833	1	0
I	26396201	23449455	214584492	67999337	17707394	427585	69	6
Sum	443687275	304224817	1686569672	394414118	101709537	4299130	1092	205

Table A.1: Cut-flow table of all pp collision 2010 periods with the trigger scheme and event selection cuts implemented exactly as they were in 2010 inclusive dijet analysis. Column called “Events 30, 20” refers to the minimum p_T requirement on a (sub-)leading jet, $p_T^{\text{jet } 1(2)} > 30(20)$ GeV.

B. Systematic uncertainties: summary tables

Systematic	$0.0 < \Delta\eta^F < 0.5$	$0.5 < \Delta\eta^F < 1.0$	$1.0 < \Delta\eta^F < 2$	$2 < \Delta\eta^F < 3$	$3 < \Delta\eta^F < 4$	$4 < \Delta\eta^F < 5$	$5 < \Delta\eta^F < 6.5$
JES	(+23.7; -29.8)%	(+21.2; -27.5)%	(+19.2; -21.2)%	(+21.0; -20.5)%	(+23.8; -37.6)%	(+29.8; -39.0)%	(+27.6; -38.1)%
JES1	(+8.5; -7.1)%	(+7.2; -7.1)%	(+7.9; -4.8)%	(+6.5; -6.3)%	(+7.5; -12.4)%	(+9.9; -9.1)%	(+7.3; -5.9)%
JES2	(+11.0; -8.0)%	(+9.7; -7.7)%	(+10.0; -5.7)%	(+8.6; -6.1)%	(+10.2; -12.9)%	(+12.6; -9.4)%	(+10.4; -7.2)%
JES3	(+9.5; -9.1)%	(+8.1; -8.7)%	(+8.5; -5.8)%	(+7.4; -7.8)%	(+8.8; -14.7)%	(+11.1; -11.7)%	(+8.2; -6.8)%
JES4	(+14.5; -9.2)%	(+11.9; -8.8)%	(+10.6; -5.8)%	(+9.9; -7.7)%	(+12.6; -14.8)%	(+15.0; -11.7)%	(+12.9; -7.0)%
JES5	(+13.8; -16.4)%	(+10.6; -14.3)%	(+8.7; -11.1)%	(+8.5; -8.9)%	(+12.9; -20.2)%	(+18.6; -20.2)%	(+20.4; -29.7)%
JES6	(+8.5; -5.6)%	(+7.1; -5.7)%	(+7.4; -3.7)%	(+7.1; -4.2)%	(+6.8; -10.4)%	(+8.8; -6.4)%	(+5.4; -2.9)%
JES7	(+0.0; -0.0)%	(+0.0; -0.0)%	(+0.0; -0.0)%	(+0.0; -0.0)%	(+0.0; -0.0)%	(+0.0; -0.0)%	(+0.0; -0.0)%
JER	(+0.0; 0.0)%	(+0.1; 0.0)%	(+1.1; 0.0)%	(+3.1; 0.0)%	(+0.0; -3.0)%	(+1.8; 0.0)%	(+0.6; 0.0)%
JAR	(+0.0; -0.4)%	(+0.0; -0.5)%	(+0.3; 0.0)%	(+0.4; 0.0)%	(+0.0; -1.7)%	(+0.0; -0.5)%	(+0.0; -0.8)%
JRE	(+1.5; -1.5)%	(+1.4; -1.4)%	(+1.4; -1.4)%	(+1.4; -1.4)%	(+1.5; -1.5)%	(+1.5; -1.5)%	(+1.6; -1.7)%
ChaseE	(+0.0; -0.0)%	(+0.0; -0.0)%	(+0.0; -0.0)%	(+0.0; -0.0)%	(+0.0; -0.0)%	(+0.0; -0.0)%	(+0.0; -0.0)%
CST	(+0.3; -0.3)%	(+10.8; -10.1)%	(+16.1; -14.6)%	(+10.9; -17.8)%	(+4.1; -5.7)%	(+5.6; -5.1)%	(+9.8; -16.2)%
JCE	(+0.9; -0.8)%	(+0.8; -0.7)%	(+0.7; -0.6)%	(+1.1; -1.0)%	(+0.5; -0.4)%	(+0.9; -0.7)%	(+0.1; -0.2)%
LoosePV0	(+0.0; 0.0)%	(+0.0; 0.0)%	(+0.1; 0.0)%	(+0.6; 0.0)%	(+0.5; 0.0)%	(+0.2; 0.0)%	(+0.3; 0.0)%
Unfolding	(+0.2; 0.0)%	(+0.0; -6.0)%	(+0.0; -16.5)%	(+0.0; -16.3)%	(+0.0; -5.4)%	(+0.0; -5.9)%	(+0.0; -8.5)%
Trigger (Fit)	(+0.5; -0.2)%	(+0.6; -0.2)%	(+0.4; -0.2)%	(+0.6; -0.2)%	(+0.6; -0.2)%	(+0.3; -0.1)%	(+1.3; -0.1)%
Trigger (MC)	(+1.9; 0.0)%	(+1.0; 0.0)%	(+1.4; 0.0)%	(+1.4; 0.0)%	(+2.1; 0.0)%	(+1.8; 0.0)%	(+1.3; 0.0)%
Tracking	± 1.0 %	± 1.0 %	± 1.0 %	± 1.0 %	± 1.0 %	± 1.0 %	± 1.0 %
Luminosity	± 3.5 %	± 3.5 %	± 3.5 %	± 3.5 %	± 3.5 %	± 3.5 %	± 3.5 %
Added Material	± 3.0 %	± 3.0 %	± 3.0 %	± 3.0 %	± 3.0 %	± 3.0 %	± 3.0 %
Total uncertainty	(+28.0; -24.6)%	(+25.7; -25.7)%	(+27.6; -27.7)%	(+23.5; -30.0)%	(+25.6; -37.0)%	(+33.1; -31.3)%	(+31.1; -37.9)%

Table B.1: Contributions to the systematic uncertainty on the differential cross section for $\Delta\eta^F$ selected with anti- k_T . $R = 0.6$ jets. The total systematic uncertainty is calculated as the quadratic sum of the individual contributions.

Systematic	$0.0 < \Delta\eta^F < 0.5$	$0.5 < \Delta\eta^F < 1.0$	$1.0 < \Delta\eta^F < 2$	$2 < \Delta\eta^F < 3$	$3 < \Delta\eta^F < 4$	$4 < \Delta\eta^F < 5$	$5 < \Delta\eta^F < 6.5$
JES	(+21.1; -24.7)%	(+22.9; -27.0)%	(+21.5; -29.5)%	(+16.9; -30.2)%	(+14.0; -27.1)%	(+15.5; -17.0)%	(+15.5; -17.9)%
JES1	(+5.7; -5.4)%	(+6.1; -6.3)%	(+6.1; -6.8)%	(+4.9; -5.6)%	(+3.6; -2.7)%	(+4.6; -4.4)%	(+2.6; -2.7)%
JES2	(+9.0; -2.9)%	(+9.4; -4.1)%	(+8.9; -4.0)%	(+9.3; -2.4)%	(+3.9; -1.8)%	(+6.4; -2.9)%	(+3.7; -2.0)%
JES3	(+5.9; -8.9)%	(+6.0; -10.9)%	(+6.7; -11.2)%	(+3.4; -8.3)%	(+4.6; -4.9)%	(+4.6; -6.7)%	(+3.0; -4.4)%
JES4	(+7.9; -5.0)%	(+8.6; -5.9)%	(+8.5; -6.3)%	(+8.4; -5.4)%	(+4.0; -2.7)%	(+6.0; -4.0)%	(+4.0; -2.7)%
JES5	(+12.6; -14.4)%	(+14.2; -16.8)%	(+11.9; -16.1)%	(+8.9; -17.3)%	(+9.4; -6.6)%	(+10.2; -11.2)%	(+13.2; -16.2)%
JES6	(+6.7; -5.0)%	(+8.0; -5.6)%	(+7.2; -5.0)%	(+7.4; -5.2)%	(+3.9; -2.2)%	(+4.9; -3.5)%	(+2.6; -1.4)%
JES7	(+0.0; -0.0)%	(+0.0; -0.0)%	(+0.0; -0.0)%	(+0.0; -0.0)%	(+0.0; -0.0)%	(+0.0; -0.0)%	(+0.0; -0.0)%
JER	(+1.1; 0.0)%	(+2.9; 0.0)%	(+2.7; 0.0)%	(+0.0; -0.8)%	(+0.5; 0.0)%	(+2.6; 0.0)%	(+0.9; 0.0)%
JAR	(+0.0; -0.7)%	(+0.3; 0.0)%	(+0.0; -0.5)%	(+0.5; 0.0)%	(+0.0; 0.0)%	(+0.0; -0.3)%	(+0.0; -0.4)%
JRE	(+1.4; -1.4)%	(+1.4; -1.5)%	(+1.4; -1.4)%	(+1.7; -1.7)%	(+1.0; -1.1)%	(+1.2; -1.3)%	(+1.1; -1.1)%
ClustE	(+0.0; -0.0)%	(+0.0; -0.0)%	(+0.0; -0.0)%	(+0.0; -0.0)%	(+0.0; -0.0)%	(+0.0; -0.0)%	(+0.0; -0.0)%
CST	(+0.4; -0.4)%	(+9.6; -9.4)%	(+16.5; -14.1)%	(+10.5; -20.5)%	(+6.7; -9.0)%	(+2.7; -5.8)%	(+11.8; -19.5)%
JCE	(+0.8; -0.7)%	(+0.9; -0.8)%	(+0.8; -0.7)%	(+1.2; -1.1)%	(+0.5; -0.5)%	(+0.8; -0.7)%	(+0.3; -0.4)%
LoosePV0	(+0.0; 0.0)%	(+0.0; 0.0)%	(+0.1; 0.0)%	(+0.5; 0.0)%	(+0.2; 0.0)%	(+0.1; 0.0)%	(+0.0; -0.0)%
Unfolding	(+0.3; 0.0)%	(+0.0; -7.1)%	(+0.0; -12.2)%	(+0.0; -14.6)%	(+0.0; -6.4)%	(+0.0; -5.9)%	(+0.0; -6.5)%
Trigger (Fit)	(+0.4; -0.2)%	(+0.4; -0.2)%	(+0.4; -0.2)%	(+0.4; -0.2)%	(+0.5; -0.3)%	(+0.4; -0.2)%	(+1.0; -0.5)%
Trigger (MC)	(+1.5; 0.0)%	(+1.3; 0.0)%	(+2.2; 0.0)%	(+2.3; 0.0)%	(+3.2; 0.0)%	(+2.7; 0.0)%	(+2.4; 0.0)%
Tracking	± 1.0 %	± 1.0 %	± 1.0 %	± 1.0 %	± 1.0 %	± 1.0 %	± 1.0 %
Luminosity	± 3.5 %	± 3.5 %	± 3.5 %	± 3.5 %	± 3.5 %	± 3.5 %	± 3.5 %
Added Material	± 3.0 %	± 3.0 %	± 3.0 %	± 3.0 %	± 3.0 %	± 3.0 %	± 3.0 %
Total uncertainty	(+21.0; -20.0)%	(+25.1; -26.2)%	(+27.2; -29.8)%	(+21.6; -33.4)%	(+15.7; -15.4)%	(+17.1; -17.9)%	(+20.0; -27.3)%

Table B.2: Contributions to the systematic uncertainty on the differential cross section for $\Delta\eta^F$ selected with anti- k_T $R = 0.4$ jets. The total systematic uncertainty is calculated as the quadratic sum of the individual contributions.

Systematic	$-3.2 < \log_{10} \hat{\xi}^{\pm} < -2.5$	$-2.5 < \log_{10} \hat{\xi}^{\pm} < -2$	$-2 < \log_{10} \hat{\xi}^{\pm} < -1.5$	$-1.5 < \log_{10} \hat{\xi}^{\pm} < -1$	$-1 < \log_{10} \hat{\xi}^{\pm} < -0.5$	$-0.5 < \log_{10} \hat{\xi}^{\pm} < -0.5$
JES	(+35.0; -47.6)%	(+25.7; -33.6)%	(+21.7; -33.1)%	(+21.4; -23.9)%	(+23.3; -28.1)%	(+25.7; -39.9)%
JES1	(+11.6; -9.9)%	(+7.3; -7.0)%	(+6.2; -11.1)%	(+7.5; -7.7)%	(+8.6; -7.0)%	(+9.0; -6.4)%
JES2	(+15.6; -10.8)%	(+10.2; -7.1)%	(+9.0; -10.7)%	(+10.0; -8.4)%	(+11.2; -7.4)%	(+10.9; -9.5)%
JES3	(+13.2; -11.4)%	(+8.2; -8.4)%	(+7.2; -11.3)%	(+8.7; -9.1)%	(+9.6; -8.8)%	(+9.5; -10.0)%
JES4	(+18.4; -11.5)%	(+12.2; -8.3)%	(+12.6; -11.8)%	(+11.7; -9.1)%	(+14.1; -9.0)%	(+17.0; -9.9)%
JES5	(+25.9; -32.0)%	(+15.1; -17.7)%	(+12.7; -14.5)%	(+9.0; -10.7)%	(+13.5; -14.3)%	(+18.0; -29.3)%
JES6	(+10.4; -6.3)%	(+6.4; -4.9)%	(+6.5; -7.9)%	(+7.1; -5.8)%	(+8.8; -5.5)%	(+8.5; -5.4)%
JES7	(+0.0; -0.0)%	(+0.0; -0.0)%	(+0.0; -0.0)%	(+0.0; -0.0)%	(+0.0; -0.0)%	(+0.0; -0.0)%
JER	(+3.8; 0.0)%	(+0.8; 0.0)%	(+0.0; -2.3)%	(+0.2; 0.0)%	(+0.9; 0.0)%	(+0.0; -0.8)%
JAR	(+0.4; 0.0)%	(+0.0; -0.3)%	(+0.0; -3.0)%	(+0.0; -0.5)%	(+0.4; -0.1)%	(+0.4; 0.0)%
JRE	(+1.8; -1.9)%	(+1.4; -1.5)%	(+1.2; -1.3)%	(+1.4; -1.5)%	(+1.5; -1.5)%	(+1.5; -1.5)%
ClusteE	(+7.1; -8.9)%	(+4.9; -7.5)%	(+7.1; -14.1)%	(+6.5; -12.4)%	(+3.6; -8.0)%	(+32.0; -14.8)%
CST	(+0.2; -0.1)%	(+0.7; -0.3)%	(+0.0; -0.8)%	(+1.1; -1.3)%	(+0.1; 0.0)%	(+0.9; -1.2)%
JCE	(+0.4; -0.3)%	(+0.5; -0.4)%	(+0.6; -0.6)%	(+0.9; -0.8)%	(+0.9; -0.8)%	(+0.7; -0.7)%
LoosePV0	(+1.1; 0.0)%	(+0.4; 0.0)%	(+0.1; 0.0)%	(+0.0; 0.0)%	(+0.0; 0.0)%	(+0.0; 0.0)%
Unfolding	(+2.8; 0.0)%	(+4.3; 0.0)%	(+0.0; -8.3)%	(+0.0; -3.2)%	(+0.0; -1.8)%	(+8.6; 0.0)%
Trigger (Fit)	(+0.5; -0.1)%	(+0.4; -0.2)%	(+0.5; -0.2)%	(+0.5; -0.2)%	(+0.5; -0.2)%	(+0.4; -0.1)%
Trigger (MC)	(+1.0; 0.0)%	(+1.6; 0.0)%	(+1.2; 0.0)%	(+3.1; 0.0)%	(+2.2; 0.0)%	(+0.0; -3.5)%
Tracking	± 1.0 %	± 1.0 %	± 1.0 %	± 1.0 %	± 1.0 %	± 1.0 %
Luminosity	± 3.5 %	± 3.5 %	± 3.5 %	± 3.5 %	± 3.5 %	± 3.5 %
Added Material	± 10.0 %	± 10.0 %	± 10.0 %	± 10.0 %	± 10.0 %	± 10.0 %
Total uncertainty	(+43.2; -41.7)%	(+28.4; -27.4)%	(+26.5; -34.3)%	(+25.9; -26.9)%	(+29.7; -26.1)%	(+46.8; -39.6)%

Table B.3: Contributions to the systematic uncertainty on the differential cross section for $\log_{10} \hat{\xi}^{\pm}$ selected with anti- k_T $R = 0.6$ jets. The total systematic uncertainty is calculated as the quadratic sum of the individual contributions.

Systematic	$-3.2 < \log_{10} \xi^\pm < -2.5$	$-2.5 < \log_{10} \xi^\pm < -2$	$-2 < \log_{10} \xi^\pm < -1.5$	$-1.5 < \log_{10} \xi^\pm < -1$	$-1 < \log_{10} \xi^\pm < -0.5$	$-0.5 < \log_{10} \xi^\pm < -0.5$
JES	(+23.7; -51.9)%	(+24.7; -36.0)%	(+24.8; -28.9)%	(+20.5; -33.1)%	(+21.1; -23.6)%	(+22.4; -23.3)%
JES1	(+7.5; -7.0)%	(+6.3; -7.3)%	(+9.0; -8.6)%	(+6.6; -7.8)%	(+5.7; -5.1)%	(+3.9; -4.1)%
JES2	(+12.9; -6.0)%	(+8.9; -4.0)%	(+11.7; -5.1)%	(+8.8; -3.7)%	(+9.0; -2.7)%	(+8.1; -2.5)%
JES3	(+4.0; -14.1)%	(+7.0; -12.2)%	(+6.8; -11.0)%	(+6.5; -12.1)%	(+6.7; -8.6)%	(+2.6; -7.1)%
JES4	(+13.3; -8.9)%	(+8.3; -6.6)%	(+11.6; -7.9)%	(+8.4; -7.1)%	(+8.0; -4.8)%	(+6.3; -4.0)%
JES5	(+19.3; -42.4)%	(+17.0; -23.5)%	(+15.8; -15.8)%	(+10.2; -17.1)%	(+13.1; -13.5)%	(+12.8; -16.9)%
JES6	(+9.3; -6.7)%	(+7.5; -5.2)%	(+8.3; -4.0)%	(+7.2; -10.9)%	(+7.0; -4.0)%	(+4.6; -3.4)%
JES7	(+0.0; -0.0)%	(+0.0; -0.0)%	(+0.0; -0.0)%	(+0.0; -0.0)%	(+0.0; -0.0)%	(+0.0; -0.0)%
JER	(+4.9; 0.0)%	(+5.6; 0.0)%	(+3.0; 0.0)%	(+0.6; 0.0)%	(+2.4; 0.0)%	(+0.0; -0.9)%
JAR	(+0.4; 0.0)%	(+0.0; -0.5)%	(+0.0; -0.2)%	(+0.0; -0.8)%	(+0.0; -0.3)%	(+0.0; -1.0)%
JRE	(+1.6; -1.8)%	(+1.6; -1.6)%	(+1.4; -1.5)%	(+1.4; -1.5)%	(+1.3; -1.4)%	(+1.4; -1.5)%
ClusE	(+9.0; -13.6)%	(+4.4; -10.6)%	(+7.7; -15.8)%	(+7.0; -10.5)%	(+3.2; -3.5)%	(+21.7; -16.8)%
CST	(+0.0; -0.4)%	(+0.8; 0.0)%	(+0.0; -0.5)%	(+1.0; -0.8)%	(+0.5; -0.3)%	(+1.8; -2.3)%
JCE	(+0.2; -0.3)%	(+0.6; -0.6)%	(+0.8; -0.7)%	(+0.9; -0.8)%	(+0.8; -0.8)%	(+0.6; -0.6)%
LoosePV0	(+0.3; 0.0)%	(+0.0; 0.0)%	(+0.0; 0.0)%	(+0.0; 0.0)%	(+0.0; 0.0)%	(+0.0; -0.0)%
Unfolding	(+0.0; -4.2)%	(+1.5; 0.0)%	(+0.0; -8.1)%	(+0.0; -2.3)%	(+0.0; -4.7)%	(+16.2; 0.0)%
Trigger (Fit)	(+0.4; -0.2)%	(+0.4; -0.3)%	(+0.4; -0.2)%	(+0.4; -0.2)%	(+0.4; -0.2)%	(+0.3; -0.2)%
Trigger (MC)	(+1.3; 0.0)%	(+4.5; 0.0)%	(+19.4; 0.0)%	(+0.9; 0.0)%	(+0.8; 0.0)%	(+0.0; -0.1)%
Tracking	± 1.0 %	± 1.0 %	± 1.0 %	± 1.0 %	± 1.0 %	± 1.0 %
Luminosity	± 3.5 %	± 3.5 %	± 3.5 %	± 3.5 %	± 3.5 %	± 3.5 %
Added Material	± 10.0 %	± 10.0 %	± 10.0 %	± 10.0 %	± 10.0 %	± 10.0 %
Total uncertainty	(+33.1; -50.2)%	(+27.8; -32.7)%	(+35.8; -31.3)%	(+23.7; -30.3)%	(+24.0; -22.0)%	(+34.2; -28.1)%

Table B.4: Contributions to the systematic uncertainty on the differential cross section for $\log_{10} \tilde{\xi}^\pm$ selected with anti- k_T $R = 0.4$ jets. The total systematic uncertainty is calculated as the quadratic sum of the individual contributions.

Systematic	$-3.2 < \log_{10} \tilde{\xi}^{\pm} < -2.5$	$-2.5 < \log_{10} \tilde{\xi}^{\pm} < -2.25$	$-2.25 < \log_{10} \tilde{\xi}^{\pm} < -2$
JES	(+38.0; -55.0)%	(+27.6; -40.3)%	(+20.5; -26.5)%
JES1	(+11.9; -11.2)%	(+7.9; -8.1)%	(+7.3; -7.1)%
JES2	(+15.5; -11.8)%	(+11.9; -9.6)%	(+9.1; -7.0)%
JES3	(+13.3; -13.4)%	(+9.8; -10.4)%	(+7.6; -8.3)%
JES4	(+18.3; -13.5)%	(+14.0; -10.6)%	(+11.0; -8.3)%
JES5	(+28.3; -37.6)%	(+17.7; -25.5)%	(+9.2; -12.2)%
JES6	(+9.6; -6.9)%	(+7.4; -5.3)%	(+6.7; -5.5)%
JES7	(+0.0; -0.0)%	(+0.0; -0.0)%	(+0.0; -0.0)%
JER	(+5.9; 0.0)%	(+0.4; 0.0)%	(+0.0; -0.8)%
JAR	(+1.7; 0.0)%	(+0.1; 0.0)%	(+0.0; -0.9)%
JRE	(+1.7; -1.7)%	(+1.5; -1.5)%	(+1.4; -1.5)%
ClustE	(+5.0; -6.3)%	(+3.8; -3.9)%	(+1.9; -1.4)%
CST	(+1.5; -2.2)%	(+1.9; -2.6)%	(+5.5; -7.8)%
JCE	(+0.5; -0.4)%	(+0.4; -0.3)%	(+0.4; -0.4)%
LoosePV0	(+0.3; 0.0)%	(+0.4; 0.0)%	(+0.0; -0.0)%
Unfolding	(+0.0; -0.4)%	(+0.8; 0.0)%	(+6.1; 0.0)%
Trigger (Fit)	(+0.4; -0.1)%	(+0.3; -0.3)%	(+0.4; -0.3)%
Trigger (MC)	(+1.0; 0.0)%	(+1.7; 0.0)%	(+1.4; 0.0)%
Tracking	± 1.0 %	± 1.0 %	± 1.0 %
Luminosity	± 3.5 %	± 3.5 %	± 3.5 %
Added Material	± 10.0 %	± 10.0 %	± 10.0 %
Total uncertainty	(+44.3; -47.4)%	(+31.6; -34.6)%	(+25.1; -24.4)%

Table B.5: Contributions to the systematic uncertainty on the differential cross section for $\log_{10} \tilde{\xi}^{\pm}$ with $\Delta\eta^F > 2$ cut selected with anti- k_T $R = 0.6$ jets. The total systematic uncertainty is calculated as the quadratic sum of the individual contributions.

Systematic	$-3.2 < \log_{10} \tilde{\xi}^{\pm} < -2.5$	$-2.5 < \log_{10} \tilde{\xi}^{\pm} < -2.25$	$-2.25 < \log_{10} \tilde{\xi}^{\pm} < -2$
JES	(+28.5; -49.9)%	(+23.3; -29.1)%	(+27.5; -31.3)%
JES1	(+8.4; -7.1)%	(+4.2; -6.1)%	(+8.3; -8.8)%
JES2	(+10.9; -3.5)%	(+9.7; -6.1)%	(+10.6; -4.1)%
JES3	(+6.9; -13.6)%	(+5.1; -9.6)%	(+10.1; -12.0)%
JES4	(+11.4; -6.3)%	(+8.1; -7.1)%	(+10.5; -8.0)%
JES5	(+22.7; -39.1)%	(+19.7; -23.2)%	(+14.5; -16.4)%
JES6	(+8.7; -4.7)%	(+5.5; -3.8)%	(+9.7; -7.5)%
JES7	(+0.0; -0.0)%	(+0.0; -0.0)%	(+0.0; -0.0)%
JER	(+6.5; 0.0)%	(+0.7; 0.0)%	(+3.9; 0.0)%
JAR	(+0.4; 0.0)%	(+0.0; 0.0)%	(+0.0; -0.2)%
JRE	(+1.5; -1.6)%	(+1.0; -1.3)%	(+1.4; -1.4)%
ClustE	(+5.4; -6.7)%	(+4.5; -4.6)%	(+11.1; -9.0)%
CST	(+2.5; -2.2)%	(+2.0; -1.1)%	(+2.3; -4.3)%
JCE	(+0.2; -0.2)%	(+1.0; -0.9)%	(+1.2; -1.0)%
LoosePV0	(+0.4; 0.0)%	(+0.4; 0.0)%	(+0.0; 0.0)%
Unfolding	(+0.0; -4.5)%	(+11.3; 0.0)%	(+0.0; -2.7)%
Trigger (Fit)	(+0.5; -0.2)%	(+0.5; -0.4)%	(+0.4; -0.2)%
Trigger (MC)	(+2.0; 0.0)%	(+3.0; 0.0)%	(+2.9; 0.0)%
Tracking	± 1.0 %	± 1.0 %	± 1.0 %
Luminosity	± 3.5 %	± 3.5 %	± 3.5 %
Added Material	± 10.0 %	± 10.0 %	± 10.0 %
Total uncertainty	(+34.0; -45.0)%	(+29.9; -30.1)%	(+31.1; -29.1)%

Table B.6: Contributions to the systematic uncertainty on the differential cross section for $\log_{10} \tilde{\xi}^{\pm}$ with $\Delta\eta^F > 2$ cut selected with anti- k_T $R = 0.4$ jets. The total systematic uncertainty is calculated as the quadratic sum of the individual contributions.

Bibliography

- [1] M. Herrero, *The Standard Model*, arXiv:hep-ph/9812242
- [2] R. K. Ellis, W. J. Stirling and B. R. Webber, *QCD and collider physics*, Cambridge University Press, 1996
- [3] The ATLAS Collaboration, ATLAS-CONF-2013-041
- [4] P. Collins, *An introduction to Regge theory and High Energy Physics*, Cambridge U.P., 1977
- [5] A. Donnachie and P. V. Landshoff, Nucl. Phys. B **244** (1984) 322; Phys. Lett. B **296**, **227** (1992) [arXiv:hep-ph/9209205]
- [6] V. Barone, E. Predazzi, *High-Energy Particle Diffraction*, Springer-Verlag, Berlin, 2002.
- [7] G. Ingelman, P.E.Schlein, Phys.Lett. **B152** (1985) 256.
- [8] R. Bonino *et al.* [UA8 Collaboration], Phys. Lett. B **211** (1988) 239; A. Brandt *et al.* [UA8 Collaboration], Phys. Lett. B **297** (1992) 417.
- [9] A. Aktas *et al.*, *Measurement and QCD analysis of the diffractive deep-inelastic scattering cross-section at HERA*, Eur.Phys.J., vol. C48, pp. 715–748, 2006.
- [10] T. Affolder *et al.*, *Diffractive dijets with a leading antiproton in $\bar{p}p$ collisions at $\sqrt{s} = 1800$ GeV*, Phys. Rev. Lett., vol. 84, pp. 5043-5048, May 2000
- [11] Collins, John C., *Proof of factorization for diffractive hard scattering*, Physical Review **D 57** (1998), 3051
- [12] V.A. Khoze, A.D. Martin, M.G. Ryskin, *Soft diffraction and the elastic slope at Tevatron and LHC energies: a multi-pomeron approach*, Eur.Phys.J., vol. C18:167-179, September 2000
- [13] The CMS Collaboration, Serguei Chatrchyan *et al.*, *Observation of a diffractive contribution to dijet production in proton-proton collisions at $\sqrt{s} = 7$ TeV*, Phys.Rev. **D87** (2013) 012006
- [14] LHC citation !!!
- [15] The ATLAS Collaboration, G. Aad *et al.*, *The ATLAS Experiment at the CERN Large Hadron Collider*, JINST 3 (2008) S08003
- [16] The ATLAS Collaboration, *ATLAS Inner Detector Technical Design Report*, CERN/LHCC/97-16, 1997
- [17] The ATLAS Collaboration, *Liquid Argon Calorimeter*, CERN/LHCC 96-41, CERN, 1996
- [18] The ATLAS Collaboration, *ATLAS Tile Calorimeter TDR*, CERN/LHCC/96-42, 1996

- [19] C. Eck *et al.*, *LHC computing Grid: Technical Design Report*, CERN-LHCC-2005-022, 2005
- [20] The ATLAS Collaboration, *ATLAS computing: Technical Design Report*, ATLAS TDR-017, CERN-LHCC-2005-022, 2005
- [21] S. Agostinelli *et al.*, GEANT4 Collaboration, Nucl. Instrum. Meth. A **506** (2003) 250
- [22] R. Brun, F. Rademakers, *ROOT - An Object Oriented Data Analysis Framework*, Proceedings AIHENP'96 Workshop, Lausanne, Sep. 1996, Nucl. Inst. & Meth. in Phys. Res. A 389 (1997) 81-86
- [23] T. Sjostrand, S. Mrenna, and P. Z. Skands, *A Brief Introduction to PYTHIA 8.1*, Comput. Phys. Commun., vol. 178, pp. 852–867, 2008
- [24] B. Andersson, G. Gustafson, G. Ingelman, and T. Sjostrand, *Parton fragmentation and string dynamics*, Physics Reports, vol. 97, no. 23, pp. 31 – 145, 1983
- [25] G. Aad et al., *Summary of ATLAS Pythia 8 tunes*, 2012
- [26] R. Corke and T. Sjostrand, *Interleaved Parton Showers and Tuning Prospects*, JHEP, vol. 1103, p. 032, 2011
- [27] H.-L. Lai, M. Guzzi, J. Huston, Z. Li, P. M. Nadolsky, et al., *New parton distributions for collider physics*, Phys.Rev., vol. **D82**, p. 074024, 2010
- [28] T. Sjostrand, S. Mrenna, and P. Skands, *Pythia 6.4 physics and manual*, Journal of High Energy Physics, vol. 2006, no. 05, p. 026, 2006
- [29] G. A. Schuler and T. Sjöstrand, *Hadronic diffractive cross sections and the rise of the total cross section*, Phys. Rev. D, vol. 49, pp. 2257–2267, Mar 1994
- [30] G. Ingelman and P. Schlein, *Jet structure in high mass diffractive scattering*, Physics Letters B, vol. 152, no. 34, pp. 256 – 260, 1985
- [31] P. Bruni and G. Ingelman, *Diffractive W and A production at pp colliders and the pomeron parton content*, Physics Letters B, vol. 311, no. 14, pp. 317 – 323, 1993
- [32] E. L. Berger, J. C. Collins, D. E. Soper, and G. Sterman, *Diffractive hard scattering*, Nuclear Physics B, vol. 286, no. 0, pp. 704 – 728, 1987
- [33] K. H. Streng, *Hard QCD scatterings in diffractive reactions at HERA*, CERN-TH-4949, 1988
- [34] R. Ciesielski, K. Goulianos, *MBR Monte Carlo Simulation in PYTHIA8*, arXiv:1205.1446 [hep-ph]
- [35] M. Bahr *et al.*, *Herwig++ Physics and Manual*, Eur.Phys.J. **C58** (2008) 639-707, arXiv:0803.0883 [hep-ph]

- [36] B. E. Cox and J. R. Forshaw, *POMWIG: HERWIG for diffractive interactions*, Comput.Phys.Commun., vol. 145, pp. 104–110, 2002, arXiv:hep-ph/0010303
- [37] G. Corcella *et al.*, *HERWIG 6.5: an event generator for Hadron Emission Reactions With Interfering Gluons (including supersymmetric processes)*, JHEP **01**, 010 (2001)
- [38] S. Alioli, K. Hamilton, P. Nason, C. Oleari, and E. Re, *Jet pair production in POWHEG*, JHEP, vol. 1104, p. 081, 2011
- [39] J. M. Butterworth and M. H. Seymour, *Multiparton Interactions in Herwig for the LHC*, CERN-TH/95-82, MC-TH-96/05, UCL-HEP 96-02 hep-ph/9601371. Zeit. für Phys. **C72** (1996) 637-646
- [40] Y. Davygora *et al.*, *"In-situ pseudorapidity intercalibration for evaluation of jet energy scale uncertainty"*, ATL-COM-PHYS-2011-110
- [41] T. Carli *et al.*, *"Measurement of the inclusive jet cross section in pp collisions at $\sqrt{s} = 2.76$ TeV and comparison to the inclusive jet cross section at $\sqrt{s} = 7$ TeV using the ATLAS detector"*, ATL-PHYS-INT-2014-011, arXiv:1304.4739 [hep-ex]
- [42] The ATLAS Collaboration, *In-situ pseudorapidity intercalibration to evaluate jet energy scale uncertainty and calorimeter performance in the forward region*, ATLAS-CONF-2010-055, <http://cdsweb.cern.ch/record/1281312> (2010)
- [43] M. Cacciari, G. Salam, and G. Soyez, *The anti- k_T jet clustering algorithm*, JHEP **0804** (2008) 063, arXiv:0802.1189
- [44] G. Aad *et al.*, *Measurement of inclusive jet and dijet production in pp collisions at $\sqrt{s} = 7$ TeV using the ATLAS detector*, Phys.Rev., vol. **D86**, p. 014022, 2012
- [45] G. Aad *et al.*, *Rapidity gap cross sections measured with the ATLAS detector in pp collisions at $\sqrt{s} = 7$ TeV*, Eur.Phys.J., vol. **C72**, p. 1926, 2012
- [46] W. Lampl *et al.*, *Calorimeter Clustering algorithms: Description and Performance*, ATLAS-LARG-PUB-2008-002, 2008
- [47] D. Schouten, A. Tanasijczuk, M. Vetterli, the ATLAS Collaboration, *ATLAS Jet Energy Scale*, Proceedings from XXXI Physics in Collision, arXiv:1201.2429
- [48] ATLAS Collaboration, *ATLAS public Tilecal noise plots*, <https://twiki.cern.ch/twiki/bin/view/AtlasPublic/ApprovedPlotsTileNoise>
- [49] G. Aad *et al.*, *Measurements of the pseudorapidity dependence of the total transverse energy in proton-proton collisions at $\sqrt{s} = 7$ TeV with ATLAS*, JHEP, vol. 1211, p. 033, 2012

- [50] B. Malaescu, *An Iterative, Dynamically Stabilized (IDS) Method of Data Unfolding*, 2011
- [51] The ATLAS Collaboration, *Jet energy scale and its systematic uncertainty in proton-proton collisions at $\sqrt{s} = 7$ TeV in ATLAS 2010 data*, ATLAS-CONF-2011-032, 2011
- [52] G. Aad *et al.*, *Jet energy resolution in proton-proton collisions at $\sqrt{s} = 7$ TeV recorded in 2010 with the ATLAS detector*, Eur.Phys.J., vol. **C73**, p. 2306, 2013
- [53] The ATLAS Collaboration, *Improved luminosity determination in pp collisions at $\sqrt{s} = 7$ TeV using the ATLAS detector at the LHC*, CERN-PH-EP-2013-026, arXiv:1302.4393 [hep-ex]